LARGE EDDY SIMULATION (LES) OF TURBULENT FLOWS IN GAS TURBINE

Mohammad Karimi

A Thesis
in
The Department
of
Mechanical and Industrial Engineering

Presented in Partial Fulfillment of the Requirements
for the Degree of Master of Applied Science in Mechanical Engineering at
Concordia University
Montreal, Quebec, Canada

February 2007

Library and
Archives Canada

Published Heritage
Branch

395 Wellington Street
Ottawa ON K1A 0N4
Canada

Bibliothèque et
Archives Canada

Direction du
Patrimoine de l'édition

395, rue Wellington
Ottawa ON K1A 0N4
Canada

Your file Votre référence
ISBN: 978-0-494-28953-2
Our file Notre référence
ISBN: 978-0-494-28953-2

NOTICE:
The author has granted a non-exclusive license allowing Library and Archives Canada to reproduce, publish, archive, preserve, conserve, communicate to the public by telecommunication or on the Internet, loan, distribute and sell theses worldwide, for commercial or non-commercial purposes, in microform, paper, electronic and/or any other formats.

The author retains copyright ownership and moral rights in this thesis. Neither the thesis nor substantial extracts from it may be printed or otherwise reproduced without the author's permission.

AVIS:
L'auteur a accordé une licence non exclusive permettant à la Bibliothèque et Archives Canada de reproduire, publier, archiver, sauvegarder, conserver, transmettre au public par télécommunication ou par l'Internet, prêter, distribuer et vendre des thèses partout dans le monde, à des fins commerciales ou autres, sur support microforme, papier, électronique et/ou autres formats.

L'auteur conserve la propriété du droit d'auteur et des droits moraux qui protège cette thèse. Ni la thèse ni des extraits substantiels de celle-ci ne doivent être imprimés ou autrement reproduits sans son autorisation.

In compliance with the Canadian Privacy Act some supporting forms may have been removed from this thesis.

While these forms may be included in the document page count, their removal does not represent any loss of content from the thesis.

Conformément à la loi canadienne sur la protection de la vie privée, quelques formulaires secondaires ont été enlevés de cette thèse.

Bien que ces formulaires aient inclus dans la pagination, il n'y aura aucun contenu manquant.

Canada

ABSTRACT

LARGE EDDY SIMULATION (LES) OF TURBULENT FLOWS IN GAS TURBINE

Mohammad Karimi

Compressible turbulent flow over a modern gas turbine blade is modeled in this thesis using Large Eddy Simulation (LES) methods. CFD simulation of turbo-machinery flows is a challenging problem due to the high Reynolds and Mach numbers of such flows. Reynolds Averages Navier Stokes (RANS) methods that are currently used in industry to model such turbulent flows do not give satisfactory results specifically at off-design conditions and therefore there is a need to further improve the turbulence modeling in the CFD simulations. Herein, different variations of the LES method are investigated to simulate this compressible turbulent flow. LES methodologies consist of Smagorinsky, Dynamic Smagorinsky, and Implicit LES accompanied by Yoshizawa and Van Driest relations. In this work, a 3D unstructured tetrahedral Navier-Stokes solver is applied using a mixed finite-volume-finite-element method. LES terms are discretized using the finite-element method. Parallel computation is performed according to MPI standards.

LES pressure distribution results have significant differences with the 3D RANS results. Much more discrepancy is expected in velocity profiles, shear stresses, and heat transfer characteristics. Considering pressure distribution results and compared to the currently used RANS models, LES results are fairly superior especially in the off-design conditions. LES results of this work are more superior to RANS results in the regions close to leading edge which contains very high strain in fluid elements and it is not satisfactorily resolvable using RANS. RANS results of [66] are superior to LES results of

this work for the mid suction side at which the turbulence structures are not resolved well in LES where a separation leads to constant pressure distribution which is captured as an attached flow in LES. This might be due to not introducing fluctuations at LES inlet and also to not having enough mesh resolution. Both LES and RANS results have difficulty resolving the shock/boundary layer interaction on the rear suction side of the blade. This might also be cured in LES by improving the mesh at that region or using adaptation methods or enhancing the shock capturing characteristics of the flux calculation method. The deficiencies of the LES simulation are discussed and possible cures and future works are elaborated.

This work aims at accomplishing the first step and providing a solid basis for future works on an intellectually challenging topic which is of high importance in academia and industry: *Turbulence Modeling*.

ACKNOWLEDGEMENTS

I would like to thank the Natural Sciences and Engineering Research Council of Canada (NSERC) for funding this work and the Réseau Québécois de Calcul de Haute Performance (RQCHP) for providing access to computer resources.

I wish to express my thanks to my supervisor, Professor Marius Paraschiviou, for all his support and guidance throughout the research.

I am indebted to Dr. Kaveh Mohamed for all his encouragements and for his many constructive discussions and comments. Without whom this work would never be as good as it is now.

I also would like to acknowledge students of Concordia University CFD Application Laboratory for their great sense of friendship and support. To me, CFD Lab looks like a library of great minds from whom I learnt a lot.

In my most heartfelt acknowledgement, I would like to dedicate this work to the greatest scientist, philosopher, doctor, and also poet that I had the chance to know in my life, *Ibn Sina*, known in the West as *Avicenna.* For he is the most beautiful mind I encountered in my life. In Iran he is also known as 'leader among the wise men' and 'Prince of Physicians'. He was born in 980 C.E. in the village of Afshana in Iran and lived a hard multi-dimensional life with hardworking, interest, and magnificent contributions to logic, philosophy, physics, metaphysics, medicine, and Sufism. When friends advised him to take life in moderation, he replied "*I prefer a short life with width to a narrow one with length*". When he cured the King and was asked for anything in exchange, he asked for permission to access Royal Library. From the 12th-17th century, his book 'the Qanun', served as the chief guide to Medical Science in the West and is said to have influenced Leonardo da Vinci. In the words of Dr. William Osler, the Qanun has remained "*a medical bible for a longer time than any other work* ".

TABLE OF CONTENT

LIST OF FIGURES

LIST OF TABLES

NOTATIONS

c	Speed of sound
c_p	Specific heat at constant pressure
c_v	Specific heat at constant volume
C_s	Smagorinsky constant
$C(I)$	Finite-volume cell which contains node I
$\partial C(I)$	Finite-volume cell boundaries
e_I	Internal energy
e	Total specific energy
$E(I)$	Tetrahedral element which contains node I
$E(\kappa)$	Energy spectrum function
${}^{c}F$	Convective flux
${}^{v}F$	Diffusive flux
g	Acceleration of gravity
h	Total specific enthalpy
h_S	Static enthalpy
k	Conductivity
l_0	Large eddy scale
L	Length
M	Mach number
M_I	Dual-mesh shape function at node I
n_1	X-component of unit normal vector $\vec{n}$
n_2	Y-component of unit normal vector $\vec{n}$
n_3	Z-component of unit normal vector $\vec{n}$
N_n	Number of nodes
N_e	Number of elements
N_I	Finite-element shape function at node I
p	Pressure
Pr	Prandtl number
q	Heat transfer
R_g	Gas constant
Re	Reynolds number
S	Source term
$\lvert S \rvert$	Characteristic rate of strain tensor
t	Time
Δt	Time step
T	Temperature

u_1	X-component of velocity
u_2	Y-component of velocity
u_3	Z-component of velocity
W	Conservative variable
x	Direction
y^+	Non-dimensional distance from wall

Greek Letters

α	Van-Leer flux calculation coefficient
α_{attack}	Angle of attack
β	Filter weight
ρ	Density
μ	Dynamic coefficient of viscosity
λ	Eigenvalue
δ	Delta function
γ	Polytropic coefficient
κ	Van-Leer flux calculation coefficient
κ	Wavenumber
ε	Energy dissipation rate
η	Kolmogorov scale
δ_v	Viscous length scale
ψ	Test function
Ω	Physical domain
$\partial\Omega$	Physical domain boundaries
Ω_h	Computational domain
Ψ	Characteristic variables
Δ	LES filter width

Vectors and Matrices

$\vec{n}$	Unit normal vector
$\vec{\omega}$	Angular velocity
$\vec{v}$	Relative velocity
$\vec{u}$	Absolute velocity
$\vec{f}$	External force
$\vec{r}$	Local position vector
A_{IJ}	Jacobian matrix for edge IJ
Λ	Matrix of eigenvalues
P_W^{-1}	Left eigenvector matrix

P_W	Right eigenvector matrix
S_{ij}	Strain tensor
τ_{ij}	Shear stress tensor
σ_{ij}	Stress tensor
L_{ij}	Leonard stress tensor
τ_{ij}^h	Numerical stress tensor

Superscripts

$+$	Non-dimensional quantity
$\bar{\bullet}$ or $\overleftrightarrow{\bullet\bullet\bullet}$	Grid filter
$\hat{\bullet}$ or $\widehat{\bullet\bullet\bullet}$	Test filter
$\bullet'$	Sub-grid scale variable
B	Boundary
C	Convective
n	Time step
T	Transpose
U	Upwind

Subscripts

0	Reference quantity
IJ	Roe average values between nodes I and J
is	Isentropic
i	Direction (x, y, or z)
j	Direction (x, y, or z)
k	Direction (x, y, or z)
$,k$	Differentiation with respect to the variable k
t	Turbulent

Abbreviations

CFD	Computational Fluid Dynamics
DNS	Direct Numerical Simulation
ILES	Implicit Large Eddy Simulation
LES	Large Eddy Simulation
MUSCL	Monotone Upwind Scheme for Conservation Laws
RANS	Reynolds Averaged Navier-Stokes
SGS	Sub-Grid Scale
TVD	Total Variation Diminishing

Chapter 1

TURBO-MACHINERY DESIGN USING CFD

1.1 Using CFD in Turbo-Machinery Design

The main parameters in aircraft gas turbine engine design are the *thermal efficiency*, the *specific power*, and the *specific weight*. These parameters are to be increased in the design process. Increasing the thermal efficiency leads to lowering the specific fuel consumption. *Thermal efficiency* is a direct function of the overall cycle pressure ratio and the thermodynamic efficiency of the individual components. *Specific power* mainly depends of the maximum cycle temperature. *Specific weight* can be heightened by using lightweight and high strength materials and reducing the number of turbo-machinery stages by increasing the stage pressure ratio. The design process is a complicated and expensive sequence of tasks which iteratively has to improve all the design parameters. As an illustration, a typical design cycle is shown in figure 1.1.

The Use of *Computational Fluid Dynamic* (CFD) techniques in aerodynamic design process is the key technology area to increase the speed of the design cycle, reduce testing time and therefore, necessary investments. In addition, CFD, by providing the computational experiment, provides the insight into the flow physics. CFD analysis codes solve the fluid flow equations at different levels of approximations. These codes are then used iteratively in the design process for optimizing the component geometry and to achieve the desired level of performance.

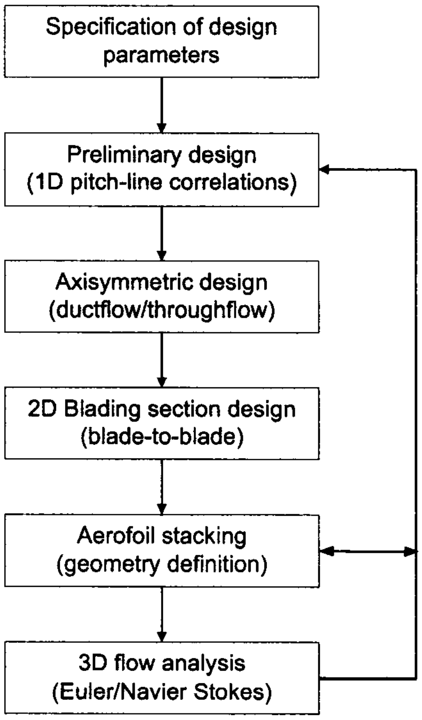

Fig. 1.1: *Typical turbo-machinery aerodynamic design cycle [1]*

The preliminary design stage provides an initial definition of the geometry of the blade and the annulus of the turbo-machinery. The design cycle is based on the analysis where the blade geometry is assessed using CFD codes and it is iteratively refined [1].

1.2 CFD Methodologies Used in Turbo-Machinery Design

The application of CFD in design dates back to 60's. The reference [2] is mainly consulted to present the history of using CFD in turbo-machinery design. The early computer codes in 60's and early 70's, for defining the geometry and analysis of the turbo-machinery flows used streamline curvature methods, stream function methods, and potential function methods. *Streamline curvature methods* are capable of predicting the overall performance of the turbo-machine both at the design and off-design conditions. However, these methods need the introduction of the real-flow-effect correlations for loss, deviation, and blockage. *Stream function formulations* are restricted to the two dimensional flows. *Potential function formulations* are not able to capture shocks due to the non-conservative form of the discretized principal equations. In the late 70's, these drawbacks were tackled after introduction of the CFD methods based on Euler equations. In contrary to the preceding methods, the *Euler method* is capable of solving inviscid flows with shocks. The Euler method was used for blade to blade flows or through linear cascades. Until then, CFD codes were all used for 2D flow simulations. Nonetheless, the flow in radial, mixed, and highly loaded axial flow machines are highly three dimensional. In the late 70's, the *three dimensional inviscid* solvers have been developed. In the same era, the need for unsteady simulation was realized and CFD codes were improved to simulate *unsteady compressible flows* to simulate the four major sources of unsteadiness: wake rotor interaction, potential interaction (interaction between adjacent blade rows), vortex shedding, and flutter (blade oscillations).

In the mid 80's, it was recognized that viscous effects can become very significant, especially in flows with shock boundary layer interactions. Also, many key phenomena of the flow such as tip clearance flows can only be analyzed by viscous modeling. Two approaches for viscous modeling have been introduced: *viscous-inviscid interaction methods* as well as *Reynolds Averaged Navier-Stokes* (RANS) equations with appropriate turbulence models for 2d and 3d flows. RANS models proved to be more robust and accurate and are still the most commonly used models accompanied by transition and turbulence models.

After all of the above-mentioned improvements in CFD calculations, currently the selection of the turbulence model is the key feature in the quality of the simulation. The most commonly used turbulence models in the context of turbo-machinery flows are Baldwin-Lomax and $k-\varepsilon$ models where the latter is more complicated but often results in better results.

With all the improvements in CFD simulations, there is still a need for more accurate turbulence models [3]. The new area for improving CFD calculations is to try to find better turbulence models out of the context of RANS models. It is understood that most RANS deficiencies stem from the fact that it aims at modeling all the scales of the flow in a time-averaged sense disregarding the fact that these scales of the flow may be time-dependent. Hence, recently more attention has been paid to simulating rather than modeling the flow. All scales of the flow can be simulated, instead of being modeled, using *Direct Numerical Simulation* (DNS) of the Navier-Stokes equations. If DNS becomes feasible for a flow, it will give the most complete possible picture of the flow governed by Navier-Stokes equations. However, for moderate to high Reynolds number flows, DNS is not currently feasible. DNS power depends essentially on the computing power and it is expected to be practicable in around 80 years [12]. *Large Eddy Simulation* (LES) of the turbulence, which is the subject of this work, has a flow realization level between RANS and DNS models and until DNS becomes feasible for high Reynolds number flows, applying LES models remains the area for improving the quality of CFD simulations.

1.3 History and Literature of Large Eddy Simulation of Turbulent Flows

The first LES simulation dates back to 30 years ago [12]. So far, there have been numerous works to solidify the theory of LES, to provide experimental data that can be used to verify LES models, and to apply LES models to different flows (free shear, wall bounded, acoustic, combustion, etc.). However, as LES has been in its infancy, most of the application was toward academic flows with very simple geometry. Below, the LES literature is addressed.

The most important contributions to the theory of LES have been accomplished in *Stanford Turbulence Research Center.* A survey of the research carried out at this center from 1996-2005 shows that so far the academic cases or the industrial cases of very simple geometry have been investigated. Different areas in which LES has played a role and the flow geometries are as shown in table 1.1.

Table 1.1: *Flows Simulated Using LES*

Type of Flow	The Case Under Consideration
Aero-Acoustic	trailing edge vortices
Combustion	nozzle with variable cross-sectional area
Free shear Flows	jets, mixing layers
Wall Bounded Flows	lid driven cavity, channel flow, diffuser (ramp), flow passed circular cylinder

Table 1.1 shows the areas for which LES has been tested and proved to overpower RANS models. As can be seen from the test cases, usually very simple flows and geometries are modeled. This fact is true for the whole literature on LES.

A very interesting work at Stanford Turbulence Research Center has been the simulation of all parts of a gas turbine [4-5], in which compressor and turbine are modeled using RANS models and combustor is modeled using LES. The interface of the RANS-LES models is matched [6-8]. RANS models have been used for the large scale turbo-machinery calculations, such as flow over multiple stages of gas turbine or compressor blades [9] or flow over a helicopter rotor [10]. For external flows of large computational domain, such as flow over an airfoil [11], LES and RANS have been mixed. LES is used for the regions around the airfoil and RANS is used for the rest of the domain.

The *Von Karman Institute for Fluid Dynamics (VKI)* is one of the most important European centers in which they work on LES. In the lecture series given at VKI between 1998-2005 there is one work of Piomelli [12] in which he presented the LES methodology for incompressible flow as well as some "building block" flows such as channel flow, 3D boundary layer, flow over a bump, and the wake downstream of a circular cylinder. Also, some industrial problems of very simple geometry have been tackled which include swirling and non-swirling coaxial jets and an asymmetric plane diffuser. He concluded that LES is not a substitute for other turbulence models but it complements other models. LES is expected to be reliable for first and second moments and to produce the basic structures of the flow. In addition, LES should be applied to complex flows in which the cost is comparable to RANS models or in problems where other models fail and the Reynolds number is so high that the solution can not be reached by DNS methods. Such problems include 3D boundary layer flows, vortex-boundary interactions, separated flows, and flow in complex geometries. In other simple cases, LES serves to give a better understanding of the physics of the problem as well as a reliable data base for assessing the other lower-level turbulence models.

Also in VKI lecture series 1998-2005, Comte and Lesieur [13] presented the LES methodologies in the context of compressible flows. Their unpredictability growth investigation shows that the LES error increases linearly with time rather than exponential growth of chaotic dynamical systems. This fact is promising in unsteady flow simulations using LES. They also found that dynamic LES models are capable of reducing the LES viscosity when the solver is too dissipative. They investigated some academic applications such as compressible mixing layers and flat plat boundary layer as well as some industrial applications with very simple geometries such as simplified solid rocket engine and a curved compression ramp.

Elsevier Science Direct is a very rich data base of scientific works in different disciplines. From 1996 to 2006, there have been around 700 works in which they applied LES, however, only very few works have been done on turbo-machinery flows. These works are as follows: Some external flows are investigated using LES on delta wing [14-16] or NACA airfoils [15-17]. The aero-acoustic LES simulation on an axial fan is presented in [18]. Conwoy et al. [19] investigated a stator blade is investigated using LES but they have not verified their method with experimental data. Rodi [20] investigated a low-pressure blade cascade is investigated using DNS and LES for two low Reynolds numbers 50,000 and 150,000. On the suction side, the LES and DNS results for C_p show good agreement with experiment with a bit more discrepancy compared to RANS model. On the pressure side however, C_p is underestimated using both LES and DNS results but

RANS results have a better agreement with experimental data. Also on both pressure and suction surfaces, LES and DNS results are almost indistinguishable.

Journal of Turbomachinery contains the most enormous amount of research works on the turbomachinery flows physics, measurements, simulations and models, etc. Also it contains many informative works close to the scope of this work, for example [21-22] for the flow physics, it does not have many LES or DNS works. Perhaps the closest work in this journal to the scope of this thesis is [23] which is a DNS of a transitional cascade flow with low Reynolds number (Re=60,000). Although [23] contains many useful information on the turbomachinery flow simulation, but in the pressure distribution calculation, DNS could only find the pressure distribution on the suction side correctly and it underestimated the pressure over all pressure side.

AIAA journal is another very important data base for aeronautical and turbomachinery works. The first successful LES of flow around an airfoil near stall is presented in AIAA journal in 2002 [24]. Also, very recently, at the last minutes of submission of this thesis, another interesting LES application is published in AIAA journal [25]. The Reynolds number in this work is close to ours, Re=5.0e+05, but the Mach number is much lower, M=0.3, compared to the transonic flow investigated here. Hence, they have no shock/boundary layer interaction. The numerical simulation is very different from ours. 6th order compact differences are used on a structured mesh. Turbulent stresses are modeled implicitly and a 10th order filter is used. They realized successfully the pressure distribution around the blade and also laminar-turbulent transition. They also explored remarkably the transitional behavior of the boundary layer. They work is the first successful LES application of a cascade flow at high Reynolds number that has been encountered in the literature review of this thesis. However, the Mach number limitation in this work did not allow creation of shocks and observing the competence of their method on the shock/boundary layer capturing.

The thorough literature review reveals that the current study is one of the very first LES applications to turbomachinery flows at high Reynolds and Mach numbers.

1.4 Thesis Originality and Outline

As pointed out in the LES literature review, very little work has been done in applying LES methodologies in turbo-machinery flow analysis. In this work, the flow over a gas turbine blade cascade at high Reynolds and Mach numbers is investigated using LES at design and off-design conditions. The aim is to study different LES models in the literature and their behavior and performance for a real industrial flow in a complex geometry and in different flow conditions. To the authors knowledge this work constitutes one of the very first LES attempts at simulation of such flow at high Reynolds and Mach number regimes.

FLUENT software as a robust and user-friendly commercial CFD software is always the first choice in simulating industrial flows. However, the latest version of the software FLUENT 6 does not have the LES model for compressible flows. Besides, its parallel version has a limit on the size of the simulations. For the case under consideration here, a parallel research CFD code is used which is originally developed by Dr. Paraschiviou and has been extended by works of Kaveh Mohamed.

The CFD code used in this thesis is a finite-volume-finite-element Navier-Stokes solver. At the starting point of this work, the CFD code was developed to solve external compressible Navier-Stokes equations only. In the course of this work, appropriate boundary conditions for internal turbo-machinery flow have been added to the code and by some minor changes in the governing equations, a new CFD code was developed which was tailored for internal turbo-machinery flow. Afterwards, some variations of the LES turbulence model available in the literature were added. In the next step, all of the above modifications were brought to the parallel version of the code according to MPI standards. Aside form the CFD code development stages at CFD Applications Lab of Concordia University, more than 100,000 CPU*Hour was spent at Mammoth Parallel Computer of Sherbrook University to run the simulations. The Mammoth project is a 1024 processor LINUX cluster. The super-computer will be divided in two parts: A "serial" one which will be composed of the latest generation of X86 processors, interconnected by an Ethernet gigabit network. A parallel part, equipped with 64-bit processors (AMD Opteron or INTEL Itanium2) interconnected with a high-speed network (Quadrix, Myrinet or Infiniband). For this work the Mammoth Parallel is used and the parallelization is performed according to MPI standards.

The outline of this thesis is as follows: Chapter 2 is devoted to presentation of the governing equations of the gas dynamics and their specific non-dimensional form used in this work. In chapter 3, the numerical method used to solve the gas flow in this thesis is fully described. The material in chapter 3 is further extended in chapter 4 to introduce boundary conditions in the CFD application used herein. In chapter 5, all the steps and different models for *Large Eddy Simulation* of the turbulence are presented and the specific filtered governing equations used in this thesis are derived. Also, a thorough literature review on different LES models capabilities and features is accomplished. LES simulation strategies and results are brought forth in chapter 6 and the future work is presented.

Chapter 2

GOVERNING EQUATIONS

The governing equations of gas dynamics are a set of three conservation equations, second law of thermodynamics, and equations of state. The three conservation equations require that the three fundamental properties mass, momentum, and energy are neither created nor destroyed and throughout the fluid flow they are just redistributed or, except for mass, are converted to each other. The second law of thermodynamics requires that another fundamental property which is entropy should never decrease. The equations of state specify the type and nature of the gas. This collection of equations when written for a fixed coordinate system, are called Euler Equations; while, they are called Lagrange Equations when expressed for a moving coordinate system. Taking into account the effect of viscosity in momentum and energy conservation laws leads to Navier-Stokes Equation which are considered as the most complete governing equations of modern gas dynamics.

2.1 Conservation Laws, Compressible Navier-Stokes Equations

The unsteady compressible Navier-Stokes Equations in conservative form and in 3D Cartesian coordinate system are written as follows [26],

$$\frac{\partial W}{\partial t}+\frac{\partial}{\partial x_j}\left({}^{c}F_j+{}^{v}F_j\right)=S \tag{2.1}$$

where W is the vector of conservative variables. ${}^{c}F_j$ and ${}^{v}F_j$ designate convective and viscous fluxes respectively. S is the external forces applied on the system such as gravity.

$$W=\begin{bmatrix}\rho\\ \rho u_1\\ \rho u_2\\ \rho u_3\\ \rho e\end{bmatrix},\ {}^{c}F_j=\begin{bmatrix}\rho u_j\\ \rho u_j u_1+p\delta_{j1}\\ \rho u_j u_2+p\delta_{j2}\\ \rho u_j u_3+p\delta_{j3}\\ \rho u_j h\end{bmatrix},\ {}^{v}F_j=\begin{bmatrix}0\\ -\sigma_{j1}\\ -\sigma_{j2}\\ -\sigma_{j3}\\ -u_k\sigma_{kj}+q_j\end{bmatrix},S=\begin{bmatrix}\rho f_1\\ \rho f_2\\ \rho f_3\\ \rho f_4\\ \rho f_5\end{bmatrix} \tag{2.2}$$

Vector of conservative variables is formed per volumetric mass ρ. u_1 and u_2 and u_3 are Cartesian components of the velocity. Total specific energy, e, is the summation of internal energy and kinetic energy,

$$e=e_I+\frac{1}{2}u_i^2 \tag{2.3}$$

h is the total specific enthalpy given by

$$h=e+\frac{p}{\rho} \tag{2.4}$$

Tensor of viscous forces for a Newtonian fluid using the Boussinesq relation is written as,

$$\sigma_{ij}=\mu\left(u_{i,j}+u_{j,i}\right)+\lambda u_{k,k}\delta_{ij} \tag{2.5}$$

Where μ is the dynamic coefficient of viscosity and the second coefficient of viscosity of the fluid λ is given by the Stokes relation,

$$\lambda+\frac{2}{3}\mu=0 \tag{2.6}$$

Dynamic viscosity of the gas varies as a function of temperature according to the Sutherland relation,

$$\mu = \mu_S \left(\frac{T}{T_S} \right)^{\frac{3}{2}} \left(\frac{T_S + T_C}{T + T_C} \right) \quad , \quad T < 2000K \tag{2.7}$$

where T_C is a constant for a given gas, and it is equal $T_C = 110.4K$ for air. Constants μ_S and T_S are reference values generally chosen at zero Celsius degree $T_S = 237.15K$ and $\mu = 1.711 \times 10^{-5} kg.m^{-1}.s^{-1}$.

Conduction heat flux is expressed by Fourier law as,

$$q_i = -kT_{,i} \tag{2.8}$$

where thermal conductivity can be obtained with assumption of constant Prandtl number,

$$k = \frac{\mu c_p}{\Pr} \tag{2.9}$$

Prandtl number of the air in normal condition is $\Pr = 0.72$. In cases where Prandtl number can not be fixed, variation of thermal conductivity with temperature may be approximated as,

$$k = k_S \frac{\mu}{\mu_S} \left[1 + C(T - T_S) \right] \tag{2.10}$$

with $k_S = 0.0242 kg.m.s^{-3}.K^{-1}$ and $C = 0.00023K^{-1}$.

In the case where gravity is the only external force applied on the system, the source term $\vec{S}$ becomes:

$$\vec{S} = \begin{bmatrix} 0 \\ \rho g n_1 \\ \rho g n_2 \\ \rho g n_3 \\ \rho g n_k u_k \end{bmatrix} \tag{2.11}$$

The acceleration of gravity is $g = 9.81\,m.s^{-2}$. The vector $\vec{n} = (n_1, n_2, n_3)^T$ is the direction along which the gravity is exerted.

2.1.1 Rotating Frame of Reference

In a rotating frame of reference, assuming a steady rotation of $\vec{\omega}$, the governing equations undergo some changes. By taking the frame velocity into account, the velocity $\vec{u}$ changes to relative velocity $\vec{v} = \vec{u} - \vec{\omega} \times \vec{r}$, where $\vec{r}$ is the local position vector. The Coriolis and centrifugal forces, $-2\rho\vec{\omega} \times \vec{v} - \rho\vec{\omega} \times (\vec{\omega} \times \vec{r})$, have to be considered as an external force, $\vec{f}_e$, and added to the source term as follows,

$$\vec{S} = \begin{bmatrix} 0 \\ \rho f_1 \\ \rho f_2 \\ \rho f_3 \\ \rho f_k u_k \end{bmatrix} \tag{2.12}$$

The total energy takes the new form [27],

$$e^* = e_I + \frac{1}{2}\left(v_i^2 - (\vec{\omega} \times \vec{r})_i^2\right) = e - (\vec{\omega} \times \vec{r}) \cdot \vec{u} \tag{2.13}$$

The total enthalpy changes to rothalpy I as [27],

$$I = h_S + \frac{1}{2}\left(v_i^2 - (\vec{\omega} \times \vec{r})_i^2\right) = h - (\vec{\omega} \times \vec{r}) \cdot \vec{u} \tag{2.14}$$

where, e_I and h_S are internal energy and static enthalpy, respectively. e and h are total energy and total enthalpy, respectively.

2.2 Equations of State

Equations of state specify the type of the fluid and serve to define the thermodynamic state of the fluid. The thermodynamic state of a fluid is defined by specifying three thermodynamic properties of that fluid. Thermodynamic properties of a fluid, such as internal energy and enthalpy, describe the average microscopic properties of that fluid, in contrast to mechanical properties of a fluid, such as velocity and kinetic energy, which describe macroscopic properties of the fluid. Some properties such as density or pressure can either be considered as mechanical or thermodynamic properties.

Three equations of state are needed to determine all thermodynamic properties. As all the properties in gas dynamics are specific properties, i.e. per unit mass, there is only need to two equations of state on the account that mass per unit mass is always one. Hence two specific equations of state are needed to determine all other specific equations of state.

In analogy to the conservations laws which are expressed on the macroscopic level, the equations of state are the conservation laws on the microscopic level. Assuming that direct collision is the only mechanism for momentum transfer, applying the conservation of momentum law on microscopic level lead to the *ideal gas law* or *thermal equation of state* [28],

$$p = \rho R_g T \tag{2.15}$$

where R_g is the gas constant and it is equal to $287 N.m/kg.K$ for sea-level air. A fluid satisfying this relationship is called *thermally perfect.* Using the same assumption, applying the conservation of energy law on the microscopic level leads to the *caloric equation of state* [28],

$$e_I = c_v T \tag{2.16}$$

Or equivalently,

$$h = c_p T \tag{2.17}$$

There is a constant on the right hand side of too which is usually unimportant. c_v and c_p are specific heat in constant volume and constant pressure, respectively. Their values are assumed constant and for sea-level air are as follows, $c_v = 717 N.m/kg.K$ and $c_p = 1004 N.m/kg.K$. Any fluid satisfies the above-mentiones relation is called *calorically perfect.*

Some useful definitions and relations for perfect gases are the followings. Ratio of the specific heats is the polytropic coefficient which is 1.4 for air,

$$\gamma = \frac{c_p}{c_v} \tag{2.18}$$

Gas constant and the specific heats are related as below,

$$R_g = c_p - c_v \tag{2.19}$$

Using the above definition, the internal energy is written as a function of pressure as follows,

$$e_I = \frac{p}{\rho(\gamma - 1)} \tag{2.20}$$

This allows expressing the total energy as,

$$\rho e = \frac{p}{(\gamma - 1)} + \frac{1}{2} \rho u_i^2 \tag{2.21}$$

This allows for evaluating the pressure from conservative variables.

The speed of sound is the ratio of the speed at which the small disturbances, such as acoustic disturbances, propagate through a substance to the speed of movement of the substance.

$$c = \sqrt{\frac{\gamma P}{\rho}} = \sqrt{\gamma R_g T} \qquad (2.22)$$

Two other equations of state can be derived using the definition of speed of sound as given below,

$$e = \frac{1}{2}u^2 + \frac{1}{\gamma(\gamma - 1)}c^2 \qquad (2.23)$$

$$h = \frac{1}{2}u^2 + \frac{1}{\gamma - 1}c^2 \qquad (2.24)$$

In the same fashion, other equations of state for perfect gases can be derived.

2.3 Non-Dimensionalization

Non-dimensionalization chosen here allows for writing transport equations in the same form as the dimensional equations.

2.3.1 Non-Dimensional Parameters

Dimensional parameter ϕ is non-dimensionalized by a reference value ϕ_0 to give the non-dimensional parameter ϕ^+. Principal reference values are given in the table below,

***Table 2.1:** Reference Values for Non-dimensionalization of Governing Equations*

$\phi = \phi_0 \phi^+$	Reference Values Relations
$\vec{x} = L_0 \vec{x}^+$	
$\vec{u} = u_0 \vec{u}^+$	$u_0 = \sqrt{R_g T_0}$
$t = t_0 t^+$	$t_0 = L_0 / u_0$
$\rho = \rho_0 \rho^+$	
$T = T_0 T^+$	
$p = p_0 p^+$	$p_0 = \rho_0 R_g T_0$
$\mu = \mu_0 \mu^+$	
$k = k_0 k^+$	
$e = e_0 e^+$	$e_0 = u_0{}^2$

The choice of t_0 and p_0 stems from non-dimensionalization of conservation of mass equations and equation of state respectively.

Non-dimensionalization of the Navier-Stokes equations will lead to the definition of three non-dimensional parameters which are,

$\mathrm{Re} = \dfrac{\rho_0 u_0 L_0}{\mu_0}$ Reynolds number, the ratio of convective term to dissipative term

$\Pr = \frac{c_p \mu_0}{k_0}$ Prandtl number, the ratio of viscous diffusion μ_0/ρ_0 to the thermal conduction $k_0/\rho_0 c_p$

$Ma = \frac{u_0}{c_0}$ Mach number, the ratio of the speed of the flow to the speed of sound in the fluid

2.3.2 Equation of State

For a perfect gas, the pressure is given as a function of density and temperature by the equation of state,

$$p = \rho R_g T \tag{2.25}$$

With the aid of non-dimensional values this equation can be written as,

$$p = \rho_0 \rho^+ R_g T_0 T^+ \tag{2.26}$$

This permits using the relation for reference pressure $p_0 = \rho_0 R_g T_0$ to write

$$p^+ = \rho^+ T^+ \tag{2.27}$$

2.3.3 Non-Dimensional Equation of Conservation of Mass

The equation of conservation of mass is written as,

$$\frac{\partial \rho}{\partial t} + \frac{\partial \rho u_i}{\partial x_i} = 0 \tag{2.28}$$

With the aid of non-dimensional values this equation can be written as,

$$\frac{\rho_0}{t_0}\frac{\partial \rho^+}{\partial t^+} + \frac{\rho_0 u_0}{L_0}\frac{\partial \rho^+ u_i^+}{\partial x_i^+} = 0 \tag{2.29}$$

Using the relation for reference time $t_0 = L_0/u_0$ this equation can be written as,

$$\frac{\partial \rho^+}{\partial t^+} + \frac{\partial \rho^+ u_i^{\ +}}{\partial x_i^{\ +}} = 0 \tag{2.30}$$

This shows that the non-dimensional equation has the same form as the corresponding dimensional one.

2.3.4 Non-Dimensional Equation of Conservation of Momentum

The equation of conservation of momentum is written as,

$$\frac{\partial \rho u_i}{\partial t} + \frac{\partial \rho u_i u_j}{\partial x_j} = -\frac{\partial p}{\partial x_i} + \frac{\partial \sigma_{ij}}{\partial x_j} \tag{2.31}$$

The tensor of viscous stresses is defined as,

$$\sigma_{ij} = \mu(u_{i,j} + u_{j,i}) - \frac{2}{3}\mu u_{k,k}\delta_{ij} \tag{2.32}$$

Using the corresponding non-dimensional values it leads to:

$$\sigma_{ij} = \frac{\mu_0 u_0}{L_0}\left[\mu^+(u^+{}_{i,j^+} + u^+{}_{j,i^+}) - \frac{2}{3}\mu^+ u^+{}_{k,k^+}\delta_{ij}\right] = \frac{\mu_0 u_0}{L_0}\sigma_{ij}^+ \tag{2.33}$$

In which the notation for differentiation is $\frac{\partial \bullet}{\partial x_i^+} \equiv \bullet_{,i^+}$. The multiplying coefficient in this equation can be written as $\frac{\mu_0 u_0}{L_0} = \frac{\rho_0 u_0^{\ 2}}{\mathrm{Re}}$. Hence the last term on the right hand side of the conservation of momentum equation can be written as,

$$\sigma_{ij,j} = \frac{\rho_0 u_0^{\ 2}}{L_0}\frac{1}{\mathrm{Re}}\sigma_{ij,j^+}^+ \tag{2.34}$$

The gradient of pressure term can be written in non-dimensional form as following, using the relation of reference pressure $p_0 = \rho_0 R_g T_0$,

$$p_{,i} = \frac{\rho_0 R_g T_0}{L_0} p^+_{,i^+} \tag{2.35}$$

The unsteady and convective terms on the left hand side can be non-dimensionalized using the relation of reference velocity $u_0 = \sqrt{R_g T_0}$,

$$(\rho u_i)_{,t} + (\rho u_i u_j)_{,j} = \frac{\rho_0 u_0^2}{L_0} \left[(\rho^+ u_i^+)_{,t} + (\rho^+ u_i^+ u_j^+)_{,j} \right] \tag{2.36}$$

The non-dimensional form of the equation of conservation of momentum can be written using all previously obtained results, as

$$\frac{\partial \rho^+ u_i^+}{\partial t^+} + \frac{\partial \rho^+ u_i^+ u_j^+}{\partial x_j^+} = -\frac{\partial p^+}{\partial x_i^+} + \frac{1}{\mathrm{Re}} \frac{\partial \sigma_{ij}^+}{\partial x_j^+} \tag{2.37}$$

This non-dimensional equation is different from its corresponding dimensional one by the coefficient of $1/\mathrm{Re}$ in its right hand side.

2.3.5 Non-Dimensional Equation of Conservation of Energy

Conservation of the total energy is written as

$$\frac{\partial \rho e}{\partial t} + \frac{\partial \rho e u_i}{\partial x_i} = -\frac{\partial p u_i}{\partial x_i} + \frac{\partial \sigma_{ij} u_i}{\partial x_j} - \frac{\partial q}{\partial x_i} \tag{2.38}$$

The total specific energy, as derived before, can be written as a function of temperature,

$$e = c_v T + \frac{1}{2} u_i^2 \tag{2.39}$$

Using the non-dimensional values the above equation can be written as,

$$e = c_v T_0 T^+ + \frac{1}{2} u_0^2 u_i^{+2} \tag{2.40}$$

Applying the relation of the reference velocity $u_0 = \sqrt{R_g T_0}$,

$$e = c_v T_0 T^+ + \frac{1}{2} R_g T_0 u_i^{+2} \tag{2.41}$$

Using the relations among polytropic coefficient, specific heats, and gas constant, the above equation will be,

$$e^+ = \frac{1}{\gamma - 1} T^+ + \frac{1}{2} u_i^{+2} \tag{2.42}$$

Having the non-dimensional total specific energy, we can write the unsteady and convective terms on the left hand side of the conservation of energy equation as follows,

$$(\rho e)_{,t} + (\rho e u_i)_{,i} = \frac{\rho_0 u_0^3}{L_0} \frac{e_0}{u_0^2} \left[(\rho^+ e^+)_{,t^+} + (\rho^+ e^+ u_i^+)_{,i^+} \right] \tag{2.43}$$

Using the relation for reference total specific energy the preceding equation is written as

$$(\rho e)_{,t} + (\rho e u_i)_{,i} = \frac{\rho_0 u_0^3}{L_0} \left[(\rho^+ e^+)_{,t^+} + (\rho^+ e^+ u_i^+)_{,i^+} \right] \tag{2.44}$$

The pressure gradient term can be written in non-dimensional form as follows,

$$(p u_i)_{,i} = \frac{p_0 u_0}{L_0} (p^+ u_i^+)_{,i^+} \tag{2.45}$$

Using the relation for reference pressure $p_0 = \rho_0 R_g T_0$ and reference velocity $u_0 = \sqrt{R_g T_0}$, one can rewrite the relation for reference pressure as $p_0 = \rho_0 u_0^2$. Plugging the resulting relation for reference pressure into above equation leads to,

$$(p u_i)_{,i} = \frac{\rho_0 u_0^3}{L_0} (p^+ u_i^+)_{,i^+} \tag{2.46}$$

The viscous stress term, using the same approach as that used in non-dimensionalization of the equation of conservation of momentum, can be obtained as

$$(\sigma_{ij} u_j)_{,i} = \frac{\rho_0 u_0^3}{L_0} \frac{1}{\mathrm{Re}} (\sigma_{ij}^+ u_j^+)_{,i^+} \tag{2.47}$$

Heat flux term can be non-dimensionalized as,

$$\begin{aligned} q_{i,i} &= \left(-kT_{,i}\right)_{,i} \\ &= \frac{k_0 T_0}{L_0^{\ 2}}\left(-k^+ T^+_{,i^+}\right)_{,i^+} \end{aligned} \tag{2.48}$$

Then factoring the inverted Pradtl number out of the above equation gives,

$$q_{i,i} = \frac{k_0}{c_p \mu_0} \frac{c_p \mu_0 T_0}{L_0^{\ 2}}\left(-k^+ T^+_{,i^+}\right)_{,i^+} \tag{2.49}$$

Then factoring the inverted Reynolds number out of the above equation gives,

$$q_{i,i} = \frac{k_0}{c_p \mu_0} \frac{\rho_0 u_0^{\ 3}}{L_0} \frac{\mu_0}{\rho_0 u_0 L_0} \frac{c_p T_0}{u_0^{\ 2}}\left(-k^+ T^+_{,i^+}\right)_{,i^+} \tag{2.50}$$

Using the relation for reference velocity $u_0 = \sqrt{R_g T_0}$ and the definition of polytropic coefficient, one can write

$$\frac{c_p T_0}{u_0^{\ 2}} = \frac{c_p}{R_g} = \frac{\gamma}{\gamma - 1} \tag{2.51}$$

Hence, the non-dimensional heat flux can be written as,

$$q_{i,i} = \frac{\rho_0 u_0^{\ 3}}{L_0} \frac{1}{\mathrm{Pr}} \frac{1}{\mathrm{Re}} \frac{\gamma}{\gamma - 1}\left(-k^+ T^+_{,i^+}\right)_{,i^+} \tag{2.52}$$

Applying the relations derived before, the following non-dimensionalization for the equation of conservation of energy is obtained,

$$\frac{\partial \rho^+ e^+}{\partial t^+} + \frac{\partial \rho^+ e^+ u_i^+}{\partial x_i^+} = -\frac{\partial p^+ u_i^+}{\partial x_i^+} + \left(\frac{1}{\mathrm{Re}}\right)\frac{\partial \sigma_{ij}^+ u_i^+}{\partial x_j^+} - \left(\frac{\gamma}{\gamma - 1}\frac{1}{\mathrm{Pr}}\frac{1}{\mathrm{Re}}\right)\frac{\partial q^+}{\partial x_i^+} \tag{2.53}$$

This equation is only different from its analogous dimensional equation by the coefficients on the right hand side.

2.3.6 Non-Dimensional Conservative Form of Governing Equations

The conservative form of the non-dimensional governing equations mentioned before is given as,

$$\frac{\partial W^{+}}{\partial t^{+}}+\frac{\partial}{\partial x_j^{+}}\left({}^{c}F_j^{\ +}+{}^{v}F_j^{\ +}\right)=S^{+} \tag{2.54}$$

where the non-dimensional quantities are the following,

$$W^{+}=\begin{bmatrix}\rho^{+}\\ \rho^{+}u_1^{+}\\ \rho^{+}u_2^{+}\\ \rho^{+}u_3^{+}\\ \rho^{+}e^{+}\end{bmatrix},\ {}^{c}F_j^{\ +}=\begin{bmatrix}\rho^{+}u_j^{+}\\ \rho^{+}u_j^{+}u_1^{+}+p^{+}\delta_{j1}\\ \rho^{+}u_j^{+}u_2^{+}+p^{+}\delta_{j2}\\ \rho^{+}u_j^{+}u_3^{+}+p^{+}\delta_{j3}\\ \rho^{+}u_j^{+}h^{+}\end{bmatrix},\ {}^{v}F_j^{\ +}=\begin{bmatrix}0\\ -\frac{1}{\mathrm{Re}}\sigma_{j1}^{+}\\ -\frac{1}{\mathrm{Re}}\sigma_{j2}^{+}\\ -\frac{1}{\mathrm{Re}}\sigma_{j3}^{+}\\ -\frac{1}{\mathrm{Re}}u_k^{+}\sigma_{kj}^{+}+\frac{\gamma}{\gamma-1}\frac{1}{\mathrm{Pr}}\frac{1}{\mathrm{Re}}q_j^{+}\end{bmatrix},S=\begin{bmatrix}\rho^{+}f_1^{+}\\ \rho^{+}f_2^{+}\\ \rho^{+}f_3^{+}\\ \rho^{+}f_4^{+}\\ \rho^{+}f_5^{+}\end{bmatrix} \tag{2.55}$$

In which, h^{+} is the non-dimensional total specific enthalpy given by

$$h^{+}=e^{+}+\frac{p^{+}}{\rho^{+}} \tag{2.56}$$

The Sutherland Law for temperature variation of dynamic viscosity can also be written in non-dimensional form as,

$$\mu^{+}=\left(T^{+}\right)^{\frac{3}{2}}\left(\frac{1+T_C^{+}}{T^{+}+T_C^{+}}\right) \tag{2.57}$$

In this case, temperature variation of thermal conductivity is given as,

$$k^{+}=\frac{\mu^{+}}{\mathrm{Pr}}\frac{\gamma}{\gamma-1} \tag{2.58}$$

Chapter 3

NUMERICAL METHOD

The numerical methodology used here, is a mixed finite element finite volume method. Convective fluxes are evaluated using a finite volume type formulation. Diffusive fluxes and source terms are calculated by a finite element type approximation. Three-dimensional space is discretized using an unstructured mesh of tetrahedral elements. Dependent variables are located at the nodes of the elements leading to a cell-vertex discretization. This numerical scheme proved to be an efficient and robust method that serves well as a solid basis for introducing new turbulence models [29-30]. The sections below describe the details of the discretization of the weak form of the governing equations in space and in time. The material of this chapter is written in the lights of the excellent presentation of reference [26].

3.1 Weak Formulation

Compressible Navier-Stokes equations are written as below,

$$\frac{\partial W}{\partial t} + \nabla \cdot \left({}^{c}F + {}^{v}F \right) = S \tag{3.1}$$

where W is the vector of conservative variables, ${}^{c}F$ and ${}^{v}F$ are the convective and diffusive fluxes respectively, and S is the source term. The weak formulation is carried out by multiplying this equation by a test function ψ and integrating over the whole physical domain,

$$\int_{\Omega} \frac{\partial W}{\partial t} \psi \, dv + \int_{\Omega} \nabla \cdot \left({}^{c}F + {}^{v}F \right) \psi \, dv = \int_{\Omega} S \psi \, dv \qquad (3.2)$$

Ω stands for the domain and $\partial\Omega$ is its boundaries. The choice of the test function determines the type of approximation. Following the Galerkin method, the test function is chosen as to be the shape function of the elements. The shape functions are linear leading to second order of accuracy of the discretization.

3.2 Discretized Weak Formulation

The physical domain, Ω, is discretized by an unstructured mesh into a computational domain, Ω_h. This mesh consists of N_n nodes and N_e tetrahedral elements noted by $E(I)$. The discretized space is $\Omega_h = \bigcup_{I=1}^{N_e} E(I)$, as shown below,

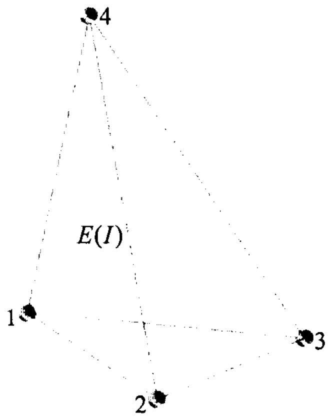

Fig 3.1: 3D Element

Starting from this mesh, we can construct another dual mesh formed by finite volume cells noted by $C(I)$. The finite volume cell around a node is formed by the contributions of each support elements, i.e. elements sharing the given node. Contribution of an element to the cell around the node, as shown in the figure below, is the volume obtained by constructing the median planes, i.e. planes containing middle points of the adjacent edges, centers of gravity of the adjacent faces, and center of gravity of the element. Cutting the element by median planes leads to having four sub-tetrahedral with vertices at centers of the edges and faces that contains node I and center of the element as well, which surround the node I. Then the cell, $C(I)$, is constructed by the union of the sub-tetrahedral having the node I as a vertex.

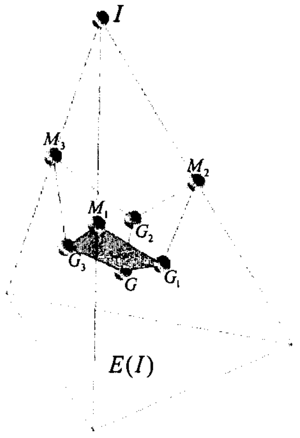

Fig 3.2: Contribution of an Element to a Cell

Dependent variables are located at the nodes of the elements. Two weak formulations are used in the mixed formulation. First weak formulation is a finite element type one, where the solution $\phi_h|_{E(I)}$ of the variable ϕ on the element $E(I)$ is defined as a function of discrete values ϕ_I at the nodes of the element as well as shape functions N_I associated to the element:

$$\phi_h|_{E(I)} = \sum_{I=1}^{N_s} \phi_I N_I(\vec{x}) \tag{3.3}$$

Here, elements are of the type P_1, and shape functions are piece-wise linear functions as given below,

$$N_I = \begin{cases} 1 \ , \ at\, node\, I \\ 0 \ , \ at\, other\, nodes\, of\, the\, element \end{cases} \tag{3.4}$$

Second weak formulation is a finite volume type one, where the solution ϕ_h of the variable ϕ on the cell $C(I)$ is defined on the dual mesh using the discrete values ϕ_I at the nodes and the shape functions M_I:

$$\phi_h = \sum_{I=1}^{N_s} \phi_I M_I(\vec{x}) \tag{3.5}$$

Base functions which are constant throughout the cell are defined as,

$$M_I = \begin{cases} 1 \ , \ on\, C(I) \\ 0 \ , \ elsewhere \end{cases} \tag{3.6}$$

The method of calculation of the flux, as it will be explained after, is a second order finite volume method, leading to second order accuracy in space.

Finite volume approximation on the cell $C(I)$ is equal to the average value finite element approximation on the same cell. In practice, these two approximations are supposed to be identical in order to apply a mixed formulation to Navier-Stokes equations [26]. Under this condition, in the discrete mixed formulation, unsteady and convective terms are treated by the finite volume method whereas diffusive and source terms are treated by the finite element method:

$$\int_{C(I)} \frac{\partial W_h}{\partial t}\, dv + \int_{C(I)} \nabla \cdot {}^{c}F(W_h)\, dv = - \int_{E(I)} \nabla \cdot {}^{v}F(W_h) N_I\, dv + \int_{E(I)} S(W_h) N_I\, dv \tag{3.7}$$

Volume integral of the convective term, using Divergence Theorem, is transformed to a surface integral on $\partial C(I)$ which is the outline of the cell $C(I)$. Divergence theorem states that the volume integral of the divergence of a vector is equal to the surface integral of that vector over the boundary of the volume:

$$\int_V \left(\vec{\nabla} \cdot \vec{F}\right) dV = \int_S \vec{F} \cdot d\vec{S} \equiv \int_S \vec{F} \cdot \vec{n}\, dS \tag{3.8}$$

Volume integral of the diffusive term is rewritten using the divergence theorem applied to the product of a scalar and a vector and using the following vector identity:

$$\vec{\nabla} \cdot \left(N\vec{F}\right) = N\left(\vec{\nabla} \cdot \vec{F}\right) + \vec{F} \cdot \left(\vec{\nabla} N\right) \tag{3.9}$$

This is also called Green theorem, leading to,

$$\begin{gathered} \int_V \left(\vec{\nabla} \cdot N\vec{F}\right) dV = \int_S N\vec{F} \cdot \vec{n}\, dS \\ \int_V \left[N\left(\vec{\nabla} \cdot \vec{F}\right) + \vec{F} \cdot \left(\vec{\nabla} N\right)\right] dV = \int_S N\vec{F} \cdot \vec{n}\, dS \\ \int_V N\left(\vec{\nabla} \cdot \vec{F}\right) dV = -\int_V \vec{F} \cdot \left(\vec{\nabla} N\right) dV + \int_S N\vec{F} \cdot \vec{n}\, dS \end{gathered} \tag{3.10}$$

Finally, the discretized weak formulation is written as:

$$\int_{C(I)} \frac{\partial W_h}{\partial t}\, dv + \int_{\partial C(I)} {}^{c}F(W_h) \cdot \vec{n}_{\partial C(I)}\, ds = \int_{E(I)} {}^{v}F(W_h) \cdot \nabla N_I\, dv - \int_{\partial E(I)} {}^{v}F(W_h) \cdot \vec{n}_{\partial \Omega_h}\, N_I\, ds + \int_{E(I)} S(W_h) N_I\, dv \tag{3.11}$$

The following sections are devoted to describe the details of discretization of the convective, diffusive, source, and unsteady terms respectively.

3.3 Discretization of the Convective Term

The convective term in the governing equations state the balance of the convective fluxes in a finite volume cell through the cell boundary faces. These faces are shown in the figure below,

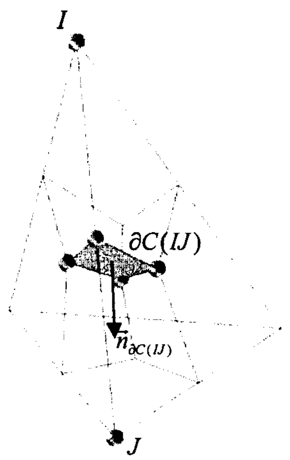

Fig 3.3: *Finite Volume Cells Surfaces*

The surface of the cell $C(I)$ around the node I is denoted by $\partial C(I)$. This surface can be written as

$$\partial C(I) = \bigcup_{J\in K(I)} \partial C(IJ) \tag{3.12}$$

where $\partial C(IJ)$ is the common face between two neighboring cells $C(I)$ and $C(J)$, and $K(I)$ notes all the neighboring nodes of the node I, i.e. the nodes connected to the node I by an edge.

Convective term can be written as,

$$\int_{\partial C(I)} {}^{c}F(W_h)\cdot\vec{n}_{\partial C(I)}\,ds = \sum_{J\in K(I)} \int_{\partial C(IJ)} {}^{c}F(W_h)\Big|_{\partial C(IJ)}\cdot\vec{n}_{\partial C(IJ)}\,ds \tag{3.13}$$

Assuming constant convective flux over the common face $\partial C(IJ)$ leads to,

$$\int_{\partial C(I)} {}^{c}F(W_h)\cdot\vec{n}_{\partial C(I)}\,ds = \sum_{J\in K(I)} {}^{c}F(W_h)\Big|_{\partial C(IJ)}\cdot\vec{n}_{\partial C(IJ)}\,S_{\partial C(IJ)} \tag{3.14}$$

And by noting $F_{IJ} = {}^{c}F_{IJ}(W_h)\Big|_{\partial C(IJ)}\cdot\vec{n}_{\partial C(IJ)}$,

$$\int_{\partial C(I)} {}^{c}F(W_h)\cdot\vec{n}_{\partial C(I)}\,ds = \sum_{J\in K(I)} F_{IJ}\,S_{\partial C(IJ)} \tag{3.15}$$

The normal vector is obtained by the contribution from each element, $E(IJ)$, that contains both nodes, I and J. In all such elements, the contribution to normal vector $\vec{n}_{IJ}$ comes from the normal vectors of the surface $\partial C(IJ)$ formed during the process of dual mesh generation.

$$\vec{n}_{IJ} = \sum_{J \in K(I)} \int_{\partial C(IJ)} \vec{n}_{\partial C(IJ)} \, ds \tag{3.16}$$

The direction of the normal vector is always outward from the cell. Hence, $\vec{n}_{IJ}$ is directed outward from the cell $C(I)$ and towards the cell $C(J)$. Therefore, it is evident that,

$$\vec{n}_{IJ} = -\vec{n}_{JI} \tag{3.17}$$

In the presence of a shock or high gradients in the flow, it is necessary to take into account the hyperbolic nature of the Euler equations which translates the perturbations in the privileged directions called characteristic directions, as will be discussed in next chapters. The convective fluxes can be simply constructed by a centered scheme with addition of an artificial viscosity which damps the high frequency oscillations generated by the scheme near the discontinuities to avoid having non-physical solutions. Another method consists of using an upwind scheme which utilizes the propagation direction of the information, i.e. the sign of the eigenvalues of the convective matrix. This type of scheme introduces the physical conditions into the discretization scheme to model the nonlinearity of the Euler equation in presence of discontinuities. The convective flux treatment used here is the Roe method [31-32] which consists of determining an exact solution to the Riemann problem locally at the interface of the neighboring cells.

3.3.1 Roe Method

A Riemann solver of Roe [31] is used to approximate the hyperbolic part of the Navier-Stokes equations. Roe method defines a local linearization of the local Euler equation with the discontinuity located at the interfaces of the mesh. To have the first order of accuracy, the solution is supposed to be constant on each cell. A simplified figure of the linearization is shown below:

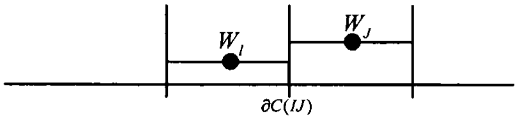

Fig 3.4: *First Order Roe Method*

At the interface, there is a discontinuity in the value of the variable. This jump in the variable value is supposed to be the contributions from three simple waves. Linearization consists of carrying out the jump on the variables defined at the interface. Roe method defines the average values in the following fashion,

$$\rho_{IJ} = \sqrt{\rho_I \rho_J} \tag{3.18}$$

$$u_{IJ} = \frac{u_I \sqrt{\rho_J} + u_J \sqrt{\rho_I}}{\sqrt{\rho_I} + \sqrt{\rho_J}} \tag{3.19}$$

$$h_{IJ} = \frac{h_I \sqrt{\rho_J} + h_J \sqrt{\rho_I}}{\sqrt{\rho_I} + \sqrt{\rho_J}} \tag{3.20}$$

where h designates the total enthalpy. Pressure can be expressed as a function of the average density, velocity, and enthalpy as,

$$p_{IJ} = \frac{\gamma - 1}{\gamma} \rho_{IJ} \left(h_{IJ} - \frac{1}{2} u_{IJ}^2 \right) \tag{3.21}$$

Speed of sound can be written as,

$$a_{IJ} = \sqrt{\gamma \frac{p_{IJ}}{\rho_{IJ}}} \tag{3.22}$$

Using these values, convective flux at the interface is written as,

$$F_{IJ} = \frac{1}{2}\left[{}^cF_I + {}^cF_J\right] - \frac{1}{2}\partial^c F_{IJ} \quad with \quad \partial^c F_{IJ} = |A_{IJ}|\partial W_{IJ} \tag{3.23}$$

where ${}^cF_I$ and ${}^cF_J$ are the physical convective fluxes at each node on both sides of the interface. $\partial^c F_{IJ}$ is the sum of the jumps in the flux as a result of the waves which are propagating through the computational domain. Existence of such waves lies in the nature of eigenvalues of the homogenous system of differential equations, i.e. the Jacobian matrices of the convective fluxes. This issue will be discussed further in next chapters. A^1, A^2, and A^3 stand for the Jacobian matrices of the flux vectors ${}^cF^1$, ${}^cF^2$, and ${}^cF^3$ respectively. Jacobian matrix J of a vector F is defined as,

$$F(x_1,\ldots,x_n) = \begin{bmatrix} f_1(x_1,\ldots,x_n) \\ . \\ . \\ . \\ f_n(x_1,\ldots,x_n) \end{bmatrix} \rightarrow J(x_1,\ldots,x_n) \equiv \frac{\partial(f_1,\ldots,f_n)}{\partial(x_1,\ldots,x_n)} = \begin{bmatrix} \partial f_1/\partial x_1 & \ldots & \partial f_1/\partial x_n \\ \ldots & \ldots & \ldots \\ \ldots & \ldots & \ldots \\ \ldots & \ldots & \ldots \\ \partial f_n/\partial x_1 & \ldots & \partial f_n/\partial x_n \end{bmatrix} \tag{3.24}$$

Matrix of Eigenvalues of $A^k \cdot n_k$ is written as,

$$\Lambda = \begin{bmatrix} \vec{u}\cdot\vec{n} & 0 & 0 & 0 & 0 \\ 0 & \vec{u}\cdot\vec{n} & 0 & 0 & 0 \\ 0 & 0 & \vec{u}\cdot\vec{n} & 0 & 0 \\ 0 & 0 & 0 & \vec{u}\cdot\vec{n} + a\sqrt{n_1^2+n_2^2+n_3^2} & 0 \\ 0 & 0 & 0 & 0 & \vec{u}\cdot\vec{n} - a\sqrt{n_1^2+n_2^2+n_3^2} \end{bmatrix} \tag{3.25}$$

where $\vec{n} = (n_1, n_2, n_3)$ is an arbitrary spatial direction. The eigenvalues, physically, represent the speed of the wave propagation in the direction $\vec{n}$. Left eigenvectors matrix, P_W^{-1}, associated with conservative variables, is formed by placing left eigenvectors in its lines. Right eigenvectors matrix, P_W, associated with conservative variables, is formed by placing right eigenvectors in its columns.

The Jacobian matrix can be diagonalized using the left and right eigenvectors matrices and eigenvalues matrix as follows,

$$|A_{IJ}| = P_W\,|\Lambda|\,P_W^{-1} \tag{3.26}$$

Hence, the change in the convective flux, $\partial^c F_{IJ}$, can be as,

$$\partial^c F_{IJ} = P_W(W_{IJ})|\Lambda_{IJ}|P_W^{-1}(W_{IJ})\partial W_{IJ} \tag{3.27}$$

The last two terms of the right hand side of the above equation are the change in characteristic variables Ψ. Characteristic variables are the information propagated along the waves and their change is obtained from projection of the change in conservative variables, ∂W, on the matrix of left eigenvectors,

$$\partial\Psi = P_W^{-1}\partial W \tag{3.28}$$

In the Roe method for flux calculations, the interface quantities which are shown by $\bullet_{IJ}$ are evaluated using the Roe average values and the change in the conservative variables are given by $\partial W_{IJ} = W_J - W_I$.

3.3.2 Entropy Correction

In the computation of inviscid flows using Roe method, some non-physical solutions may occur. Roe method only sees the values at discontinuities and therefore models an expansion wave in the sonic regions of the flow by a shock wave without taking into account its distribution [33]. In particular, in Riemann problem in which the initial condition has a jump expansion, using Roe method this expansion shock remains as stationary solution all the time. Wherever the eigenvalues of the neighboring cells have the opposite sign, in the Roe average values, speed becomes sonic in an expansion wave [26].

Roe and Pike [34] introduced an additional flux contribution in Roe's scheme in case of expansion through sonic points. This contribution is added to upstream and subtracted from downstream for conservation purpose.

Another method proposed by Harten and Hyman [35] and have been complemented by Kermani and Plett [33] which consists of detecting the expansion shock and then diffusing it by introducing a local expansion fan in Roe's method. This is done by modifying corresponding components of the eigenvalues matrix, Λ_{IJ} by searching for the regions of sonic expansion where $|\lambda|$ approaches zero. Then, Roe averages are written using the corrected eigenvalue. This condition is called entropy correction in $|\lambda|$ is approximated by $Q(\lambda)$ as,

$$Q(\lambda) = diag\begin{cases} |\lambda| & if \ \ |\lambda| \geq \varepsilon \\ \varepsilon \ (or) \ \dfrac{\lambda^2 + \varepsilon^2}{2\varepsilon} & if \ \ |\lambda| < \varepsilon \end{cases} \tag{3.29}$$

and $\varepsilon = \max[0, (\lambda - \lambda^L), (\lambda^R - \lambda)]$. The zero in maximum function avoids this correction on the compression shock.

3.3.3 Second Order Roe Method

Assuming a piece-wise constant solution in each cell leads to the first order accuracy in space. To obtain the second order accuracy in space, the solution can be approximated by piece-wise linear functions in each cell as shown in the figure below,

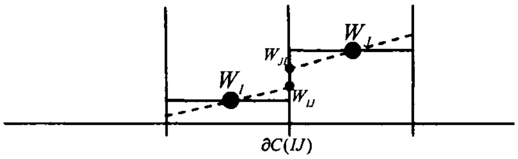

***Fig 3.5:** Second Order Roe Method*

Extension of the Roe method to second order of accuracy needs the introduction of the variables at the interface which specifies the discontinuity. These quantities are calculated by extrapolation of the corresponding variable at the adjacent cell. The extrapolated variables at the interface IJ are denoted by $\bullet_{IJ}$ in cell C_I, and by $\bullet_{JI}$ in cell C_J. Resolution of the local Reimann problem is done in the same fashion as that of first order accuracy by a new discontinuity. Roe scheme in second order of accuracy is written as [26],

$$F_{IJ}=\frac{1}{2}\left[{}^{c}F(W_{IJ})+{}^{c}F(W_{JI})\right]-\frac{1}{2}\partial^{c}F_{IJ} \tag{3.30}$$

In which the interface quantities are constructed by linear extrapolation as,

$$W_{IJ}=W_I+\frac{1}{2}(\nabla W)_I\cdot\vec{n}_{IJ} \tag{3.31}$$

$$W_{JI}=W_J+\frac{1}{2}(\nabla W)_J\cdot\vec{n}_{JI} \tag{3.32}$$

∇W_I and ∇W_J characterize the gradient of W in the cells C_I and C_J respectively. These gradients are evaluated using a finite element technique as [29],

$$(\nabla W)_I=\frac{\int_{C(I)}\nabla(W_I\varphi_I)dv}{\int_{C(I)}dv}=\frac{1}{vol(C(I))}\sum_{E\in K(I)}\frac{vol(E(I))}{N_s}\left(\sum_{1}^{N_s}W_I(\nabla\varphi)_I\right) \tag{3.33}$$

Where, N_s is the number of nodes of the finite elements $E(I)$ that support the node I, that is the elements that are a member of $K(I)$, i.e. have I as a vertex.

The change in the flux is determined by,

$$\partial^c F_{IJ} = |A_{IJ}| \partial W_{IJ} \tag{3.34}$$

Which is a function of discontinuity at inter interface $\partial W_{IJ} = W_{JI} - W_{IJ}$. This second order Roe method is a MUSCL, Monotone Upwind Scheme for Conservation Laws, type scheme. In practice, the simple linear interpolation of the variables is insufficient. Such schemes generate oscillations close to discontinuities. This behavior is avoided by imposing a TVD, Total Variation Diminishing, method. This affects the variables extrapolation by introducing a non-linear term, limiting the value of the variables in a way that the TVD condition is satisfied. In the next sections the details of flux calculation and limiter are discussed.

3.3.4 Van Leer MUSCL Type Modification of Roe Method

The $\kappa - \alpha$ type method of Van Leer [36] is basically the second order Roe method, modified by introducing a factor α allows for balancing the importance of the centered scheme and the artificial viscosity in the scheme. Flux calculation at the interface become,

$$F_{IJ} = \frac{1}{2}\left[{}^cF(W_{IJ}) + {}^cF(W_{JI})\right] - \alpha\, \partial^c F_{IJ} \tag{3.35}$$

When $\alpha = 1/2$, this scheme is the same as second order Roe method. To construct the interface variables a MUSCL type expression is used by introducing a combination of centered and upwind gradients to evaluate ∇W_{IJ} and ∇W_{JI},

$$W_{IJ} = W_I + \frac{1}{2}\left[(1-\kappa)(\nabla W)_I^C \cdot \vec{n}_{IJ} + \kappa(\nabla W)_I^U \cdot \vec{n}_{IJ}\right] \tag{3.36}$$

$$W_{JI} = W_I + \frac{1}{2}\left[(1-\kappa)(\nabla W)_J^C \cdot \vec{n}_{JI} + \kappa(\nabla W)_J^U \cdot \vec{n}_{JI}\right] \tag{3.37}$$

with centered gradient defined as $(\nabla W)_I^C \cdot \vec{n}_{IJ} = (W_J - W_I)$ and upwind gradient defined as $(\nabla W)_I^D \cdot \vec{n}_{IJ} = 2(\nabla W)_I \cdot \vec{n}_{IJ} - (W_J - W_I)$. Where the gradient at node I, as stated before, is calculated by the average on its support $E(I)$,

$$(\nabla W)_I = \frac{1}{vol(C(I))} \sum_{E \in E(I)} \frac{vol(E)}{N_s} \nabla W\big|_E \tag{3.38}$$

with $\nabla W\big|_E = \sum_{k \in E} W_k \nabla N_k\big|_E$.

The table below shows the theoretical order of accuracy of the schemes on structured mesh. When $\kappa = 0$, the scheme is totally centered and so unstable.

Table 3.1: *Order of Accuracy of the Different Variations of $\kappa - \alpha$ Method on Structured Grid*

Name of the Method	α	κ	Spatial Order of Accuracy
F2	1/2	1	2
F31	1/2	1/3	3
F32	1/10	1/3	3

3.3.5 Van Leer – Van Albada Limiter

As stated before, MUSCL type schemes, which are based on a linear interpolation of the variables at interface, can generate oscillations at the neighborhood of discontinuities. So it is customary to limit the variables values, i.e. take the gradient of the interpolation by a non-linear function g called limiter, to damp off numerical oscillations. In this case, the resulting MUSCL scheme, with the TVD property, preserves its second order of accuracy in the areas in which the gradients ∇W_h are smooth. But, the scheme becomes a first order upwind method in the vicinity of discontinuities which introduces a numerical dissipation with a beneficial damping effect.

By introduction of limiter, the flux calculation can be rewritten as [26],

$$F_{IJ} = \frac{1}{2}\left[{}^{c}F(W_{IJ}) + {}^{c}F(W_{JI})\right] - \alpha\,\partial^{c}F_{IJ} \tag{3.39}$$

with,

$$W_{IJ} = W_I + \frac{1}{2} g\left((\nabla W)_I^C \cdot \vec{n}_{IJ} \,,\, (\nabla W)_I^U \cdot \vec{n}_{IJ} \right) \tag{3.40}$$

$$W_{JI} = W_J + \frac{1}{2} g\left((\nabla W)_J^C \cdot \vec{n}_{JI} \,,\, (\nabla W)_J^U \cdot \vec{n}_{JI} \right) \tag{3.41}$$

The Van Leer – Van Albada limiter [37] is written as follows,

$$g(x,y) = \begin{cases} 0 & if \quad xy < 0 \\ \dfrac{(x^2+\varepsilon)y + (y^2+\varepsilon)x}{x^2+y^2+\varepsilon} & otherwise \end{cases} \tag{3.42}$$

where, ε is a very small number. The function g produces the 0 value whenever the centered gradient and the upwind gradient have the opposite sign; where it changes the extrapolation of the interface values to the constant mode and limits their value. This function also gives a very small value when one or both of the gradients are zero.

3.4 Discretization of the Diffusive Term

The diffusive term is discretized by a finite element type method. This term has the parabolic nature. Owing to the fact that no oscillation can arise in diffusion dominated region, discretization is carried out in a centered way. In finite element method, any function can be interpolated over a finite element $E(I)$ as,

$$F(\vec{x})\big|_{E(I)} = \sum_{j\in E(I)} F_j\left(\varphi_j(\vec{x})\right)_{E(I)} \tag{3.43}$$

In Galerkin finite element the test functions, Ψ_I, are chosen so as to be the shape functions, N_I. The contribution of the viscous term in the discrete Navier-Stokes equation after the application of Green theorem, as explained before, is decomposed into a volume integral and a surface integral, as follows,

$$-\int_{E(I)} \nabla\cdot{}^{v}F(W_h)\,N_I\,dv = \int_{E(I)} {}^{v}F(W_h)\cdot\nabla N_I\,dv - \int_{\partial E(I)} {}^{v}F(W_h)\cdot\vec{n}_{\partial\Omega_h}\,N_I\,ds \tag{3.44}$$

The surface integral represents the viscous flux which passes through the boundaries of the mesh. This contribution is generally negligible, except close to solid walls. The volume integral involves the gradient of the shape functions ∇N_I at node I. By definition, these functions are continuous and piece-wise linear on each element that supports the node I. Their gradient is therefore constant on each of these elements. The volume integral can be written as,

$$\int_{E(I)} {}^{v}F(W_h)\cdot\nabla N_I\,dv = \sum_{J\in L(I)} \int_{E(J)} {}^{v}F(W_h)\cdot\nabla N_{IJ}\,dv \tag{3.45}$$

where, $L(I)$ is the support at node I, i.e. all the elements that node I is their vertex. J is one of the supports of node I, and N_{IJ} is the base function N_I on the element $E(J)$. The approximation W_h of the value of W is piece-wise linear, so its gradient is constant on each element.

3.5 Discretization of the Source Term

The contribution of each of the support elements of the node I to the source term in discrete Navier-Stokes equations is given by,

$$\int_{E(I)} S(W_h)\, N_I\, dv = \sum_{J\in L(I)} \int_{E(J)} S(W_h)\, N_{IJ}\, dv \tag{3.46}$$

The integral of the source term is calculated as a function of the its average value in each support element, $S_J(W_h)$, over the cell as,

$$\int_{E(I)} S(W_h) N_I\, dv = \sum_{J\in L(I)} \frac{1}{N_s} (S_J(W_h)\, vol(E(J))) \tag{3.47}$$

3.6 Discretization of the Unsteady Term

The spatial discretization as mentioned above, leads to a semi-discretized formulation. The governing equations can be rewritten by having the temporal term on left hand side and the rest of the terms, $K(W_h)$, on the right hand side as,

$$\int_{C(I)} \frac{\partial W_h}{\partial t}\, dv = K(W_h) \tag{3.48}$$

The discretized temporal term is integrated by assuming constant W_h over the cell, which is fully equivalent to using a finite element discretization with a mass-lumping approximation [29].

$$\int_{C(I)} \frac{\partial W_h}{\partial t}\, dv = \frac{\partial W_h}{\partial t} \int_{C(I)} dv = \left.\frac{\partial W_h}{\partial t}\right|^{n} vol(C(I)) \tag{3.49}$$

An implicit method is used which has the advantage of having no restriction on time steps in a linear problem. In the nonlinear problem under consideration here, implicit method allows very large time steps. This property leads to faster convergence in comparison to explicit methods. However, there is a limit for CFL number to maintain stability which is found practically. Using the implicit discretization method, the right hand side of the discretized equation, $K(W_h)$, should be written in $n+1$ time step as,

$$\left.\frac{\partial W_h}{\partial t}\right|^{n} vol(C(I)) = K(W_h^{n+1}) \tag{3.50}$$

A linearized Newton procedure is applied to the right hand side of the above equation. Using Taylor series expansion, $K(W_h^{n+1})_I$ can be found to second order of accuracy as,

$$K(W_h^{n+1})_I = K(W_h^{n})_I + \frac{\partial K(W_h^{n})_I}{\partial t}\Delta t + \mathrm{O}(\Delta t)^2 \tag{3.51}$$

Using the chain rule gives a straight forward way to use the above equation,

$$\frac{\partial K(W_h^{n+1})_I}{\partial t} = \frac{\partial K(W_h^{n})_I}{\partial W_h}\left.\frac{\partial W_h}{\partial t}\right|^{n} \tag{3.52}$$

Using Taylor series expansion, W_h^{n+1} can be found to second order of accuracy as,

$$W_h^{n+1} = W_h^{n} + \left.\frac{\partial W_h}{\partial t}\right|^{n}\Delta t + \mathrm{O}(\Delta t)^2 \tag{3.53}$$

hence,

$$\left.\frac{\partial W_h}{\partial t}\right|^{n} = \frac{W_h^{n+1} - W_h^{n}}{\Delta t} \equiv \frac{\Delta W_h^{n}}{\Delta t} \tag{3.54}$$

where, ΔW_h^n signifies the change in value of ΔW_h at the time step n. Now, the right hand side of the discretized equation, $K(W_h)$, can be rewritten as,

$$K(W_h^{n+1})_I = K(W_h^{n})_I + \frac{\partial K(W_h^{n})_I}{\partial W_h}\Delta W_h^{n} \tag{3.55}$$

where, $\frac{\partial K(W_h^{n})_I}{\partial W_h}$ is simply the Jacobian of the fluxes.

It should be noted that relation 3.55 is second order accurate. However, the temporal order of accuracy of the method also depends on how $\left.\frac{\partial W_h}{\partial t}\right|^n$ is discretized. For first order accuracy in time, the following first order backward finite difference is used,

$$\left.\frac{\partial W_h}{\partial t}\right|^n = \frac{W_h^{n+1} - W_h^n}{\Delta t} \equiv \frac{\delta W_h^n}{\Delta t} \tag{3.56}$$

Hence, the discrete system is written as,

$$\left[\frac{vol(C(I))}{\Delta t_I} - \frac{\partial K(W_h^n)_I}{\partial W_h}\right]\delta W_h^n = K(W_h^n)_I \tag{3.57}$$

For second order accuracy in time, the following second order backward finite difference is used,

$$\left.\frac{\partial W_h}{\partial t}\right|^n = \frac{(1+2\tau)/(1+\tau)W_h^{n+1} - (1+\tau)W_h^n + (\tau^2)/(1+\tau)W_h^{n-1}}{\Delta t} \equiv \frac{(1+2\tau)/(1+\tau)\delta W_h^n - (\tau^2)/(1+\tau)\delta W_h^{n-1}}{\Delta t} \tag{3.58}$$

where $\tau = \Delta t_I / \Delta t_{I-1}$. The second order time integration of the governing equations is written as,

$$\left[(a)\frac{vol(C(I))}{\Delta t_I} - \frac{\partial K(W_h^n)_I}{\partial W_h}\right]\Delta W_h^n = K(W_h^n)_I + \left[(b)\frac{vol(C(I))}{\Delta t_I}\right]\Delta W_h^{n-1} \tag{3.59}$$

where $a = (1+2\tau)/(1+\tau)$, $b = (\tau^2)/(1+\tau)$, and $c = (\tau)/(1+\tau)$.

3.7 Solver

Applying the implicit time integration of Euler to the governing equations, results in a linear system of equations. This system is then solved using a flexible GMRES technique [38] which is written by written by Y. Saad and modified by A. Malevsky.

3.8 Parallelization

The physical domain is discretized using tetrahedral elements. For parallel processing purpose, the domain is partitioned, using software METIS [39] based on two criteria: having the same number of elements in each sub-domain as well as having the minimum interface nodes between adjacent sub-domains. Figure 3.6 and 3.7 show the partitioned mesh from the front 2D view and they correspond to the coarse mesh with 8 partitions and fine mesh with 32 partitions, respectively. Parallel processing is done according to MPI standards [40]. In this parallelization method, all CPUs are treated the same, i.e. they run the same code in contrary to parallelization methods that break the loops between CPUs. Here the geometry is partitioned and each partition is assigned to one CPU. Then for any data that they need from the neighboring CPUs, they communicate according to MPI standards in the MPI_COMM_WORLD communicator.

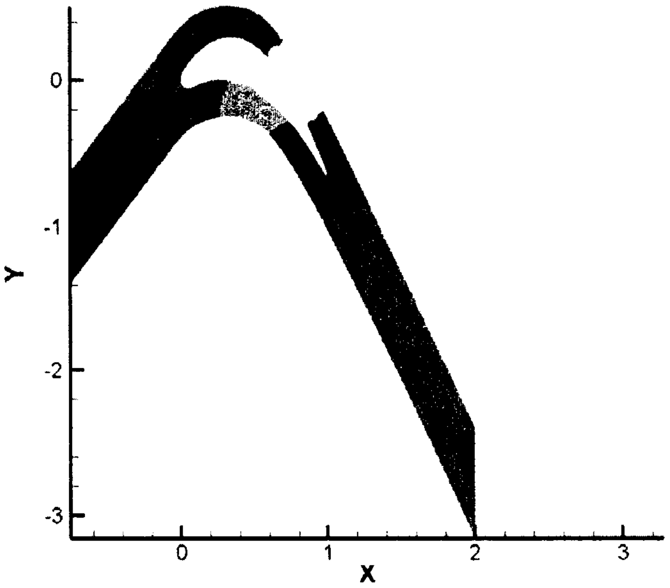

Fig 3.6: *Partitioned Coarse Mesh*

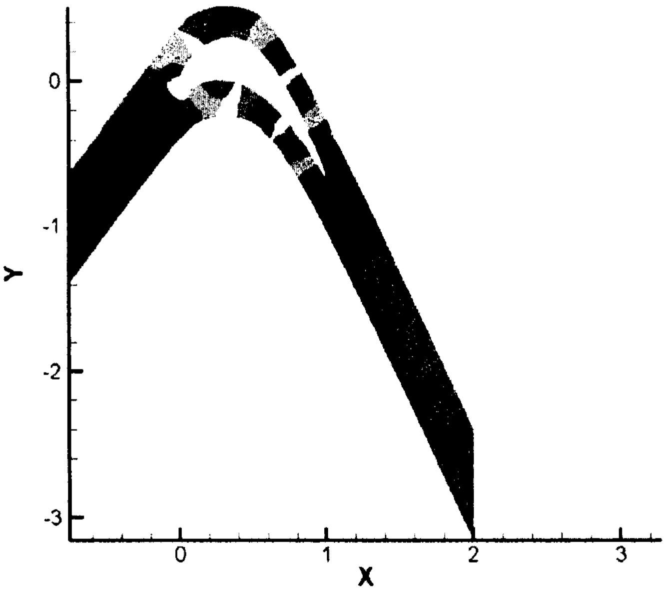

Fig 3.7: *Partitioned Fine Mesh*

Chapter 4

BOUNDARY CONDITIONS

In the present numerical method, as discussed in previous chapters, diffusive and source terms are calculated by a weak form which is a volume integral over the element $E(I)$. On each node I at the boundary $\partial E(I)$, variables and shape functions of the finite element discretization are known. This information suffices for their flux calculation at the boundary in the same way as the flux calculation for the inside of the domain. In the calculation of these terms, the surface integral obtained by the decomposition using the Green Theorem has to be taken into account when it is necessary, in particular near the wall.

The unsteady and convective terms are discretized by an approximation of finite volume type which balances the fluxes over a cell $C(I)$ surrounding the node I. At the boundaries of the domain, the balance of fluxes over this cell needs the evaluation of the fluxes which cross the boundary face, i.e. $C(I) \cap \partial\Omega_h$.

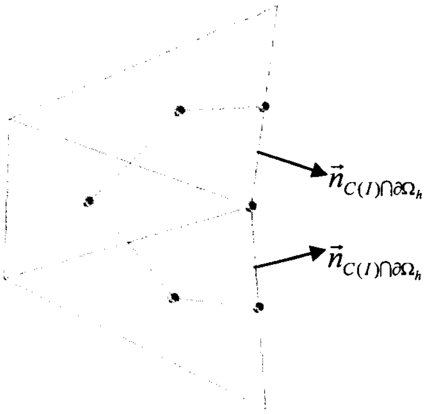

Fig. 4.1: *Boundary of the Cell $C(I)$*

The value of the unknown at the boundary, W_I^B, may be imposed by two methods [26]: first by using the weak formulation, through an imposed flux at the boundary face, i.e. $F_I = F_I^B$, second by using the strong formulation, through directly imposing the value at the boundary face, i.e. $W_I = W_I^B$.

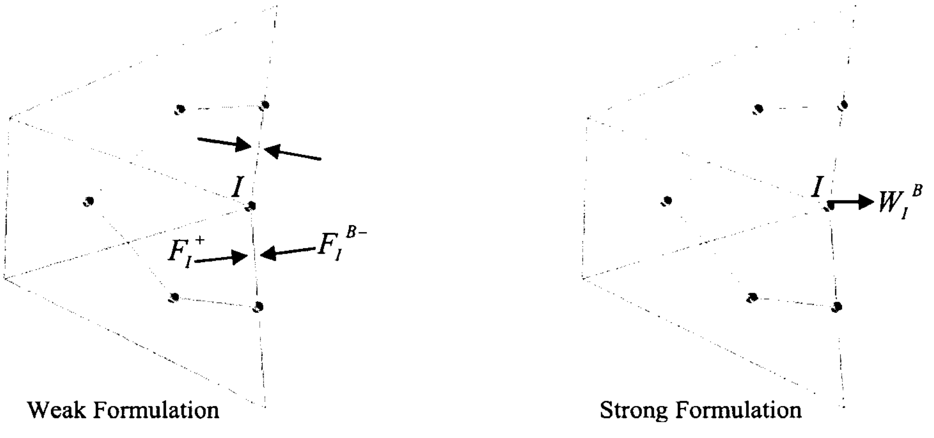

Weak Formulation

Strong Formulation

Fig. 4.2: *Different Methods for Boundary Condition Assignment*

4.1 Weak Formulation Methods

The boundary conditions using the weak formulation are imposed by determining the fluxes. In this case, according to the wave propagation direction which is discussed in the previous chapter, the flux at the boundary is decomposed to a contribution stemming from outgoing waves from interior domain based on the variable W_I, and another contribution arising from incoming waves base on the variable $W_I{}^B$. As proposed by Steger and Warming,

$$F_I{}^B = A^+(W_I)W_I + A^-(W_I{}^B)W_I{}^B \tag{4.1}$$

where, $A^+(W_I)$ and $A^-(W_I{}^B)$ are contributions of the Jacobian matrix of the convective fluxes from positive and negative eigenvalues, respectively. The Steger-Warming flux vector splitting method is given by [41],

$$F_{\pm}^{(n)} = \frac{\rho}{2\gamma}\begin{bmatrix} \alpha \\ \alpha u + c(\lambda_2{}^{\pm} - \lambda_3{}^{\pm})n_1 \\ \alpha v + c(\lambda_2{}^{\pm} - \lambda_3{}^{\pm})n_2 \\ \alpha w + c(\lambda_2{}^{\pm} - \lambda_3{}^{\pm})n_3 \\ \alpha \frac{q^2}{2} + c(\lambda_2{}^{\pm} - \lambda_3{}^{\pm})V_n + c^2 \frac{\lambda_2{}^{\pm} + \lambda_3{}^{\pm}}{\gamma - 1} \end{bmatrix} \tag{4.2}$$

where $q^2 = u^2 + v^2 + w^2$ and $\alpha = 2(\gamma - 1)\lambda_1{}^{\pm} + \lambda_2{}^{\pm} + \lambda_3{}^{\pm}$.

In practice, this decomposition does not permit the correct treatment of the supersonic boundaries. This results in constructing a unique Jacobian matrix from the interior state W_I,

$$F_I{}^B = A^+(W_I)W_I + A^-(W_I)W_I{}^B \tag{4.3}$$

This formulation is essentially applied on slip wall, inlet and outlet boundaries.

4.1.1 Slip Wall Boundary Conditions

On slip wall boundary faces, the normal component of velocity is zero $\vec{u} \cdot \vec{n} \equiv u_n = 0$ in which $\vec{n}$ is the outward normal vector at the boundary. The contribution of the viscous flux is assumed to be negligible hence $\vec{F}_j \cdot \vec{n}_j = {}^c\vec{F}_j \cdot \vec{n}_j$. Normal convective flux at the wall is written as,

$$ {}^c\vec{F}_j \cdot \vec{n}_j = \begin{bmatrix} 0 \\ pn_1 \\ pn_2 \\ pn_3 \\ 0 \end{bmatrix} \tag{4.4} $$

Pressure can be determined as a function of conservative variable, i.e. $p = (\gamma - 1)\left[\rho e - 1/2\, \rho u_i{}^2\right]$. The Jacobian of the corrected convective flux is written as,

$$ A_n = \begin{bmatrix} 0 & 0 & 0 & 0 & 0 \\ \left[c^2 - (\gamma-1)\left(h - |\vec{u}|^2\right)\right]n_1 & (2-\gamma)u_1 n_1 & -(\gamma-1)u_2 n_1 & -(\gamma-1)u_3 n_1 & (\gamma-1)n_1 \\ \left[c^2 - (\gamma-1)\left(h - |\vec{u}|^2\right)\right]n_2 & -(\gamma-1)u_1 n_2 & (2-\gamma)u_2 n_2 & -(\gamma-1)u_3 n_2 & (\gamma-1)n_2 \\ \left[c^2 - (\gamma-1)\left(h - |\vec{u}|^2\right)\right]n_3 & -(\gamma-1)u_1 n_3 & -(\gamma-1)u_2 n_3 & (2-\gamma)u_3 n_3 & (\gamma-1)n_3 \\ 0 & 0 & 0 & 0 & 0 \end{bmatrix} \tag{4.5} $$

4.1.2 Inlet and Outlet Boundary Conditions

The inlet and outlet boundary conditions are based on the characteristic properties of the governing equations. Namely, on account of hyperbolicity of the Euler equations, the solution can be written as superposition of waves propagating in computational domain. These waves are associated with the eigenvalues of the Jacobian matrix of the flux vectors. The Eigenvalues are $\vec{u} \cdot \vec{n}$, $\vec{u} \cdot \vec{n}$, $\vec{u} \cdot \vec{n}$, $\vec{u} \cdot \vec{n} + c$, and $\vec{u} \cdot \vec{n} - c$ which represent the propagation speed of the information waves in the direction $\vec{n}$. The figure below shows the domain of influence of the waves at the boundary which dictates the number of boundary conditions,

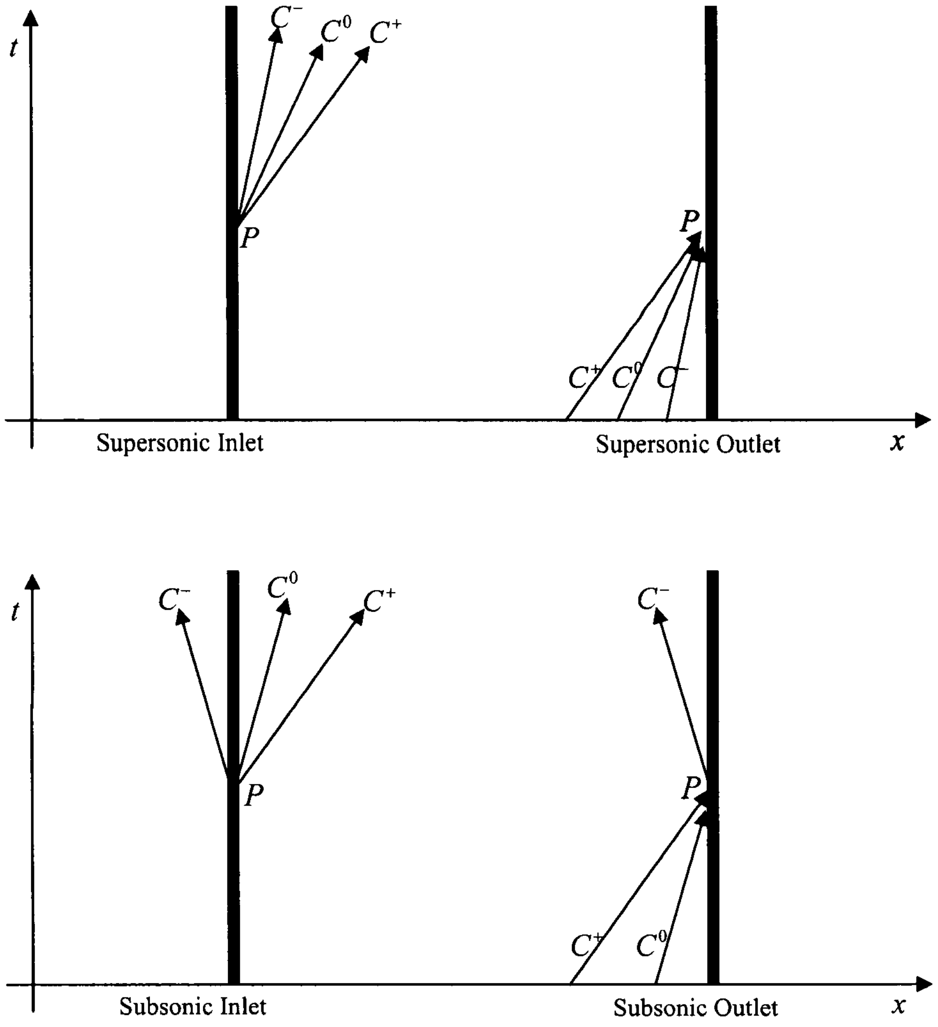

Fig. 4.3: *Characteristic Waves at the Boundary*

The sign of the eigenvalues, as depicted above, determines whether the wave is going out or coming in. Positive eigenvalues correspond to incoming and negative ones to outgoing characteristic waves. For incoming waves the physical conditions should be imposed, while for outgoing waves only numerical conditions are imposed which means the corresponding variables should be found using information coming from the interior points. Compatibility relations can be used to make sure that the outgoing waves are not reflected at the boundary. This is ensured by imposing the change in characteristic variable of the corresponding wave to be zero, leading to *non-reflecting boundary conditions*.

The number of the conditions to be imposed at a boundary is related to the information entering or leaving the boundary, i.e. the number of bi-characteristics [26]. Bi-characteristic propagation parallel to the boundary surface neither leaves nor enters the computational domain. So only the normal projection of bi-characteristic propagation has significance in transferring the information, namely the bi-characteristics associated with the vector $\vec{k} = \vec{n}$. Characteristic variables in this direction are,

$$\delta W_1 = \delta\rho - \frac{1}{c^2}\delta p \tag{4.6}$$

$$\delta W_2 = k_1\delta u_3 - k_3\delta u_1 = \left(\vec{k}\times\vec{e}_2\right)\cdot\delta\vec{u} \tag{4.7}$$

$$\delta W_3 = k_2\delta u_1 - k_1\delta u_2 = \left(\vec{e}_3\times\vec{k}\right)\cdot\delta\vec{u} \tag{4.8}$$

$$\delta W_4 = \vec{k}\cdot\delta\vec{u} + \frac{1}{\rho c}\delta p \tag{4.9}$$

$$\delta W_5 = -\vec{k}\cdot\delta\vec{u} + \frac{1}{\rho c}\delta p \tag{4.10}$$

and the corresponding compatibility relations are written as,

$$\left(\frac{\partial}{\partial t} + \vec{u}\cdot\vec{\nabla}\right)W_1 = 0 \quad \text{Entropy Wave} \tag{4.11}$$

$$\left(\frac{\partial}{\partial t}+\vec{u}\cdot\vec{\nabla}\right)W_2-\frac{c}{2}\left(\hat{e}_2\times\vec{k}\right)\cdot\vec{\nabla}\left(W_4+W_5\right)=0 \quad \text{Vorticity Wave} \tag{4.12}$$

$$\left(\frac{\partial}{\partial t}+\vec{u}\cdot\vec{\nabla}\right)W_3-\frac{c}{2}\left(\hat{e}_3\times\vec{k}\right)\cdot\vec{\nabla}\left(W_4+W_5\right)=0 \quad \text{Vorticity Wave} \tag{4.13}$$

$$\left[\frac{\partial}{\partial t}+\left(\vec{u}+c\vec{k}\right)\cdot\vec{\nabla}\right]W_4+c\vec{k}\cdot\left(\vec{k}\cdot\vec{\nabla}\right)\vec{u}=0 \quad \text{Entering Acoustic Wave} \tag{4.14}$$

$$\left[\frac{\partial}{\partial t}+\left(\vec{u}-c\vec{k}\right)\cdot\vec{\nabla}\right]W_5+c\vec{k}\cdot\left(\vec{k}\cdot\vec{\nabla}\right)\vec{u}=0 \quad \text{Exiting Acoustic Wave} \tag{4.15}$$

For a problem to be well-posed the range of influence of boundary conditions should encompass the entire computational domain [28].

Number of physical boundary conditions is shown in table below for different flow regime. As the equations govern five variables, the same number of variables has to be imposed at each boundary. The remaining variables have to be determined by a numerical procedure compatible with the physical conditions and numerical scheme using the solution of the interior points.

Table 4.1: *Number of Boundary Conditions in Different Regimes of the flow*

	Inlet		Outlet	
	Supersonic	Subsonic	Supersonic	Subsonic
Physical Condition	5	4	0	1
Numerical Condition	0	1	5	4
Incoming	$C_0 : \vec{u}\cdot\vec{n} > 0$	$C_0 : \vec{u}\cdot\vec{n} > 0$		$C_+ : \vec{u}\cdot\vec{n} + c > 0$

Wave	$C_+ : \vec{u}\cdot\vec{n}+c>0$ $C_- : \vec{u}\cdot\vec{n}-c>0$	$C_+ : \vec{u}\cdot\vec{n}+c>0$		
Outgoing Wave		$C_- : \vec{u}\cdot\vec{n}-c<0$	$C_0 : \vec{u}\cdot\vec{n}<0$ $C_+ : \vec{u}\cdot\vec{n}+c<0$ $C_- : \vec{u}\cdot\vec{n}-c<0$	$C_0 : \vec{u}\cdot\vec{n}<0$ $C_- : \vec{u}\cdot\vec{n}-c<0$

The variables that are usually fixed are given in table below, where α_{attack} is the flow angle of attack,

Table 4.2: *Fixed Variables at Boundaries*

Inlet		Outlet	
Supersonic	Subsonic	Supersonic	Subsonic
T_t, u_1, u_2, u_3, p_t	T_t, α_{attack}, p_t		p_t
T, u_1, u_2, u_3, p	T, α_{attack}, p		p

4.2 Strong Formulation Methods

The boundary conditions using the strong formulation are imposed by determining the variables at the node. The explicit temporal discretization of the governing equations can be written in the following form,

$$\frac{\Delta W}{\Delta t} = -\frac{1}{vol(C(I))}R \tag{4.16}$$

The boundary conditions consist of prescribing the variation of the conservative variable ΔW_I at the iteration $\bullet^{n+1}$ from its value at the iteration $\bullet^{n}$.

The boundary condition can be written in the general form as follows,

$$B(W) = 0 \tag{4.17}$$

Its linear representation in time permits writing its temporal discrete form as given below,

$$\frac{\partial B(W)}{\partial W}\Delta W = 0 \tag{4.18}$$

This formulation is essentially applied on symmetry, and wall boundaries.

4.2.1 Symmetry Boundary Conditions

On symmetry boundary faces, the component of velocity normal to the boundary is zero $\vec{u}\cdot\vec{n} \equiv u_n = 0$. Hence, in the boundary formulation the normal component of velocity and the increment of the corresponding flux are zero,

$$W[1] = 0 \tag{4.19}$$

$$R[1] = 0 \tag{4.20}$$

No other condition is imposed on other variables.

4.2.2 Wall Boundary Conditions

On the adiabatic wall the following conditions are imposed,

$$\vec{u} = 0 \quad \text{Non-slip Condition} \tag{4.21}$$

$$\nabla T\cdot\vec{n} = 0 \quad \text{Adiabatic Condition} \tag{4.22}$$

$$\rho_{,t} + \nabla\cdot(\rho\vec{u}) = 0 \quad \text{Continuity} \tag{4.23}$$

Therefore, using primitive variables $Y^T = [\rho, u_1, u_2, u_3, T]$,

$$B(Y)^T = [\rho_{,t} + \nabla\cdot(\rho\vec{u}), u, v, w, \nabla T\cdot\vec{n}] \tag{4.24}$$

where $\vec{n}$ is the outward normal at the boundary. First order linearization of the above equations in time is given below,

$$\left(\frac{\partial\vec{u}}{\partial t}\right) = \frac{\vec{u}^{n+1} - \vec{u}^{n}}{\Delta t} \tag{4.25}$$

$$\left(\frac{\partial\nabla T\cdot\vec{n}}{\partial t}\right) = \frac{(\nabla T\cdot\vec{n})^{n+1} - (\nabla T\cdot\vec{n})^{n}}{\Delta t} \tag{4.26}$$

$$\frac{\partial\rho}{\partial t} = -\nabla\cdot(\rho\vec{u})^n \tag{4.27}$$

therefore,

$$\frac{\partial B(V)}{\partial Y}\frac{\partial Y}{\partial t} = \left[-\nabla\cdot(\rho\vec{u})^n, -\frac{u_1}{\Delta t}, -\frac{u_2}{\Delta t}, -\frac{u_3}{\Delta t}, -\frac{(\nabla T\cdot\vec{n})^n}{\Delta t}\right]^T \tag{4.28}$$

The temperature is calculated using conservative variables as

$$T = \frac{\gamma-1}{R_g}e - \frac{1}{2}\left(u_1^2 + u_2^2 + u_3^2\right) \tag{4.29}$$

Gradient of temperature in the normal direction of the wall is calculated using interior points and a non-centered method.

In case of Neumann boundary conditions, i.e. giving the normal derivatives on boundary, the space gradients are discretized by a non-centered second order method. In practice, the physical boundary conditions are often expressed in terms of the primitive variables. This requires using the transformation matrices described in previous chapter.

In case of Dirichelet boundary conditions, i.e. giving the value of the variables on the boundary, it is easier to assign the value to the variable and then mask it from calculations. But in cases where this value is time dependent, the strong formulation has to be used.

4.3 Periodic Boundary Conditions

Periodic boundaries are treated completely different from other types of boundaries in that there is no need to impose any value or calculate any flux through these faces. The corresponding periodic faces and nodes have to be identified in the pre-processing stage. Then, by logically wrapping the geometry, a periodic face is replaced by its corresponding periodic shadow as shown in figure below. In this process, new edges have to be created and some edges have to be deleted after periodic node replacements. This process is shown in figure 4.4. The idea is that only the periodic shadow node has to be substituted by its periodic corresponding node. Hence, all the edges that have a periodic shadow node as a member, have to be deleted and new edges have to be created by replacing the periodic point by periodic shadow points on such edges. Also, there are some edges that contain only members that are periodic shadow points. Those edges have to be destroyed without creating any new edge in exchange for them.

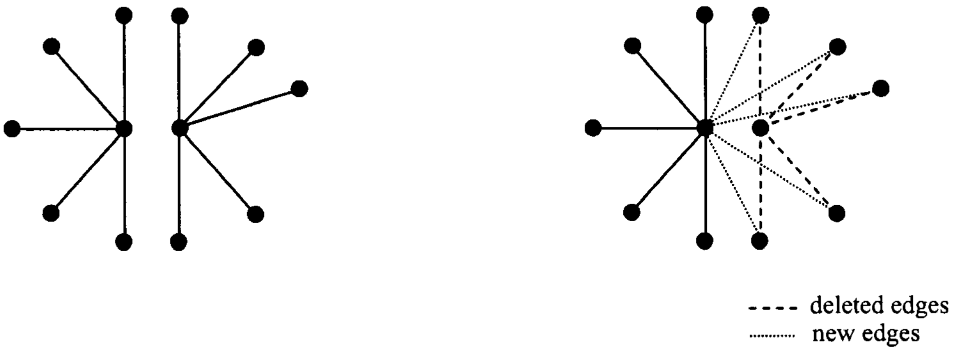

Fig. 4.4: The Process of Making Two Faces Periodic

The preceding method works fine in the serial code. However, for the parallel version of the computational code, as the periodic nodes can belong to different sub-domains which do not have access to each other's data structure the method is no longer applicable. For parallel application, instead of creating new edges, the fluxes and other variables at corresponding periodic nodes are exchanged according to MPI standards. So, each time a variable is calculated for a node or an edge, if that node or edge has a periodic corresponding node, the calculated variable has to be exchanged between the nodes or edges.

4.4 Computational Domain

The computational domain is shown below,

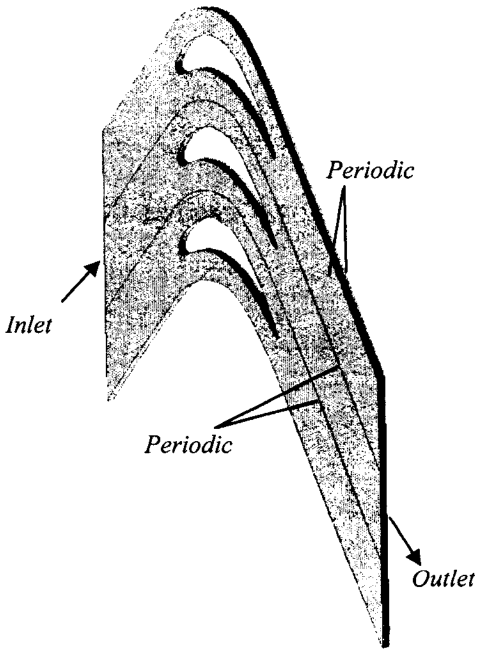

Fig. 4.5: *Computational Domain and Boundary Conditions*

Subsonic/Supersonic inlet and outlet boundary condition, according to the method of characteristics, is constructed by imposing total pressure, total temperature and flow angle at inlet plane as well as back static pressure at outlet plane. Non-slip and adiabatic conditions are imposed at walls. The upper and lower surfaces of the computational domain have been made periodic. To limit the massive number of grid points, the domain spanwise length is only 10% of the chord length and then two lateral surfaces are made periodic. The choice of periodic lateral walls allows for the 3D turbulence structured growing and it is closer to the test conditions. Imposing slip conditions in this situation forces the flow structures to be 2D. As turbulence does not exist in two dimensions physically, in LES the lateral faces have to periodic in contrary to RANS simulation with slip walls. Also, shortage of the spanwise length can have a similar effect especially in off-design conditions. The test conditions and the effect of spanwise length is more elaborated on in chapter 6: Results and Discussion. The results are gathered at half the span conforming to the experimental measurements.

Chapter 5

LARGE EDDY SIMULATION OF TURBULENCE

5.1 Physics of Turbulence

Turbulence is a phenomenon in fluids in which high velocity gradients leads to disturbances in the flow which are function of space and time. Physically, turbulent flow is considered as the superposition of eddies of different scales with a continuous energy spectrum [42]. The length scale l_0 and velocity scale U_0 of eddies in the largest size range of the flow are comparable with length scales and velocity scales of the flow. Hence, Reynolds number of such eddies is comparable to flow Reynolds number and it is high; therefore effects of viscosity in those scales are small. Large eddies are unstable and they break into the smaller eddies and by this process they transfer energy to smaller scales. Smaller eddies have smaller length and velocity scales; consequently they have a smaller Reynolds number $\mathrm{Re} = U_l.l/\nu$. The vortex break-up phenomenon continues until eddies' scales and their Reynolds number are sufficiently small so that the eddy motion becomes stable and molecular viscosity becomes effective in dissipating the kinetic energy. The smallest eddies are characterized by Kolmogorov scales. Flow scales are shown in figure 5.1 below.

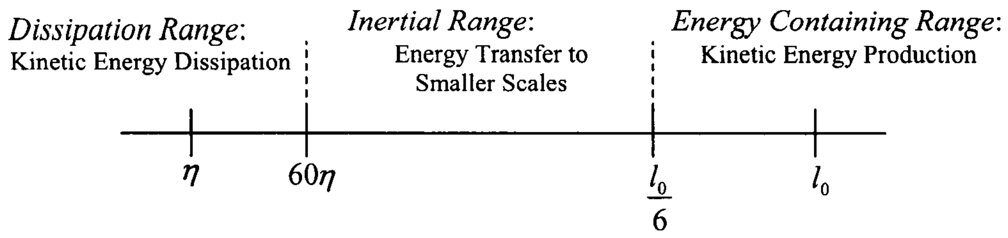

***Fig. 5.1:** Flow Scales*

According to Kolmogorov hypotheses, at sufficiently high Reynolds number the small scale motions ($l < (l_0/6)$) are statistically isotropic. The turbulence kinetic energy is produced in the large anisotropic scales ($l > (l_0/6)$). Then it will be transferred to smaller scales in the inertial range. The statistics of the flow in this range ($60\eta < l < (l_0/6)$) is only a function of ε, i.e. dissipation rate. Afterwards, the turbulent kinetic energy will be dissipated in the dissipation range. The statistics of the flow in this range ($l < 60\eta$) is dependent on both ε and ν.

Using dimensional analysis and having rate of energy dissipation ε and viscosity ν, the Kolmogorov length, velocity, and time scales can be found as, $\eta \equiv (\nu^3/\varepsilon)^{1/4}$, $U_\eta \equiv (\varepsilon\nu)^{1/4}$, and $t_\eta \equiv (\nu/\varepsilon)^{1/2}$ respectively. Reynolds number based on Kolmogorov scales is $\mathrm{Re}_\eta = U_\eta.\eta/\nu = 1$. These relations give the dissipation rate as $\varepsilon = (\nu/t_\eta^{\,2}) = \nu/(U_\eta/\eta)^2$. However, rate of the energy dissipation scale has to scale with the rate of the energy transfer to smaller scale motions, i.e. $U_0^{\,2}/t_0 = U_0^{\,3}/l_0$. The ratio of the smallest to largest scales of the flow can be determined from the previous statements as: $\eta/l_0 \approx \mathrm{Re}^{-3/4}$, $U_\eta/U_0 \approx \mathrm{Re}^{-1/4}$, and $t_\eta/t_0 \approx \mathrm{Re}^{-1/2}$.

A motion with length scale of l corresponds to wavenumber $\kappa = 2\pi/l$. Using a Fourier transform, the energy can be taken to the wavenumber space to obtain the energy spectrum function $E(\kappa)$. The contribution to the total kinetic energy from all modes in the range (κ_a, κ_b) is given by $\int_{\kappa_a}^{\kappa_b} E(\kappa)\,d\kappa$. Obviously the total kinetic energy is given by $\int_0^{\infty} E(\kappa)\,d\kappa = \int_{\Omega} \frac{1}{2}\bar{\rho}\widetilde{u}_i\widetilde{u}_i\,d\Omega$. This continuous energy spectrum function is shown in figure 6.2. In the inertial range the spectrum is $E(\kappa) = C\varepsilon^{2/3}\kappa^{-5/3}$ where C is a universal constant.

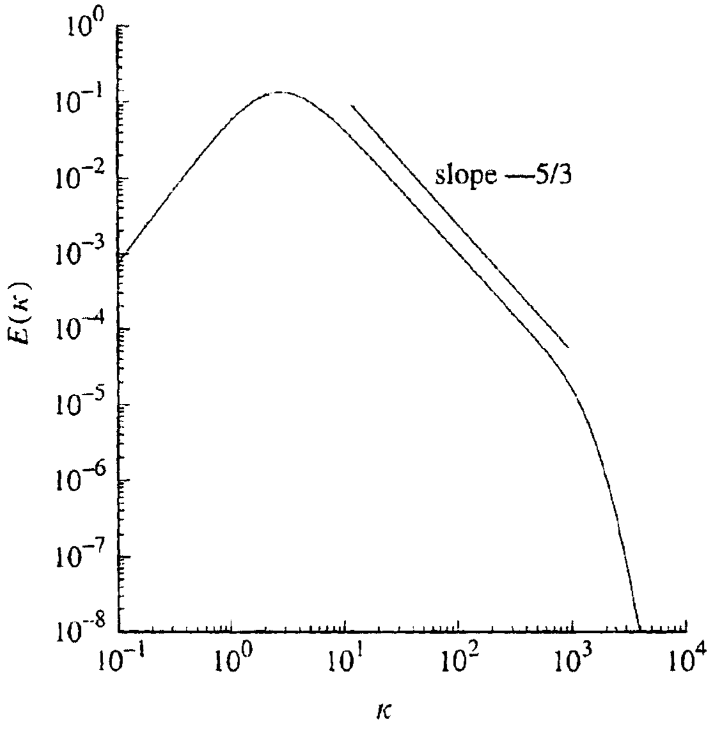

***Fig. 5.2:** Energy Spectrum Function [42]*

5.2 Turbulence Modeling and LES

The governing equations of the flow do not change in turbulent flow, hence using a dense enough mesh, all scales of the flow can be simulated. This method is called *Direct Numerical Simulation* (DNS). However, due to the high cost of such a deterministic analysis, DNS is not applicable to problems with high Reynolds numbers due to the existence of the extremely small scales.

In practice, owing to the fact that turbulent flows are characterized by random fluctuations, statistical methods are applied to governing equations which can be of time-average or spatial-average nature. Ensemble averaging the flow equations results in *Reynolds Average Navier-Stokes* (RANS) methods in which mean quantities are separated from fluctuations. Hence, all scales of the flow are modeled and far less mesh refinement is needed to simulate turbulence compared to DNS. Averaging leads to new terms that need modeling for closure. In *zero-Equation* models, the closure is achieved by using Prandtl mixing length model leading to algebraic equations for eddy viscosity. In general, zero-equation models fail to perform well in regions of recirculation and separated flows [43]. Eddy viscosity can also be obtained more accurately by solving one or two other differential equations for turbulent kinetic energy, turbulent kinetic energy dissipation, or vorticity, which leads to *one-* or *two-equation* models. In general, the effects of streamline curvature, sudden changes in strain rate, secondary motion, etc. can not be accommodated in these models [43]. Furthermore, all RANS methods are accompanied by several empirical constants which are mostly known for incompressible flows.

Large Eddy Simulation (LES) is a compromise between RANS and DNS methods in which large scales of the flow are *simulated* while only small scales are *modeled.* Performance and abilities of LES is between RANS and DNS. The LES filter width Δ prescribe the large scales which are larger than Δ and small scales which are smaller than Δ. The filter width is related to the mesh size. Since the large scales are simulated, the mesh resolution is much finer than RANS but it is quite larger than DNS mesh which resolve all the scales. However, modeling of LES sub-grid scale terms is simpler than RANS closure terms modeling on the account that small scales are expected to be more universal. The ideal application of the LES is in the case of high Reynolds number flow and with the filter width in the inertial range. Also, the mesh has to be fine enough to resolve at least 80% of the energy and close to the walls it has to be in the order of viscous length scale δ_v ($y^+ \approx 1$) which is the size of important near wall motions.

Simulation of the large scales of the flow is obtained by applying a spatial filter throughout the computational domain. In this way, each flow variable ϕ can be decomposed to a resolved component of the large scale $\bar{\phi}$, and an unresolved component of the sub-grid or small scale ϕ'.

$$\phi = \bar{\phi} + \phi' \tag{5.1}$$

In contrary to Reynolds averaging, for filtering operation one can obtain

$$\bar{\bar{\phi}} \neq \bar{\phi} \quad , \quad \overline{\phi''} \neq 0 \tag{5.2}$$

The spatial low pass filter can be defined as follows, where $\bar{f}$ is the large scale part of a variable f,

$$\bar{f} = \int_{\Omega} G_{\Delta}(x-\xi) f(\xi) d\xi \tag{5.3}$$

In general, the filtering operation is supposed to commute with spatial and temporal derivatives, with an error in the order of the numerical approximation error.

$$\overline{\frac{\partial \phi}{\partial t}} = \frac{\partial \overline{\phi}}{\partial t} \quad , \quad \overline{\frac{\partial \phi}{\partial x_i}} = \frac{\partial \overline{\phi}}{\partial x_i} \tag{5.4}$$

Filtering gives the governing equations of the large scales of the flow. Filtering non-linear terms also results in some terms which signify the effect of the small scales of the flow on the large scale. These terms are called sub-grid terms and need modeling for closure. Hence, the two major steps in LES are filtering and sub-grid scale (SGS) modeling. Filtering as well as SGS modeling can be accomplished implicitly or explicitly. In the rest of this section, first the filtered governing equations will be derived and then explicit and implicit methods for SGS modeling and filtering, which are used in this thesis, will be discussed.

5.3 Filtered Governing Equations

Using Favre [44] filter for compressible flow, in which the filter is balanced by the mass, the decomposition is written as,

$$\begin{aligned} \varphi &= \frac{\overline{\rho\varphi}}{\overline{\rho}} + \varphi' \\ \varphi &\equiv \tilde{\varphi} + \varphi' \end{aligned} \tag{5.5}$$

and sub-grid terms are avoided in continuity equations. Favre filter produces simpler governing equations which are more similar to the original Navier-Stokes equations; however, this filter generally does not commute with the partial differential operator [43]. The filtered Navier-Stokes equations can be filtered in different ways whether or not Favre averaging is used as discussed below.

5.3.1 Filtering Using Favre Average

Here we follow the derivation of Vreman et al. [45]. Non-dimensional Navier-Stokes system of equations can be written as,

$$\frac{\partial \rho}{\partial t}+\frac{\partial \rho u_i}{\partial x_i}=0 \tag{5.6}$$

$$\frac{\partial \rho u_i}{\partial t}+\frac{\partial \rho u_i u_j}{\partial x_j}+\frac{\partial p}{\partial x_i}-\frac{\partial \sigma_{ij}}{\partial x_j}=0 \tag{5.7}$$

$$\frac{\partial \rho e}{\partial t}+\frac{\partial \rho e u_i}{\partial x_i}+\frac{\partial p u_i}{\partial x_i}-\frac{\partial \sigma_{ij} u_i}{\partial x_j}+\frac{\partial q}{\partial x_i}=0 \tag{5.8}$$

The constitutive equations are written as,

$$\rho e=\rho e(\rho,\vec{u},p)=p/(\gamma-1)+1/2\,\rho u_k u_k \tag{5.9}$$

$$\sigma_{ij}=\sigma_{ij}(\vec{u},T)=(\mu(T)/\mathrm{Re})\left((u_{i,j}+u_{j,i})-\frac{2}{3}u_{k,k}\delta_{ij}\right) \tag{5.10}$$

$$q_i=q_i(T)=\frac{\mu(T)}{\gamma-1}\frac{1}{\mathrm{Pr}}\frac{1}{\mathrm{Re}}T_{,i} \tag{5.11}$$

$$T=T(\rho,p)=p/\rho \tag{5.12}$$

The system of equations in functional form is,

$$NS(\rho,\vec{u},p,e,\sigma,q)=0 \tag{5.13}$$

The filtered Navier-Stokes equations using Favre average can be written in two forms depending on how to filter the energy equation.

System (I) can be obtained by using filtered pressure and modifying total energy as,

$$NS(\overline{\rho},\widetilde{\vec{u}},\overline{p},\widehat{e},\widehat{\sigma},\widehat{q})=\widehat{R}_{SGS} \tag{5.14}$$

$$\widehat{e}=e(\overline{\rho},\widetilde{\vec{u}},\overline{p}) \tag{5.15}$$

$$\hat{\sigma}_{ij} = \sigma_{ij}(\tilde{\vec{u}}, \tilde{T}) \tag{5.16}$$

$$\hat{q}_i = q_i(\tilde{T}) \tag{5.17}$$

$$\tilde{T} = T(\bar{\rho}, \bar{p}) \tag{5.18}$$

With,

$$\hat{R}_{SGS} = \begin{bmatrix} 0 \\ A_1 + A_2 \\ B_1 + B_2 + B_3 + B_4 + B_5 + B_6 + B_7 \end{bmatrix} \tag{5.19}$$

System(II), which is used in the present work, is obtained by using filtered energy and modifying pressure as given below in more details,

$$\overline{\rho e} = \rho e(\bar{\rho}, \tilde{\vec{u}}, \breve{p}) = \bar{p}/(\gamma - 1) + 1/2\,\bar{\rho}\tilde{u}_k\tilde{u}_k + 1/2\,\bar{\rho}\tau_{kk} \tag{5.20}$$

where $\tau_{ij} = \tilde{u}_i\tilde{u}_j - \overleftrightarrow{u_i u_j}$, leading to modified pressure and temperature as follows,

$$\breve{p} = (\gamma - 1)(\bar{e} - 1/2\,\bar{\rho}\tilde{u}_k\tilde{u}_k) = \bar{p} + (\gamma - 1)/2\,\bar{\rho}\tau_{kk} \tag{5.21}$$

$$\breve{T} = T(\bar{\rho}, \breve{p}) = \breve{p}/\bar{\rho} = \bar{T} + (\gamma - 1)/2\,\tau_{kk} \tag{5.22}$$

The other constitutive equations are given as,

$$\bar{q}_i = q_i(\overline{\mu(T)}, \bar{T}) \quad \text{And} \quad \breve{q}_i = q_i(\mu(\breve{T}), \breve{T}) \tag{5.23}$$

$$\bar{\sigma}_{ij} = \sigma_{ij}(\overline{\mu(T)}, \bar{\vec{u}}) \quad \text{And} \quad \breve{\sigma}_{ij} = \sigma_{ij}(\mu(\breve{T}), \tilde{\vec{u}}) \tag{5.24}$$

The filtered governing equation are written as,

$$\frac{\partial \bar{\rho}}{\partial t} + \frac{\partial \bar{\rho}\tilde{u}_i}{\partial x_i} = 0 \tag{5.25}$$

$$\begin{aligned} \frac{\partial \bar{\rho}\tilde{u}_i}{\partial t} + \frac{\partial \bar{\rho}\tilde{u}_i\tilde{u}_j}{\partial x_j} + \frac{\partial \breve{p}}{\partial x_i} - \frac{\partial \breve{\sigma}_{ij}}{\partial x_j} &= \frac{\partial \bar{\rho}\left(\tilde{u}_i\tilde{u}_j - \overleftrightarrow{u_i u_j}\right)}{\partial x_j} + \frac{\partial(\breve{p} - \bar{p})}{\partial x_i} - \frac{\partial(\bar{\sigma}_{ij} - \breve{\sigma}_{ij})}{\partial x_j} \\ &= \quad C_1 \quad + \quad C_2 \quad + \quad C_3 \end{aligned} \tag{5.26}$$

With,

$$\frac{\partial\left(\breve{p}-\overline{p}\right)}{\partial x_i}=\frac{\partial\left(\left(\gamma-1\right)/2\,\overline{\rho}a_{kk}\right)}{\partial x_i} \tag{5.27}$$

$$\frac{\partial\overline{\rho e}}{\partial t}+\frac{\partial\overline{\rho e}\widetilde{u}_i}{\partial x_i}+\frac{\partial\breve{p}\widetilde{u}_i}{\partial x_i}-\frac{\partial\breve{\sigma}_{ij}\widetilde{u}_i}{\partial x_j}+\frac{\partial\breve{q}_i}{\partial x_i}=\frac{\partial\left(\overline{\rho e}\widetilde{u}_i-\overline{\rho e u_i}\right)}{\partial x_i}+\frac{\partial\left(\breve{p}\widetilde{u}_i-\overline{pu_i}\right)}{\partial x_i}-\frac{\partial\left(\breve{\sigma}_{ij}\widetilde{u}_i-\overline{\sigma_{ij}u_i}\right)}{\partial x_j}+\frac{\partial\left(\breve{q}_i-\overline{q}_i\right)}{\partial x_i} \tag{5.28}$$

Considering,

$$\frac{\partial\left(\overline{\rho e}\widetilde{u}_i\right)}{\partial x_i}=\frac{\partial\left(\left(\breve{p}/\left(\gamma-1\right)+1/2\,\overline{\rho}\widetilde{u}_k\widetilde{u}_k\right)\widetilde{u}_i\right)}{\partial x_i}=\frac{1}{\gamma-1}\frac{\partial\left(\breve{p}\widetilde{u}_i\right)}{\partial x_i}+\frac{\partial\left(1/2\,\overline{\rho}\widetilde{u}_k\widetilde{u}_k\widetilde{u}_i\right)}{\partial x_i} \tag{5.29}$$

And,

$$-\frac{\partial\left(\overline{\rho e u_i}\right)}{\partial x_i}=-\frac{\partial\left(\overline{\left(p/\left(\gamma-1\right)+1/2\,\rho u_k u_k\right)u_i}\right)}{\partial x_i}=\frac{-1}{\gamma-1}\frac{\partial\left(\overline{pu_i}\right)}{\partial x_i}-\frac{\partial\left(1/2\,\overline{\rho u_k u_k u_i}\right)}{\partial x_i} \tag{5.30}$$

Leads to,

$$\frac{\partial\left(\overline{\rho e}\widetilde{u}_i-\overline{\rho e u_i}\right)}{\partial x_i}=\frac{1}{\gamma-1}\frac{\partial\left(\breve{p}\widetilde{u}_i-\overline{pu_i}\right)}{\partial x_i}+\frac{\partial\left(1/2\,\overline{\rho}\widetilde{u}_k\widetilde{u}_k\widetilde{u}_i-1/2\,\overline{\rho u_k u_k u_i}\right)}{\partial x_i} \tag{5.31}$$

Also,

$$\frac{\partial\left(\breve{p}\widetilde{u}_i-\overline{pu_i}\right)}{\partial x_i}=\frac{\partial\left(\left(\overline{p}+\left(\gamma-1\right)/2\,\overline{\rho}a_{kk}\right)\widetilde{u}_i-\overline{pu_i}\right)}{\partial x_i}=\frac{\partial\left(\overline{p}\widetilde{u}_i-\overline{pu_i}\right)}{\partial x_i}+\frac{\partial\left(\left(\gamma-1\right)/2\,\overline{\rho}a_{kk}\widetilde{u}_i\right)}{\partial x_i} \tag{5.32}$$

Hence the first two terms on the right hand side of the energy equation are,

$$\begin{aligned}\frac{\partial\left(\overline{\rho e}\widetilde{u}_i-\overline{\rho e u_i}\right)}{\partial x_i}+\frac{\partial\left(\breve{p}\widetilde{u}_i-\overline{pu_i}\right)}{\partial x_i}&=\frac{\gamma}{\gamma-1}\frac{\partial\left(\overline{p}\widetilde{u}_i-\overline{pu_i}\right)}{\partial x_i}+\frac{\partial\left(1/2\,\overline{\rho}\widetilde{u}_k\widetilde{u}_k\widetilde{u}_i-1/2\,\overline{\rho u_k u_k u_i}\right)}{\partial x_i}+\frac{\partial\left(\left(\gamma-1\right)/2\,\overline{\rho}a_{kk}\widetilde{u}_i\right)}{\partial x_i}\\&=\quad D_1\quad+\quad D_2\quad+\quad D_3\end{aligned} \tag{5.33}$$

And the last two terms are,

$$-\frac{\partial\left(\breve{\sigma}_{ij}\widetilde{u}_i-\overline{\sigma_{ij}u_i}\right)}{\partial x_j}+\frac{\partial\left(\breve{q}_i-\overline{q}_i\right)}{\partial x_i}=D_4+D_5 \tag{5.34}$$

This derivation in functional form is written as,

$$NS(\bar{\rho}, \tilde{\vec{u}}, \breve{p}, \overline{\rho e}, \breve{\sigma}, \breve{q}) = \breve{R}_{SGS} \tag{5.35}$$

$$\overline{\rho e} = \rho e(\bar{\rho}, \tilde{\vec{u}}, \breve{p}) \tag{5.36}$$

$$\breve{\sigma}_{ij} = \sigma_{ij}(\mu(\breve{T}), \tilde{\vec{u}}) \tag{5.37}$$

$$\breve{q}_i = q_i(\mu(\breve{T}), \breve{T}) \tag{5.38}$$

$$\breve{T} = T(\bar{\rho}, \breve{p}) \tag{5.39}$$

With,

$$\breve{R}_{SGS} = \begin{bmatrix} 0 \\ C_1 + C_2 + C_3 \\ D_1 + D_2 + D_3 + D_4 + D_5 \end{bmatrix} \tag{5.40}$$

In which pressure and temperature are modified. The sub-grid terms are given in the table below, where $\partial_i \bullet = \partial/\partial x_i$,

***Table 5.1:** Sub-Grid Scale Terms*

Equation	System (*I*)		System (*II*)	
	Symbol	Expression	Symbol	Expression
Momentum	A_1	$\partial_j(\bar{\rho}\tau_{ij})$	C_1	$\partial_j(\bar{\rho}\tau_{ij})$
	A_2	$-\partial_j(\breve{\sigma}_{ij} - \bar{\sigma}_{ij})$	C_2	$\partial_i((\gamma-1)/2\,\bar{\rho}\tau_{kk})$
			C_3	$-\partial_j(\breve{\sigma}_{ij} - \bar{\sigma}_{ij})$
Energy	B_1	$\frac{1}{\gamma-1}\partial_i(\bar{p}\tilde{u}_i - \overline{pu_i})$	D_1	$\frac{\gamma}{\gamma-1}\partial_i(\bar{p}\tilde{u}_i - \overline{pu_i})$
	B_2	$\bar{p}\,\partial_k\tilde{u}_k - \overline{p\,\partial_k u_k}$	D_2	$\partial_i(1/2\,\bar{\rho}\tilde{u}_k\tilde{u}_k\tilde{u}_i - 1/2\,\overline{\rho u_k u_k u_i})$

	B_3	$-\partial_i\left(\overline{\rho}\tau_{ki}\widetilde{u}_k\right)$	D_3	$\partial_i\left(\left(\gamma-1\right)/2\,\overline{\rho}\tau_{kk}\widetilde{u}_i\right)$
	B_4	$\overline{\rho}a_{kj}\partial_j\widetilde{u}_k$	D_4	$-\partial_j\left(\breve{\sigma}_{ij}\widetilde{u}_i-\overline{\sigma_{ij}u_i}\right)$
	B_5	$\overline{\sigma_{kj}\partial_j u_k}-\sigma_{kj}\partial_j\widetilde{u}_k$	D_5	$\partial_i\left(\breve{q}_i-\overline{q}_i\right)$
	B_6	$-\partial_j\left(\breve{\sigma}_{ij}\widetilde{u}_i-\overline{\sigma_{ij}u_i}\right)$		
	B_7	$\partial_i\left(\breve{q}_i-\overline{q}_i\right)$		

In modeling, only sub-grid terms A_1, B_1, and B_3 from system (I) or C_1, C_2, and D_1 from system (II) are usually taken into account. Different tests can be carried out to show the significance of each term. *Priori LES Test* is carried out by filtering a DNS database in order to calculate turbulent stresses and compare them with the stresses prescribed by sub-grid models. Hence, it used only DNS methods. *Posteriori LES Test* is carried out by performing a LES study and comparing the results with those of filtered DNS. Vreman et al. [45] performed a priori LES test, using DNS results of a mixing layer using a top hat filter with width of 8 cells, and concluded that sub-grid models which incorporate energy equation should at least take into account the divergence pressure-velocity term B_1, pressure dilatation term B_2 and turbulent stress velocity term B_3. Also, it seems reasonable to neglect sub-grid terms that contain viscous stress or heat flux, which are relatively small in high Reynolds number flows. However, inviscid sub-grid terms, such as B_2 which is the pure effect of compressibility, should not be neglected. These results are summarized in the table below.

Table 5.2: *Classification of Sub-Grid Terms Based on Their Order of Magnitude*

Category	System (*I*)		System (*II*)	
	Momentum Eq.	Energy Eq.	Momentum Eq.	Energy Eq.
Large	$\partial_j\left(\overline{\rho}\widetilde{u}_i\widetilde{u}_j\right)+\partial_i\overline{p}$	$\partial_i\left(\left(\overline{\rho e}+\overline{p}\right)\widetilde{u}_i\right)$	$\partial_j\left(\overline{\rho}\widetilde{u}_i\widetilde{u}_j\right)+\partial_i\breve{p}$	$\partial_i\left(\left(\overline{\rho e}+\breve{p}\right)\widetilde{u}_i\right)$
Medium	$\partial_j\widehat{\sigma}_{ij}$	$\partial_j\left(\widehat{\sigma}_{ij}\widetilde{u}_i\right)$, $\partial_i\widehat{q}_i$	$\partial_j\breve{\sigma}_{ij}$	$\partial_j\left(\breve{\sigma}_{ij}\widetilde{u}_i\right)$, $\partial_i\breve{q}_i$
	A_1	B_1, B_2, B_3	$\left(C_1+C_2\right)$	D_1, D_2
Small		B_4, B_5		D_3, D_4, D_5
Negligible	A_2	B_6, B_7	C_3	

5.3.2 Filtering without Using Favre Average

Favre averaged equations are simpler and no model in necessary in continuity equations. Some information is lost in this process but it is not really a problem for relatively low Mach number flows. However, continuity is still a non-linear equation which can cause numerical instabilities leading to small grid point to grid point waves. This drawback can be removed by adding an artificial diffusion term to the right hand side of the equation or by averaging the governing equation without density weighting. In the latter approach the governing equations are derived, following Boersma and Lele [46], as,

$$\frac{\partial\overline{\rho}}{\partial t}+\frac{\partial\overline{\rho}\,\overline{u}_i}{\partial x_i}=\frac{\partial\left(\overline{\rho}\,\overline{u}_i-\overline{\rho u_i}\right)}{\partial x_i} \tag{5.41}$$

$$\frac{\partial\overline{\rho}\,\overline{u}_i}{\partial t}+\frac{\partial\overline{\rho}\,\overline{u}_i\,\overline{u}_j}{\partial x_j}+\frac{\partial\overline{p}}{\partial x_i}-\frac{\partial\overline{\sigma}_{ij}}{\partial x_j}=\frac{\partial\left(\overline{\rho}\,\overline{u}_i-\overline{\rho u_i}\right)}{\partial t}+\frac{\partial\left(\overline{\rho}\,\overline{u}_i\overline{u}_j-\overline{\rho u_i u_j}\right)}{\partial x_j} \tag{5.42}$$

$$\frac{\partial\overline{\rho e}}{\partial t}+\frac{\partial\overline{\rho e}\,\overline{u}_i}{\partial x_i}+\frac{\partial\overline{p}\,\overline{u}_i}{\partial x_i}-\frac{\partial\overline{\sigma}_{ij}\overline{u}_i}{\partial x_j}+\frac{\partial\overline{q}_i}{\partial x_i}=\frac{\partial\left(\overline{\rho e}\,\overline{u}_i-\overline{\rho e u_i}\right)}{\partial x_i}+\frac{\partial\left(\overline{p}\,\overline{u}_i-\overline{p u_i}\right)}{\partial x_i} \tag{5.43}$$

Where,

$$\overline{\sigma}_{ij}=\left(\mu(\overline{T})/\mathrm{Re}\right)\left((\overline{u}_{i,j}+\overline{u}_{j,i})-\frac{2}{3}\overline{u}_{k,k}\delta_{ij}\right) \tag{5.44}$$

$$\overline{q}_i=\frac{\mu(\overline{T})}{\gamma-1}\frac{1}{\mathrm{Pr}}\frac{1}{\mathrm{Re}}\overline{T}_{,i} \tag{5.45}$$

In these equations, the damping term is already present in the momentum equation. However, it is a bit more complicated as there is additional unsteady term in the momentum equation.

5.3.3 Conservative Form of Filtered Governing Equation

Filtered compressible Navier-Stokes equations in conservative non-dimensional form, assuming no source term, are as given below. The Favre filter is used here. For the sake of simplicity the superscripts showing the non-dimensional values are omitted.

$$\frac{\partial\overline{W}}{\partial t}+\frac{\partial}{\partial x_j}\left({}^{c}\overline{F}_j+{}^{v}\overline{F}_j\right)=0 \tag{5.46}$$

$$\overline{W}=\begin{bmatrix}\overline{\rho}\\ \overline{\rho}\widetilde{u}_1\\ \overline{\rho}\widetilde{u}_2\\ \overline{\rho}\widetilde{u}_3\\ \overline{\rho}\widetilde{e}\end{bmatrix},\ {}^{c}\overline{F}_j=\begin{bmatrix}\overline{\rho}\widetilde{u}_j\\ \overline{\rho}\widetilde{u}_j\widetilde{u}_1+\overline{p}\delta_{j1}\\ \overline{\rho}\widetilde{u}_j\widetilde{u}_2+\overline{p}\delta_{j2}\\ \overline{\rho}\widetilde{u}_j\widetilde{u}_3+\overline{p}\delta_{j3}\\ \widetilde{u}_j(\overline{\rho}\widetilde{e}+\overline{p})\end{bmatrix},\ {}^{v}\overline{F}_j=\begin{bmatrix}0\\ -\left(\widetilde{\sigma}_{j1}+\widetilde{\tau}_{j1}\right)\\ -\left(\widetilde{\sigma}_{j2}+\widetilde{\tau}_{j2}\right)\\ -\left(\widetilde{\sigma}_{j3}+\widetilde{\tau}_{j3}\right)\\ -\widetilde{u}_k\left(\widetilde{\sigma}_{kj}+\widetilde{\tau}_{kj}\right)+\frac{\gamma}{\gamma-1}\left(\widetilde{q}_j+\widetilde{q}_j^{t}\right)\end{bmatrix} \tag{5.47}$$

It should be noted that Dynamic viscosity and thermal conductivity are supposed to be expressed as function of filtered temperature in the same fashion as they are in instantaneous field. The Prandtl number is assumed to be the same for both large-scale and small-scale heat transfer.

5.4 Explicit Sub-Grid Scale Models

The system of equations used in this study is system (II) using Favre averaging. The following terms which are of 'medium' importance need modeling,

$$C_1 = \partial_j\left(\bar{\rho}\left(\tilde{u}_i\tilde{u}_j - \overleftrightarrow{u_i u_j}\right)\right) \tag{5.48}$$

$$C_2 = \partial_i\left(\left(\gamma-1\right)/2\,\bar{\rho}\tau_{kk}\right) \tag{5.49}$$

$$\begin{aligned} D_1 &= \frac{\gamma}{\gamma-1}\partial_i\left(\bar{p}\tilde{u}_i - \overline{p u_i}\right) = \\ &= \frac{\gamma}{\gamma-1}\partial_i\left(\bar{\rho}\bar{T}\tilde{u}_i - \overline{\rho T u_i}\right) \end{aligned} \tag{5.50}$$

$$D_2 = \partial_i\left(1/2\,\bar{\rho}\tilde{u}_k\tilde{u}_k\tilde{u}_i - 1/2\,\overline{\rho u_k u_k u_i}\right) \tag{5.51}$$

The common modeling practice is to model the terms C_1, C_2, and D_1 only. Although the term has D_2 a medium to low value, due to the lack of a model in the literature, it is disregarded here, as in reference [47] by the same research group who investigated the order of magnitude analysis. So it is assumed that the convection of sub-grid kinetic energy by the sub-grid velocity is small.

Modeling these SGS terms is easier than RANS models for large-scale eddied due to the fact that the small-scale eddies in LES simulations are more or less isotropic. However, for compressible flow especially in supersonic and hypersonic limits, the turbulent heat flux D_1, turbulent diffusion D_2, and turbulent viscous dissipation D_4 become significant which makes SGS models far from satisfactory [43].

Turbulent stress can be decomposed into three parts, which is the basis of some SGS models, and gives insight into the nature of turbulent stress.

$$-\tau_{ij} = L_{ij} + C_{ij} + R_{ij} \tag{5.52}$$

Using the following identitiy,

$$\begin{aligned} \overleftrightarrow{u_i u_j} = \overleftrightarrow{\left(\widetilde{u}_i + u'_i\right)\left(\widetilde{u}_j + u'_j\right)} &= \overleftrightarrow{\widetilde{u}_i \widetilde{u}_j} + \overleftrightarrow{\widetilde{u}_i u'_j} + \overleftrightarrow{u'_i \widetilde{u}_j} + \overleftrightarrow{u'_i u'_j} \\ &= \widetilde{u}_i \widetilde{u}_j + \left(\overleftrightarrow{\widetilde{u}_i \widetilde{u}_j} - \widetilde{u}_i \widetilde{u}_j\right) + \left(\overleftrightarrow{\widetilde{u}_i u'_j} + \overleftrightarrow{u'_i \widetilde{u}_j}\right) + \left(\overleftrightarrow{u'_i u'_j}\right) \end{aligned} \tag{5.53}$$

The tensors L_{ij}, C_{ij}, and R_{ij} are called *Leonard-*, *Cross-*, and SGS *Reynolds-stresses* respectively, as given below,

$$L_{ij} = \overleftrightarrow{\widetilde{u}_i \widetilde{u}_j} - \widetilde{u}_i \widetilde{u}_j \tag{5.54}$$

$$C_{ij} = \overleftrightarrow{\widetilde{u}_i u'_j} + \overleftrightarrow{u'_i \widetilde{u}_j} \tag{5.55}$$

$$R_{ij} = \overleftrightarrow{u'_i u'_j} \tag{5.56}$$

Leonard stresses represent the interaction between resolved scales which transfer the energy to the small scales. This phenomenon is known as *out-scatter*. Cross stresses characterize the interaction between resolved and unresolved scales which transfer energy to either large or small scales. The sub-grid Reynolds stresses illustrate the interaction between small scales which produce and transfer energy and from small scales to large scales. This phenomenon is knows as *back-scatter*.

Using a scale similarity model [48], the cross stress tensor can be written in terms of resolved scales,

$$C_{ij} = \overleftrightarrow{\widetilde{u}_i u'_j} + \overleftrightarrow{u'_i \widetilde{u}_j} = \widetilde{u}_i \widetilde{u}_j - \widetilde{\widetilde{u}}_i \widetilde{\widetilde{u}}_j \tag{5.57}$$

Together with the Leonard stress, they can be written as,

$$K_{ij}=L_{ij}+C_{ij}=\overleftrightarrow{\widetilde{u}_i\widetilde{u}_j}-\widetilde{\widetilde{u}}_i\widetilde{\widetilde{u}}_j \tag{5.58}$$

This can be calculated using resolved field. Hence, the only term which needs modeling is the sub-grid Reynolds stress term.

SGS terms can be modeled explicitly, such as eddy viscosity models, scale similarity models, and mixed models, or they can be modeled implicitly using the artificial diffusion of the numerical scheme.

5.4.1 Smagorinsky Model

Eddy viscosity models take into account the global effect of SGS terms disregarding the local convection or diffusion of energy, such as Smagorinsky's model [49] in which the deviatoric part of the SGS turbulent stress is given by,

$$\tau_{kl}-\frac{1}{3}\tau_{mm}\delta_{kl}=2\overline{\rho}(C_S\Delta)^2\left|\widetilde{S}\right|\left(\widetilde{S}_{kl}-\frac{1}{3}\widetilde{S}_{mm}\delta_{kl}\right) \tag{5.59}$$

with eddy viscosity,

$$\mu_t=\overline{\rho}(C_s\Delta)^2|S| \tag{5.60}$$

where the Favre averaged strain tensor is $\widetilde{S}_{ij}=1/2\left(\widetilde{u}_{i,j}+\widetilde{u}_{j,i}\right)$, and characteristic rate of strain tensor is given by $\left|\widetilde{S}\right|=\sqrt{2S_{ij}S_{ij}}$. $\overline{\Delta}$ is the filter length. Also a model for the isotropic part of the SGS stress is given by Yoshizawa [50] as,

$$\tau_{kk}=2\overline{\rho}(C_I\Delta)^2\left|\widetilde{S}\right|^2 \tag{5.61}$$

The constant C_I used for isotropic SGS modeling is assumed to be the same as the Smagorinsky constant C_S used for modeling deviatoric part of the SGS tensor. This model results in the following relations,

$$C_1' = \bar{\rho}\left(\tilde{u}_i\tilde{u}_j - \overleftrightarrow{u_i u_j}\right) = \bar{\rho}\upsilon_t \bar{S}_{ij} \tag{5.62}$$

$$C_2' = (\gamma - 1)/2\,\bar{\rho}\tau_{kk} = (\gamma - 1)\left(C_I \bar{\rho}\Delta\left|\tilde{S}\right|\right)^2 \tag{5.63}$$

$$D_1' = \frac{\gamma}{\gamma - 1}\left(\bar{\rho}\bar{T}\tilde{u}_i - \overline{\rho T u_i}\right) = \frac{\gamma}{\gamma - 1}\left(\bar{\rho}\frac{\upsilon_t}{\mathrm{Pr}_t}\frac{\partial \bar{T}}{\partial x_i}\right) \tag{5.64}$$

Numerous values for the Smagorinsky constant C_s is proposed in the literature, Deardorff [51] has proposed the value of $C_s = 0.1$ in the case of channel flow and $C_s = 0.2$ in the case of the homogeneous isotropic turbulence. McMillan and Ferziger [52] obtained an intermediate value $C_s = 0.13$ which matches the sub-grid scale tensor with the corresponding exact value calculated by direct simulation. Based on the spectrum of the energy, Schumann [53] suggested the following relationship for Smagorinsky constant,

$$C_s = \frac{1}{\pi}\left(\frac{3C_K}{2}\right)^{-3/4} \tag{5.65}$$

where $C_K = 1.4$ is the Kolmogorov constant. This expression is based on the hypothesis that the dissipation of sub-grid kinetic energy is identical to the flux of kinetic energy in the energy cascade between resolved and unresolved scales when the sub-grid scale is located in the Kolmogorov cascade, i.e. in the $k^{-5/3}$ zone. This choice leads to the value of $C_s = 0.18$. This constant, however, is not universal. Smagorinsky model is known to be too much dissipative in the laminar region and the correlation between the exact sub-grid scale tensor and the model is often poor. In practice, it is often customary to keep the lower value for the constant, for example Moin and Kim [54] proposed $C_s = 0.065$ for channel flow or Erlebacher et al. [55] recommended $C_s = 0.092$ for compressible flow. Herein, the value $C_s = 0.1$ has been used.

It is assumed that the filter width is the third root of the volume of the cell around the node under consideration, i.e. $\overline{\Delta} = vol(C(I))^{1/3}$. This approach to specify the filter is the implicit filtering which suits the unstructured meshing. Presence of a solid wall modifies the dynamics of the turbulence in different aspects; in particular it suppresses the growth of the small scales and the preceding expression of the filter cut length overestimates the characteristic mixing length of the sub-grid modes. Therefore it is essential to damp the characteristic length of the sub-grid scale given by the Smagorinsky model. This decreases the intensity of the sub-grid scale viscosity by introducing a damping factor which is a function of distance from the wall. Hence the filter cut length is written as follows,

$$\Delta = f\Delta_{iso} \tag{5.66}$$

The function proposed by Van Driest [56] is a very common approach and is given as,

$$f(y^+) = \left(1 - e^{-\frac{y^+}{A^+}}\right)^2 \quad , \quad A^+ = 25 \tag{5.67}$$

The dimensionless normal distance to the wall y^+ is defined in appendix A. It should be noted that for the parallel computation, y^+, has been found globally on the account that the closest wall face to a certain point can be located in another sub-domain, especially for nodes close to sub-domain boundaries.

5.4.2 Performance of Sub-grid Scale Models

Vreman et al. [45] using a priori LES test, investigated the quality of SGS modeling. Two measures have been carried out to study the effectiveness of the models. First, *norm* of the modeled turbulent stress is compared with that of exact turbulent stress to show whether *average value of turbulent stress* is calculated well. Second, *correlation* of the modeled turbulent stress with that of exact turbulent stress is calculated to explore the quality of the *spatial structure* of the modeled turbulent stress. The study is performed for the turbulent stresses $\|\bar{\rho}\tau_{1j}\|$, $\|\bar{\rho}\tau_{2j}\|$, and $\|\bar{\rho}\tau_{3j}\|$ in case of filtered DNS results and Smagorinsky, Bardina, and Clerk models.

Smagorinsky model is founded to be too much dissipative in the transitional regime due to the presence of mean shear, but beyond that as the flow is more developed, the sub-grid terms are reasonably predicted for $C_S = 0.17$. However, the poor correlation coefficient of this model shows that the spatial structure of turbulence is not modeled satisfactorily at all.

Bardina, and Clerk models are shown to perform excellent both in terms of magnitude and correlation coefficient of higher than 0.95. However, in cases such as 2D mixing layer, these models are reported to lead to numerical instability. This instability can be interpreted as negative eddy-viscosity.

Vreman et al. [45] also studied norms of τ_{12}, L_{12}, C_{12}, and R_{12}. It is showed that R_{12} has the least important contribution. This is due to the fact that large-scale structures of the mixing layer DNS database mainly contribute to L_{12} and C_{12} when they are filtered. This fact also explains the poor correlation of Smagorinsky model since this model has been developed for flows in which term R_{12} is significant.

5.4.3 Consistency between Sub-grid Scale Models and Filters

Piomelli et al. [57], performed a priori test using DNS of an incompressible channel flow using Gaussian and cut-off Filter as well as Smagorinsky and Bardina's mixed model. Filter can be defined as a weighted average of the quantity over a volume as,

$$\bar{u}_i(\vec{x}) = \int_D G(\vec{x},\vec{x}',\Delta)u_i(\vec{x}')d\vec{x}' \tag{5.68}$$

$u_i' = u_i - \bar{u}_i$ will depend both on the grid size and on the type of filter. The Gaussian and cutt-off filters are defined as follows,

$$G_i(x_i, x_i', \Delta_i) = \frac{2Sin(\pi(x_i - x_i')/\Delta_i)}{\pi(x_i - x_i')} \quad , \quad i = 1..3 \text{ Sharp Fourier cut-off filter} \tag{5.69}$$

$$G_i(x_i, x_i', \Delta_i) = (6/\pi\Delta_i)^{1/2} \exp\left[-6(x_i - x_i')^2/\Delta_i^{\,2}\right] \quad , \quad i = 1..3 \quad \text{Gaussian filter} \tag{5.70}$$

When Gaussian filter is used, sub-grid scale account for a considerable fraction, about 10%, of total turbulent kinetic energy. When Cut-off filter is used, contribution of sub-grid scale is entirely due to high wave numbers and account for a very small fraction, about 1%, of total turbulent kinetic energy.

The Bardina's mixed SGS model is defined as below,

$$\tau_{ij}{}^{BM} = C_{BM}\left(\overline{\widetilde{\overline{u}}}_i\overline{\widetilde{\overline{u}}}_j - \overline{\widetilde{\overline{u}}_i\widetilde{\overline{u}}_j}\right) - 2\mu_t\bar{S}_{ij} \tag{5.71}$$

l_S is a length scale which represents small eddies and it is related grid and filter size. Smagorinsky model by itself assures Galilean invariance, but in mixed model C_{BM} must be equal to unity for the equation of motion to be invariant under transformation between inertial frames of reference.

Piomelli et al. [57] found that the behavior of sub-grid scale Reynolds stress strongly depend on the filter chosen. The consistency requirement between the model and the filter is satisfied if they both carry the same information.

Applying cut-off filter, the sub-grid scale field contains the contribution of any structure with wave number $|k_i| > (\pi/\Delta_i)$. The Gaussian filter application, however, results in wider range of scales contributing to the sub-grid scale model.

Smagorinsky model is adequate when the sub-grid scales are well defined. It contains information only about one length scale and can not be coupled with Gaussian filter in which wider range of structures contribute to sub-grid stress. However, this model suits the cut-off filter characteristic which defines the maximum length scale of sub-grid structures more precisely. This choice is called $C-S$ model. However, when the cut-off filter is applied, the scale similar part of the mixed model is identically zero and mixed and Smagorinsky models are identical.

Mixed or scale-similar models are based on the assumption that principal interaction between resolved and unresolved eddies take place between the smallest resolved and the largest unresolved eddies. These models are best used with Gaussian filter which allows for interaction of wider range of scales close to the filter width. This choice is called $G-M$ coupling. In comparison, $G-M$ combination predicts energy spectrum better than $C-S$ combination on account of high dissipative characteristic Smagorinsky model.

5.4.4 Dynamic SGS Turbulent Shear Stress – Incompressible Flow

It is known that eddy-viscosity SGS models fail to represent correctly different turbulent flows with a *single universal constant*, especially in rotating or shear flows, near solid walls, and in transitional regime [58]. M. Germano et al. [58] based on a LES priori test using a cut-off filter, presented an eddy-viscosity model in which the model coefficient is computed dynamically based on the algebraic identity between resolved SGS turbulent stresses at two different filtered levels. The proposed model has the advantages that it vanishes in the laminar regions of the flow and also it has the correct asymptotic behavior in the near-wall region of turbulent boundary layer without requiring damping or intermittency functions. The model is also capable of taking into account the backscatter. This model locally calculates the eddy viscosity coefficient by using the smallest resolved scales to model SGS turbulent stresses. In this model two filters are defined as the convolution of the variables with two filter functions: *grid filter* $\overline{G}$ and *test filter* $\hat{G}$, as follows,

$$\bar{f}(\vec{x}) = \int f(\vec{x}')\overline{G}(\vec{x},\vec{x}')d\vec{x}' \qquad (5.72)$$

$$\hat{f}(\vec{x}) = \int f(\vec{x}')\hat{G}(\vec{x},\vec{x}')d\vec{x}' \qquad (5.73)$$

Test filter is assumed to have a larger width $\hat{\overline{\Delta}}$ than that of grid filter $\overline{\Delta}$ and corresponds to a coarser mesh. It is also assumed that $\hat{\overline{G}} = \hat{G}\overline{G}$. Applying the filters $\overline{G}$ and $\hat{\overline{G}}$ to the governing equations results in sub-grid stresses at each filtering level which are given below respectively. The grid filter is shown by $\bar{\bullet}$ or $\overleftrightarrow{\bullet\bullet\bullet}$ and the test filter is shown by $\hat{\bullet}$ or $\widehat{\bullet\bullet\bullet}$.

$$\tau_{ij} = \overline{u}_i\overline{u}_j - \overleftrightarrow{u_i u_j} \tag{5.74}$$

$$T_{ij} = \widehat{\overline{u}}_i\widehat{\overline{u}}_j - \widehat{\overleftrightarrow{u_i u_j}} \tag{5.75}$$

The contribution to Reynolds stresses by scales whose length is between grid and test filter is given by,

$$\left(T_{ij} - \widehat{\tau}_{ij}\right) \equiv L_{ij} = \widehat{\widetilde{u}}_i\widehat{\widetilde{u}}_j - \widehat{\overline{u}_i\overline{u}_j} \tag{5.76}$$

This is the resolved turbulent stress which can be calculated explicitly. This identity is used to derive more appropriate value for Smagorinsky coefficient with regard to the instantaneous state of the flow. It is assumed that the same relation, such as Smagorinsky model, can parametrize both τ_{ij} and T_{ij}. The anisotropic parts of these two SGS stress tensor is given by,

$$\tau_{ij} - \left(\delta_{ij}/3\right)\tau_{kk} = m_{ij} = 2\left(C_S\overline{\Delta}\right)^2\left|\overline{S}\right|\overline{S}_{ij} \quad \text{Where } \left|\overline{S}\right| = \sqrt{2\overline{S}_{mn}\overline{S}_{mn}} \text{ and } \overline{S} = \left(\partial_j\widetilde{u}_i + \partial_i\widetilde{u}_j\right)/2 \tag{5.77}$$

$$T_{ij} - \left(\delta_{ij}/3\right)T_{kk} = M_{ij} = 2\left(C_S\widehat{\overline{\Delta}}\right)^2\left|\widehat{\overline{S}}\right|\widehat{\overline{S}}_{ij} \quad \text{Where } \left|\widehat{\overline{S}}\right| = \sqrt{2\widehat{\overline{S}}_{mn}\widehat{\overline{S}}_{mn}} \text{ and } \widehat{\overline{S}} = \left(\partial_j\widehat{\widetilde{u}}_i + \partial_i\widehat{\widetilde{u}}_j\right)/2 \tag{5.78}$$

Plugging the above Smagorinsky model in the preceding identity for L_{ij} gives the following,

$$L_{ij}\overline{S}_{ij} = 2C_S{}^2\left(\widehat{\Delta}^2\left|\widehat{\overline{S}}\right|\widehat{\overline{S}}_{ij}\overline{S}_{ij} - \widehat{\overline{\Delta}}^2\left|\widehat{\overline{S}}\right|\widehat{\overline{S}}_{ij}\overline{S}_{ij}\right) \tag{5.79}$$

The above relation can be used to evaluate the Samgorinsky coefficient C_S dynamically. On account of ill-conditioning possibility for C_S that happens when the value of the parentheses on the right hand side becomes zero, M. Germano et al. [58] took an average over the plane normal to the channel wall, denoted by $\langle \bullet \rangle$, to compute C_S as given below,

$$C_S{}^2 = \frac{1}{2} \frac{L_{kl}\overline{S}_{kl}}{\widehat{\Delta}^2 \left\langle \left|\widehat{\overline{S}}\right| \widehat{\overline{S}}_{pq} \overline{S}_{pq} \right\rangle - \widehat{\overline{\Delta}}^2 \left\langle \left|\widehat{\overline{S}}\right| \widehat{\overline{S}}_{mn} \overline{S}_{mn} \right\rangle} \tag{5.80}$$

Hence, the dynamic eddy-viscosity is given by,

$$m_{ij} = \frac{L_{kl}\overline{S}_{kl}}{\left(\widehat{\overline{\Delta}}/\overline{\Delta}\right)^2 \left\langle \left|\widehat{\overline{S}}\right| \widehat{\overline{S}}_{mn} \overline{S}_{mn} \right\rangle - \left\langle \left|\widehat{\overline{S}}\right| \widehat{\overline{S}}_{pq} \overline{S}_{pq} \right\rangle} \left|\overline{S}\right| \overline{S}_{ij} \tag{5.81}$$

This model has remarkable properties such as, zero SGS stress in laminar regions of flow or at solid wall due to the fact that L_{ij} vanishes in such conditions. Also in the near wall region, m_{ij} is proportional to the cube of distance from wall which is the correct asymptotic behavior without requiring any ad hoc damping functions. In addition, the model does not exclude backscatter. This can be seen from the fact that the modeled SGS dissipation $\varepsilon_{SGS} = m_{ij}\overline{S}_{ij}$, is proportional to average dissipation of the resolved turbulent stresses $\left\langle L_{ij}\overline{S}_{ij} \right\rangle$, which can be either positive or negative.

The only parameter to adjust in the model is $(\widehat{\overline{\Delta}}/\overline{\Delta})$. Small values of this ratio can be infected by numerical errors while large values bring larger structures into account in SGS turbulent stress calculation. The optimum value, however, varies depending on the flow. M. Germano et al. [58] found that for the ratio $(\widehat{\overline{\Delta}}/\overline{\Delta}) = 2$, the mean SGS shear stress τ_{12} and dissipation ε_{SGS} matches the exact values very well, and for larger values results were not shown to be very sensitive. In transition regime, however, the results were not satisfactory. The discrepancy is owing to the fact that small difference in prediction of the onset of transition leads to significant difference in the instantaneous field that is simulated after. Eventually, the effect of ratio $(\hat{\bar{\Delta}}/\bar{\Delta})$ should be further investigated for more complex geometries, different filters such as box filter, and local or time averages instead of their plane average.

5.4.5 Dynamic SGS Turbulent Shear Stress – Compressible Flow

Moin et al. [59] further extended the dynamic SGS modeling for compressible turbulent flows by sharp cut-off filtering of the DNS data of isotropic turbulence, homogeneous shear flow, and turbulent channel flow. They found excellent results for isotropic turbulence decay simulation. They also found an expression for SGS turbulent Prandtl number as a function of molecular Prandtl number, direction of the scalar gradient, and distance from the wall. This dynamic model, using the scale similarity idea, utilizes the spectral information available in large scale field.

They also used another methodology for filtering the governing equations resulting in the term $D_2 = \bar{\rho}\left(\overleftrightarrow{T\partial_k u_k} - \tilde{T}\partial_k \tilde{u}_k\right)$ and then it was neglected based on a priori test which showed the term is only 5% of the SGS heat flux. The SGS turbulent shear stress is turned out to be,

$$\tau_{ij} = \bar{\rho}\tilde{u}_i\tilde{u}_j - \overleftrightarrow{\overline{\rho u_i u_j}} \tag{5.82}$$

Applying the test filter $\hat{G}$ to the resolved field, the test filtered stresses are,

$$T_{ij} = (\widehat{\overline{\rho u_i}}\,\widehat{\overline{\rho u_j}} / \hat{\bar{\rho}}) - \widehat{\overline{\rho u_i u_j}} \tag{5.83}$$

Using the Germano's identity, the Leonard stresses are given by,

$$\left(T_{ij} - \hat{\tau}_{ij}\right) \equiv L_{ij} = (\widehat{\bar{\rho}\tilde{u}_i}\,\widehat{\bar{\rho}\tilde{u}_j} / \hat{\bar{\rho}}) - \widehat{\bar{\rho}\tilde{u}_i\tilde{u}_j} \tag{5.84}$$

The right hand side of the above relation is computable solely from the resolved field. Using the eddy-viscosity model at both filtering levels, the isotrpic SGS turbulent stresses are given by,

$$\tau_{kk} = 2\bar{\rho}(C_I\Delta)^2\left|\tilde{S}\right|^2 \tag{5.85}$$

$$T_{kk} = 2\bar{\rho}(C_I\Delta)^2\left|\hat{\tilde{S}}\right|^2 \tag{5.86}$$

assuming the same eddy-viscosity model with the same constant is applicable at two filtered level. The coefficient C_I can be computed as,

$$T_{kk} - \hat{\tau}_{kk} \equiv \widehat{\bar{\rho}\tilde{u}_k\tilde{u}_k} - (\widehat{\bar{\rho}\tilde{u}_k}\,\widehat{\bar{\rho}\tilde{u}_k} / \hat{\bar{\rho}}) = 2C_I{}^2(\hat{\bar{\rho}}\hat{\Delta}^2\left|\hat{\tilde{S}}\right|^2 - \Delta^2\widehat{\bar{\rho}\left|\tilde{S}\right|^2}) \tag{5.87}$$

As shown in priori test of Germano et al. [58] the terms similar to the right hand side of the above equation can become zero at some points. Hence, the well-conditioned formulation for C_I is obtained by an averaging procedure. Moin et al. [59] assumed that in their temporally developing homogeneous flow, C_I is only a function of time. They performed a volume averaging denoted by $\langle \bullet \rangle$, that leads to,

$$C_I{}^2 = \frac{\left\langle \widehat{\bar{\rho}\tilde{u}_k\tilde{u}_k} - (\widehat{\bar{\rho}\tilde{u}_k}\,\widehat{\bar{\rho}\tilde{u}_k} / \hat{\bar{\rho}}) \right\rangle}{2\left\langle \hat{\bar{\rho}}\hat{\Delta}^2\left|\hat{\tilde{S}}\right|^2 - \Delta^2\widehat{\bar{\rho}\left|\tilde{S}\right|^2} \right\rangle} \tag{5.88}$$

However, in more complex flows, more localized averaging should be done in space and time. The model for τ_{kk} then will be written as,

$$\tau_{kk} = \frac{\left\langle \overbrace{\overline{\rho}\widetilde{u}_k\widetilde{u}_k} - (\overbrace{\overline{\rho}\widetilde{u}_k}\,\overbrace{\overline{\rho}\widetilde{u}_k} / \widehat{\overline{\rho}}) \right\rangle}{\left\langle \widehat{\overline{\rho}}\left(\widehat{\Delta}/\Delta\right)^2 \left|\widehat{\widetilde{S}}\right|^2 - \overbrace{\overline{\rho}\left|\widetilde{S}\right|^2} \right\rangle} \overline{\rho}\left|\widetilde{S}\right|^2 \tag{5.89}$$

Using the Smagorinsky model at both filtering levels, the deviatoric SGS turbulent stresses are given by,

$$\tau_{ij} - \frac{1}{3}\tau_{mm}\delta_{ij} = 2\overline{\rho}(C_S\Delta)^2\left|\widetilde{S}\right|\left(\widetilde{S}_{ij} - \frac{1}{3}\widetilde{S}_{mm}\delta_{ij}\right) \tag{5.90}$$

$$T_{ij} - \frac{1}{3}T_{mm}\delta_{ij} = 2\widehat{\overline{\rho}}(C_S\widehat{\Delta})^2\left|\widehat{\widetilde{S}}\right|\left(\widehat{\widetilde{S}}_{ij} - \frac{1}{3}\widehat{\widetilde{S}}_{mm}\delta_{ij}\right) \tag{5.91}$$

Again it is assumed that the same eddy-viscosity model with the same constant is applicable at two filtered level. Then,

$$L_{ij} = T_{ij} - \widehat{\tau}_{ij} \equiv 2C_S{}^2\widehat{\overline{\rho}}\widehat{\Delta}^2\left|\widehat{\widetilde{S}}\right|\left(\widehat{\widetilde{S}}_{ij} - \frac{1}{3}\widehat{\widetilde{S}}_{mm}\delta_{ij}\right) - \frac{1}{3}T_{mm}\delta_{ij} - 2C_S{}^2\,\overbrace{\overline{\rho}\Delta^2\left|\widetilde{S}\right|\left(\widetilde{S}_{ij} - \frac{1}{3}\widetilde{S}_{mm}\delta_{ij}\right)} + \frac{1}{3}\widehat{\tau}_{mm}\delta_{ij} \tag{5.92}$$

Using the previous relation for $T_{kk} - \widehat{\tau}_{kk} \equiv \overbrace{\overline{\rho}\widetilde{u}_k\widetilde{u}_k} - (\overbrace{\overline{\rho}\widetilde{u}_k}\,\overbrace{\overline{\rho}\widetilde{u}_k} / \widehat{\overline{\rho}})$, multiplying both sides by $\widetilde{S}_{kl}$, using the identity $\widetilde{S}_{kl}\delta_{kl} = \widetilde{S}_{jj}$, and performing appropriate volume averaging, the coefficient C_S is given as below,

$$C_S{}^2 = \frac{\left\langle [\overbrace{\overline{\rho}\widetilde{u}_k\widetilde{u}_l} - (\overbrace{\overline{\rho}\widetilde{u}_k}\,\overbrace{\overline{\rho}\widetilde{u}_l} / \widehat{\overline{\rho}})]\widetilde{S}_{kl} - 1/3(T_{mm} - \widehat{\tau}_{mm})\widetilde{S}_{jj} \right\rangle}{2\left\langle -\widehat{\overline{\rho}}\widehat{\Delta}^2\left|\widehat{\widetilde{S}}\right|\left(\widehat{\widetilde{S}}_{kl}\widetilde{S}_{kl} - \frac{1}{3}\widehat{\widetilde{S}}_{mm}\widetilde{S}_{jj}\right) + \Delta^2(\overbrace{\overline{\rho}\left|\widetilde{S}\right|\widetilde{S}_{kl}}\,\widetilde{S}_{kl} - 1/3\,\overbrace{\overline{\rho}\left|\widetilde{S}\right|\widetilde{S}_{mm}}\,\widetilde{S}_{jj}) \right\rangle} \tag{5.93}$$

Again the only adjustable parameter is $(\hat{\bar{\Delta}}/\bar{\Delta})$. A different formula for C_S will be obtained if it was contracted with another tensor than $\tilde{S}_{kl}$. However, LES results are expected not to be sensitive to this factor as it appears both in numerator and denominator of the above fraction. Moin et al. [59] found that two different contracting tensor might have at most 10% discrepancy in some turbulent statistics. They found the value of C_S to be roughly between $0.008-0.014$ and value of C_I to be roughly between $0.0025-0.009$. They also found these values are relatively little influenced by initial temperature spectrum.

5.4.6 Dynamic Turbulent Heat Flux – Compressible Flow

As seen before, the SGS heat flux is given as a function of filtered variables,

$$\begin{aligned} q_k &= \bar{\rho}\left(\overleftrightarrow{u_k T} - \tilde{u}_k \tilde{T}\right) \\ &= \overline{\rho u_k T} - \left(\overline{\rho u_k}\,\overline{\rho T}/\bar{\rho}\right) \end{aligned} \tag{5.94}$$

Where the eddy-diffusivity model for SGS heat flux is given by,

$$q_k = -\frac{\bar{\rho}\upsilon_T}{\mathrm{Pr}_T}\frac{\partial \tilde{T}}{\partial x_k} \tag{5.95}$$

Where eddy viscosity is $\upsilon_T = C_S \Delta^2 \left|\tilde{S}\right|$. The SGS turbulent Prantdl number Pr_T is to be found dynamically. The heat flux at the test filter level is given by,

$$Q_k = \overbrace{\overline{\rho u_k T}} - (\overbrace{\overline{\rho u_k}}\,\overbrace{\overline{\rho T}} / \hat{\bar{\rho}}) \tag{5.96}$$

The eddy-diffusivity at this level is given by,

$$Q_k = -\frac{\hat{\bar{\rho}}\hat{\upsilon}_T}{\mathrm{Pr}_T}\frac{\partial \hat{\tilde{T}}}{\partial x_k} = -\frac{\hat{\bar{\rho}} C \hat{\Delta}^2 \left|\hat{\tilde{S}}\right|}{\mathrm{Pr}_T}\frac{\partial \hat{\tilde{T}}}{\partial x_k} \tag{5.97}$$

Using the idea of Germano's identity, the difference of heat fluxes at different filtering level can be written as,

$$\begin{aligned} K_k \equiv Q_k - \widehat{q}_k &= \widehat{(\overline{\rho u_k}\,\overline{\rho T}/\overline{\rho})} - (\widehat{\overline{\rho u_k}}\,\widehat{\overline{\rho T}}/\widehat{\overline{\rho}}) \\ &= (\widehat{\overline{\rho}\widetilde{u}_k\widetilde{T}}) - (\widehat{\overline{\rho}\widetilde{u}_k}\,\widehat{\overline{\rho}\widetilde{T}}/\widehat{\overline{\rho}}) \end{aligned} \tag{5.98}$$

The above relation is directly computable. Substituting the eddy-viscosity models into the above relation leads to,

$$-\frac{2C_S{}^2}{\mathrm{Pr}_t}(\widehat{\overline{\rho}}\widehat{\Delta}^2\left|\widehat{\widetilde{S}}\right|\frac{\partial\widehat{\widetilde{T}}}{\partial x_k} - \widehat{\overline{\rho}\Delta^2\left|\widetilde{S}\right|\frac{\partial\widetilde{T}}{\partial x_k}}) = (\widehat{\overline{\rho}\widetilde{u}_k\widetilde{T}}) - (\widehat{\overline{\rho}\widetilde{u}_k}\,\widehat{\overline{\rho}\widetilde{T}}/\widehat{\overline{\rho}}) \tag{5.99}$$

Contracting with $\partial\widetilde{T}/\partial x_k$ and performing appropriate spatial averaging leads to,

$$\mathrm{Pr}_t = C_S{}^2\frac{\left\langle (\widehat{\overline{\rho}\Delta^2\left|\widetilde{S}\right|\frac{\partial\widetilde{T}}{\partial x_k}}\frac{\partial\widetilde{T}}{\partial x_k} - \widehat{\overline{\rho}}\widehat{\Delta}^2\left|\widehat{\widetilde{S}}\right|\frac{\partial\widehat{\widetilde{T}}}{\partial x_k}\frac{\partial\widetilde{T}}{\partial x_k}) \right\rangle}{2\left\langle ((\widehat{\overline{\rho}\widetilde{u}_k\widetilde{T}}) - (\widehat{\overline{\rho}\widetilde{u}_k}\,\widehat{\overline{\rho}\widetilde{T}}/\widehat{\overline{\rho}}))\frac{\partial\widetilde{T}}{\partial x_k} \right\rangle} \tag{5.100}$$

Moin et al. [59] used the value of $(\widehat{\overline{\Delta}}/\overline{\Delta}) = 2$ but they demonstrated that in compressible LES the results are insensitive to this parameter when it exceeds 2. The same thing was accredited by Germano et al. [58] in case of incompressible flows. Moin et al. [59] found that Pr_t is approximately 0.85. Higher value of Pr_t not only attributes to compressibility effects but also shows the different initial temperature and velocity spectra. It is also been seen that Pr_t varies with time, and in case of channel flow, it also varies with distance from wall. Eventually, the study revealed that LES with constant model coefficient accumulate more energy at high wave numbers. This shows the need to dynamically compute these coefficients to adjust to flow conditions.

Priori tests have shown that dynamic LES accurately predicts isotropic turbulence decay as well as transitional and turbulent channel flow. However, their performance it is limited for extrapolating the actual LES calculations.

5.4.7 Cure for Dynamic SGS Models Singularity

Lilly [60] proposed a modification to the dynamic SGS modeling of Germano et al. [58] and Moin et al. [59] for their stress-strain relationship at two different filtered level to become optimal using a least square approach. This modification also removed the singularity in the model which necessitated spatial averaging. Considering the following eddy-viscosity model for Leonard stresses,

$$L_{ij}-\frac{1}{3}L_{kk}\delta_{ij}=2{C_S}^2M_{ij} \tag{5.101}$$

Where,

$$M_{ij}=\widehat{\bar{\rho}}\widehat{\Delta}^2\left|\widehat{\tilde{S}}\right|\left(\widehat{\tilde{S}}_{kl}-\frac{1}{3}\widehat{\tilde{S}}_{mm}\delta_{kl}\right)-\overbrace{\bar{\rho}\Delta^2\left|\tilde{S}\right|\left(\tilde{S}_{kl}-\frac{1}{3}\tilde{S}_{mm}\delta_{kl}\right)} \tag{5.102}$$

It represents five independent equations in one unknown C_S. As no value of C_S can simultaneously make all five equations correct, by applying a least square methods, the error of the above relation can be minimized. To this aim, square of error is defined as,

$$Q=\left(L_{ij}-\frac{1}{3}L_{kk}\delta_{ij}+2{C_S}^2M_{ij}\right)^2 \tag{5.103}$$

Since $\partial^2 Q/\partial\left(C_S{}^2\right)^2 > 0$, setting $\partial Q/\partial\left(C_S{}^2\right) = 0$ will give the $C_S{}^2$ that makes Q minimum as,

$$C_S{}^2 = \frac{1}{2}\left(\frac{L_{ij}M_{ij}}{M_{ij}{}^2}\right) \tag{5.104}$$

The relation in references [58] and [59] is $C_S{}^2 = 1/2\left(L_{ij}\bar{S}_{ij}/M_{ij}\bar{S}_{ij}\right)$. This choice is just one of the many possible projections of the Leonard stress relation. Germano et al. [58] and Moin et al. [59] also found that denominator of their relation might vanish leading to numerical instability. Hence, they averaged the numerator and denominator and this has lessened some advantages of their model. However, here C becomes infinite only if all five independent components of M_{ij} vanishes. Also it is less presumable but excessive values of C can be removed by an averaging or simply by truncating isolated large values.

The same approach is taken for SGS heat flux. By analogy to Leonard stresses they can be written as,

$$K_i \equiv Q_i - \hat{q}_i = \frac{2C_S{}^2}{\mathrm{Pr}_T} R_i \tag{5.105}$$

where,

$$R_i = (\widehat{\bar{\rho}\Delta^2\left|\tilde{S}\right|\frac{\partial\tilde{T}}{\partial x_i}} - \hat{\bar{\rho}}\hat{\Delta}^2\left|\hat{\tilde{S}}\right|\frac{\partial\hat{\tilde{T}}}{\partial x_i}) \tag{5.106}$$

The same least square procedure results in the following,

$$\frac{1}{\mathrm{Pr}_t} = \frac{1}{2C_S{}^2}\frac{K_i R_i}{R_i^2} = \frac{M_{ij}{}^2}{L_{ij}M_{ij}}\frac{K_i R_i}{R_i^2} \tag{5.107}$$

5.5 Implicit Sub-Grid Scale Models

The numerical solution of the LES governing equations has several numerical errors. The most important numerical error is the spatial truncation error and depends on the grid spacing h [42]. The new governing equations, that are actually solved in the CFD simulation, are given below for an incompressible flow,

$$\frac{\overline{D}\overline{U}_j}{\overline{D}t} = \nu \frac{\partial^2 \overline{U}_j}{\partial x_i \partial x_i} - \frac{\partial}{\partial x_i}\left(\tau_{ij} + \tau_{ij}^h\right) - \frac{1}{\rho}\frac{\partial \overline{p}}{\partial x_j} \tag{5.108}$$

in which τ_{ij}^h is the numerical stress which is of the order h^n with n being the order accuracy of the numerical method. Hence, τ_{ij}^h depends on the numerical method used to solve the governing equations. Using the SGS models discussed in the previous sections, the ideal numerical model should produce a negligible τ_{ij}^h compared to τ_{ij}^{SGS}.

As initiated by Boris et al. [61], in implicit LES (ILES) approach, the "monotone" numerical methods are used to solve the Navier-Stokes equations without using the explicit residual stress model. The monotone methods lead to significant numerical stress τ_{ij}^h which replaces the SGS model. Boris et al. [61] called this method MILES which stands for Monotone Integrated Large Eddy Simulation.

In ILES approach, artificial diffusion of the numerical scheme, in the form of the truncation error terms, is solely responsible to model the effect of the unresolved scales on the resolved scales in the energy cascade and damp the turbulent kinetic energy. No SGS diffusion model is used while the mesh is highly resolved. Hence, in the implicit LES the modeling issue lies in the treatment of the convective term. The convective flux, as discussed in previous chapters, is computed here using the $\kappa - \alpha$ type method of Van Leer based on the second order Roe method which is modified by introducing a factor α

that allows for balancing the importance of the centered scheme and the artificial viscosity in the scheme. Flux calculation at the interface of cells I and J becomes,

$$F_{IJ} = \frac{1}{2}\left[{}^{c}F(W_{IJ}) + {}^{c}F(W_{JI})\right] - \alpha\,\partial^{c}F_{IJ} \tag{5.109}$$

where W is the variable vector. When $\alpha = 1/2$, this scheme is the same as the second order Roe method. To construct the interface variables a MUSCL type expression is used by introducing a combination of a centered and an upwind gradients to evaluate ∇W_{IJ} and ∇W_{JI},

$$W_{IJ} = W_I + \frac{1}{2}\left[(1-\kappa)(\nabla W)_I^C \cdot \vec{n}_{IJ} + \kappa(\nabla W)_I^U \cdot \vec{n}_{IJ}\right] \tag{5.110}$$

$$W_{JI} = W_I + \frac{1}{2}\left[(1-\kappa)(\nabla W)_J^C \cdot \vec{n}_{JI} + \kappa(\nabla W)_J^U \cdot \vec{n}_{JI}\right] \tag{5.111}$$

The table below shows the theoretical order of accuracy of the different schemes for calculating convective flux on a structured mesh.

Table 5.3: *Flux Calculation Methods*

Flux Calculation Method	α	κ	Spatial Order of Accuracy
F2	1/2	1	2
F31	1/2	1/3	3
F32	1/10	1/3	3

Decreasing κ leads to a higher spatial order of accuracy. Decreasing α leads to lowering the artificial diffusion term in the Roe flux calculation method. When $\kappa = 0$ or $\alpha = 0$, the scheme is totally centered and so unstable. This artificial diffusion removes energy from smallest scales without contaminating the large scales. It is argued [42] that the details of how this energy is removed are not very important.

The idea behind this ILES methodology, as shown by Margolin et al. [62], is based on the physical significance of the truncation errors of the spatial discretization. These truncation errors can be related to the correction necessary for the discretized finite volume equations to represent the governing equation of an infinitesimal point of fluid. Hence, it is claimed that such terms are not the numerical error but also they legitimately describe the physics of the flow [62]. Flow realization using implicit LES is also helpful to understand the behavior of numerical diffusion and its interaction with SGS models in explicit SGS modeling.

5.6 Explicit Filtering

For the use in dynamic sub-grid scale modeling, an explicit filter is constructed following the procedure of Marsden et al. [63]. This filter commutes with differentiation up to second order of accuracy. Commutative filter construction starts by definition of its moments which is then used to achieve second order commutation accuracy. Filter moments are defined using filter kernel G and filter size Δ, as

$$m^{\alpha\beta\gamma}(\vec{x}) = \frac{1}{\Delta^3} \iiint_{\Omega} \eta_1^{\alpha} \eta_2^{\beta} \eta_3^{\gamma} \, G(\vec{x},\eta) \, d\eta_1 \, d\eta_2 \, d\eta_3 \tag{5.112}$$

where $\eta_i = (x_i - y_i)/\Delta$. To achieve second order commutation error the following conditions should be satisfied,

$$m^{\alpha\beta\gamma}(\vec{x}) = \begin{cases} 1 \ \mathit{if} \ \ \alpha = \beta = \gamma \\ 0 \ \mathit{if} \ \ \alpha + \beta + \gamma = 1 \end{cases} \tag{5.113}$$

These conditions are met for interpolation-based filters [64]. Interpolation is done by finding 4 points around the node under consideration, in form of a tetrahedron as filtering window. A first-order polynomial is passed through the four neighboring vertices. The weight of each vertex of the tetrahedron is chosen, following [64], as follows: the first-order polynomial interpolant is defined as,

$$P(x,y,z)=a_0+a_1(x-x_0)+a_2(y-y_0)+a_3(z-z_0) \tag{5.114}$$

with (x_0,y_0,z_0) being the node which is going to be filtered. The Lagrange interpolation form of the linear interpolating function at the point (x_0,y_0,z_0) is written as follows,

$$P(x_0,y_0,z_0)\equiv P_0=w_1P_1+w_2P_2+w_3P_3+w_4P_4 \tag{5.115}$$

with P_1, P_2, P_3, and P_4 being the value of the interpolant at 4 vertices of the filtering tetrahedron. These weight are simply calculated from the system of equations $A\vec{w}=\vec{b}$, where

$$A=\begin{bmatrix} 1 & 1 & 1 & 1 \\ x_1-x_0 & x_2-x_0 & x_3-x_0 & x_4-x_0 \\ y_1-y_0 & y_2-y_0 & y_3-y_0 & y_4-y_0 \\ z_1-z_0 & z_2-z_0 & z_3-z_0 & z_4-z_0 \end{bmatrix}, \quad \vec{b}=\begin{bmatrix} 1 \\ 0 \\ 0 \\ 0 \end{bmatrix} \tag{5.116}$$

To attain more flexibility in filter width and shape, 7 different tetrahedral are found around each node. The weight of each tetrahedron is found, following Ciardi et al. [65], by matching the resulting filter with an equivalent isotropic spherical top-hat filter with filter size of Δ. For the equivalent top-hat filter, one can write

$$M^{200}=M^{020}=M^{002}=\frac{3}{10}\Delta^2 \tag{5.117}$$

$$M^{110}=M^{101}=M^{011}=0 \tag{5.118}$$

The filterering weight of each tetrahedral is given by the solution of the following system of equations,

$$\sum_{i=1}^{7} m_i^{\alpha\beta\gamma}\beta_i=M^{\alpha\beta\gamma} \qquad \text{where} \quad \alpha\beta\gamma=200,020,002,110,101,011$$

$$\beta_0 + \sum_{i=1}^{7} \beta_i = 1 \tag{5.119}$$

where β_i is the weight assigned to the ith basic filter, and β_0 is the weight associated to the filtered point under consideration which is set to 0.5 as recommended in reference [65].

5.7 Implicit Filtering

Implicit filtering has been done using the effect of differential operators of finite element method as an implicit filter. For the implicit filtering, it is assumed that for the largest to shortest edge ratio of at most 1000, the implicit filter can be used for static Smagorinsky model and as the grid filter of dynamic Smagorinsky model.

5.8 LES Models Implemented in This Work

In this work LES is modeled by solving the filtered governing equations using Favre Average (section 5.3.1) and by using filtered energy and modified pressure (system II). For SGS stress modeling, Smagorinsky, dynamic Smagorinsky and Implicit LES models were implemented. The Smagorinsky coefficient C_S is evaluated using the equation 5.60 and 5.61. The filtered strain $\widetilde{S}_{kl}$ is found from the grid filter velocity. Also, in Yoshizawa relation 5.62, the coefficient C_I for modeling the isotropic part of the SGS stress is assumed to be equal to the Smagorinsky coefficient C_S used for modeling the deviatoric part of the SGS stress tensor. For dynamically evaluating the Smagorinsky coefficient C_S, Lily proposal [60] (equation 5.104) is used. Tensors M_{ij} and L_{ij} are evaluated from the resolved field using the grid filter and a test filter. The test filter is chosen to a discrete interpolation filter with a commutation error of second order accuracy conforming to the second order numerical method used in this work. The filtered strain $\widetilde{\widehat{S}}_{kl}$ is found by filtering the grid filter velocity using the discrete interpolation filter and then differentiating the test filter velocity field. For the sake of simplicity, the turbulent Prandtl number is assumed to be equal to the laminar Prandtl number and equation 5.108 is not used. ILES method is considered using different flux calculation methods according to table 5.3.

Chapter 6

RESULTS AND CONCLUSIONS

In this chapter the LES results for flow over a gas turbine blade is presented. A high pressure gas turbine rotor blade profile (RS1S profile of SNECMA) mounted in two-dimensional linear cascade arrangement is selected for this purpose. The cascade is composed of 6 blades, i.e. 5 passages. The 3rd (counted from top) profile was instrumented either for static pressure or heat flux measurements. The blade geometry is shown in figure 6.1,

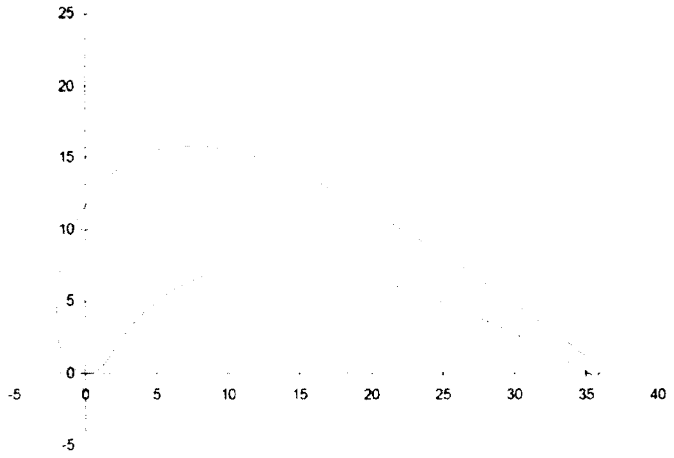

Fig. 6.1: *Geometry of the 2D RS1S rotor blade*

The main geometrical characteristics of the blade is summarized in table 6.1,

Table 6.1: *Geometrical characteristics of the blade*

Chord length c	35.906 mm
Pitch to chord ratio	0.7607
Blade height to chord ratio	1.393
Stagger angle (from tangential direction)	58.38 deg
Inlet flow angle (from axial direction)	53.36 deg
Inlet flow angle (from axial direction)	-65 deg

Measurements were performed at von Karman Institute by Arts et al. [66] under operating conditions encountered in modern aero-engine. By independent variations of exit Mach (0.8 ... 1.3) and Reynolds number (5e05 ... 2e06), free stream turbulence (1 ... 6 %), and incidence angle (-14 ... +11 deg), a detailed data base of test results for blade isentropic Mach number and heat transfer coefficient is provided. This case is used at SNECMA for validation purposes. Test facility allows for an independent selection of Mach and Reynolds number as well as gas to wall temperature ratio. Air was used as a working fluid and typical test duration was about 0.5 second.

Free stream total pressure and temperature, static pressure and turbulence intensity were quantified at 1/2 axial chord length upstream of the leading edge. Exit isentropic Mach number was quantified at 1/3 axial chord downstream of the trailing edge by pressure taps that covered almost 2.5 pitches to qualify downstream periodicity. The blade Mach number distribution was determined by 27 static pressure taps distributed at mid-height around the blade profile. Isentropic Mach number is only a function of non-dimensional pressure and it is found using the following relation, proved in Appendix B,

$$\frac{p}{p_{o,in}} = \left(1 + \frac{\gamma - 1}{2} M_{is}\right)^{\frac{\gamma}{\gamma - 1}} \tag{6.1}$$

where $p_{o,in}$ is the total inlet pressure which is also used to non-dimensionalize the pressure. The uncertainty on pressure was $\pm 0.5\%$.

The convective heat transfer measurement at the wall was determined by means of a transient technique. The convective heat transfer coefficient is defined as the ratio of the measured wall heat flux and the difference between the total free stream and the local wall temperature as given below,

$$h = \frac{\dot{q}_w}{T_{o,in} - T_w} \tag{6.2}$$

The heat flux gauges were about 20mm long and the heat transfer measurements describe some kind of spanwise average. The uncertainty on heat transfer coefficient was $\pm 5\%$.

Results distribution are presented for a coordinate along the blade, s, which is 0 at point (0,0) and it is maximum at (c,0) referring to figure 6.1. s is positive for suction side (upper surface) and negative for pressure side (lower surface).

The physics of flow is explained in [66]. Isentropic Mach number and heat transfer coefficient are selected in experiment. Isentropic Mach number distribution which is also called blade velocity not only reveals pressure distribution on the blade but also it gives information on flow acceleration and favorable or positive pressure gradient which can be indicators of existence of a separation zone. In the separation zone however this variable maintains the same level. Heat transfer coefficient is a very important design parameter in modern engines. It also discloses important information on the regime of boundary layer being laminar or turbulent as well as on the transition point.

Isentropic Mach number distribution on the blade is quite sensitive to inlet incidence angle and exit Mach number. At positive incidences, blade velocity reaches a sharp peak on the suction side and an early transition of the suction side boundary layer occurs. At negative incidences, the velocity peaks on the suction side and pressure side decrease and acceleration becomes much more continuous. This leads to development of a laminar boundary layer. In addition, different back pressures significantly change the blade velocity on the rear part of the suction side. Both incidence angle and back pressure change the boundary layer development. However, more rigorous study of boundary layer development requires studying heat transfer coefficient. Two other flow variables play major role in blade heat transfer, turbulent intensity and Reynolds number.

Increasing turbulent intensity augments laminar heating in the leading edge area and along the laminar part of the suction side. At lower inlet turbulent intensity (0.8%), boundary layer on the suction side remains laminar until the s=40 mm where the shock impinges on the blade surface. At higher inlet turbulent intensity (4%), transition is triggered much upstream at s=18 mm and the stabilization effect of the favorable pressure gradient decreases the heat transfer coefficient due to reacceleration of the flow from s=18 – 40 mm until the location of shock/wall interaction. Reynolds number has the similar effect. At lower Reynolds number boundary layer stays laminar until shock impingement. But at higher Reynolds number transition is undergone upstream the shock position. Overall, increasing Reynolds number leads to more upstream transition and overall enhancement in heat transfer.

A small recirculation bubble exists at the beginning of the pressure side which manifests itself by strong heat transfer variation due to the separation and reattachment of the flow in that region. The amplitude of this variation is not a function of Reynolds number but it is strongly reduced for higher turbulent intensity. Increasing the Reynolds number increases the heat transfer coefficient on the pressure side.

The effect of exit Mach number on heat transfer coefficient is similar to that of pressure distribution, i.e. it makes changes only in the rear part of the suction side and in the region of shock/boundary layer interaction. In the transonic and supersonic regimes, the boundary layer grows faster and heat transfer coefficient decreases. The effect of inlet incidence on heat transfer coefficient is also analogous to that of pressure distribution, i.e. at higher incidences, the transition is set off more upstream on the suction side and at lower incidences, the effect of the separation bubble on the pressure side is more pronounced.

Arts et al. [66] also simulated this flow using a SNECMA-ONERA Navier-Stokes solver. The solver computes compressible flows with finite-volume and time marching techniques on multi-block structured grids. Both experimental and RANS data will be used herein to verify the LES results.

The test conditions considered here are the transonic flow at two flow angles, i.e. $I = 53.36^{\circ}, 64.36^{\circ}$. The first one corresponds to the design flow angle with least separation possible. The second angle is $I = 11^{\circ}$ higher than the design flow angle. Experimental isentropic Mach number at the outlet is reported to be 0.844 [66]. However, as suggested in [66], this value should be adjusted to a few percent for a better agreement with experimental results. Here, M_{is} at outlet is adjusted 16% to get the best match with LES results.

Pressure distribution is known to be the first parameter to be used in verification of new turbulence models. Other flow statistics such as Reynolds stresses are more rigorous verification parameters. The large separation that exists in the second test case, $I = 63.36^\circ$, is a suitable condition to assess whether LES performs better than RANS models. In incompressible and low speed subsonic flows, pressure distribution over the blade is an inviscid phenomenon which is even resolvable with Euler models and the choice of turbulence model has no significance. However, in the transonic regime of the flow with existence of several weak and strong shocks on the blade and their interaction with the boundary layer at a very high angle of attack, the physics of the flow is viscous dominated and LES and RANS results are completely distinguishable. This different is more pronounced in off-design conditions due to the existence of a separation region.

Mesh generation is a major step of LES calculations. The criteria for mesh size are as follows: mesh has to be fine enough to resolve the wave-numbers in -5/3 law (figure 5.2) and the resolved domain has to contain at least 80% of the flow energy. Also in the near wall region, mesh has to be finer than the viscous length scale, i.e. $y^+ = 1$. The Kolmogorov length scale for this flow, assuming $\mathrm{Re} = 0.54e06$, is $\eta / l_0 \approx \mathrm{Re}^{-3/4} = 5.02e-05$, where l_0 is the flow length scale, i.e. chord length here. According to RANS simulations of this flow [66] of the of the first cell is located at $l(y^+ = 1)/chord = 2.8e-04$, that is, for DNS of this flow there is a need to have elements with edge length of $\eta \approx l(y^+ = 0.2)$. Such a DNS mesh is impossible to create for our resources. However, the inertial sub-range of the flow is the length scales in the interval $60\eta << l << l_0/6$. 60 times large than the Kolmogorov scales means $60\eta \approx l(y^+ = 30)$.

In this work, two levels of mesh resolutions are considered here. The resolution of the mesh on the wall is $\Delta y^+ \approx 5$ and $\Delta x^+ = \Delta z^+ \approx 25$ in wall units for coarse mesh and $\Delta y^+ \approx 0.5$ and $\Delta x^+ = \Delta z^+ \approx 10$ for fine mesh. After 20-30 boundary-layer type layers of structured mesh with the ratio of 1.2, the boundary mesh is smoothly mixed with the outer unstructured mesh. The largest edge length is the same in both meshes, $\Delta y^+ \approx 50$ if measured using the corresponding values on the wall, leading to a largest edge to shortest edge ratio of 10 and 100 in coarse and fine meshes respectively. Both meshes are well inside the inertial sub-range region of the flow. The effect of near-wall resolution can be best seen from the difference in the simulations of these two meshes since the fine mesh has higher near-wall resolution with the nearly same domain resolution compared to the coarse mesh and maximum edge length of both meshes are the same. No near-wall model is used in either case. It is assumed that within this limit of largest to shortest edge ratio, the implicit filter can be used for static Smagorinsky model and as the grid filter of dynamic Smagorinsky model. The coarse mesh consists of nearly 0.5 million nodes (2.5 million elements) while the fine mesh is composed of 2.5 million nodes (13 million elements). The coarse mesh is partitioned to 8 sub-domains while 32 CPUs are found to be enough to run the fine mesh.

Time stepping is another major issue in LES calculations. Very fine mesh usually results in very small time steps. However, as we use implicit methods, it is possible to increase the CFL number without stability problems. The maximum time step is found by looking into Kolmogorov scales. Largest edge in the flow is 100 times larger than Kolmogorov length scale. Hence, the first attempt can be choosing maximum time-steps to be 100 times larger than Kolmogorov time scale. The Kolmogorov time scales of this flow, assuming $\mathrm{Re}=0.54e06$, is $t_\eta/t_0 \approx \mathrm{Re}^{-1/2}=1.36e-03$. t_0 is the time scale of the flow which is around 1.0e-04 second which is 1000 times larger than t_η. The maximum time-step will then be used in extracting the statistics of the data. In this work, two sampling strategies are used. In the more expensive one, the maximum time step in the simulation is chosen to be $\Delta t_{\max}/t_0=0.1$ and the number of data sampling is 1000. In the less expensive one, the maximum time step in the simulation is chosen to be $\Delta t_{\max}/t_0=1$ and the number of data sampling is 400. It is found that, the results of both sampling strategies are identical for pressure distributions.

Each case runs until the flow becomes statistically steady. This is ensured by monitoring pressure and aerodynamic forces on the blade and residuals. Then the problem is run for a period of time, according to above-mentioned sampling strategies, which is assumed to be much longer than the period of flow oscillations. Then the data statistics are extracted.

The results are presented for Smagorinsky, ILES, and Dynamic Smagorinsky models to investigate the effect of different SGS modeling approaches. They are all calculated using the second-order accurate convective flux calculation. Afterwards, the interaction of numerical scheme artificial diffusion and turbulent SGS modeling is explored by changing the order of accuracy of the convective flux calculation as well as changing the coefficient of artificial diffusion in $\kappa-\alpha$ convective flux calculation.

6.1 Qualitative Study

Different flow variables are shown in the following figures to give a qualitative study of the simulation.

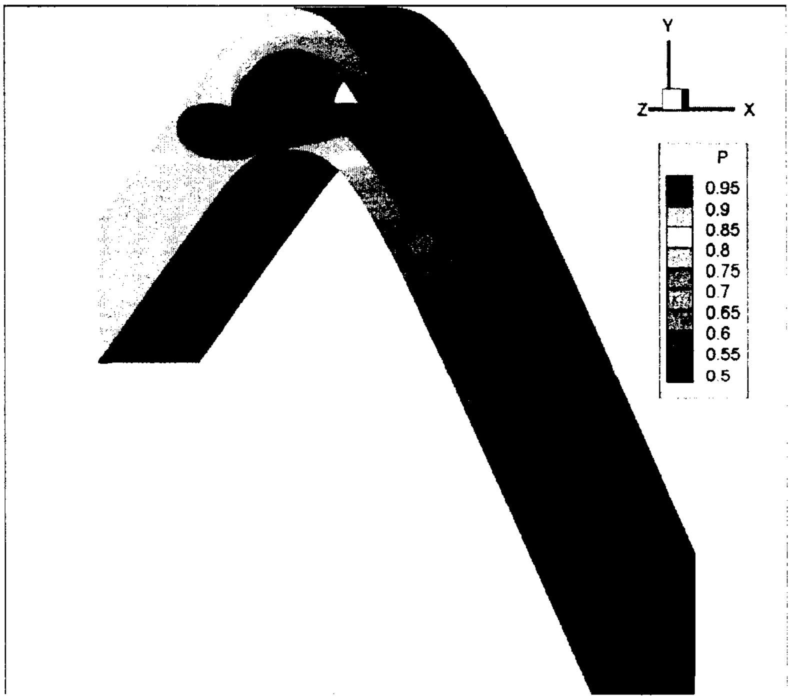

***Fig. 6.2:** Instantaneous Pressure Field*
Design Condition

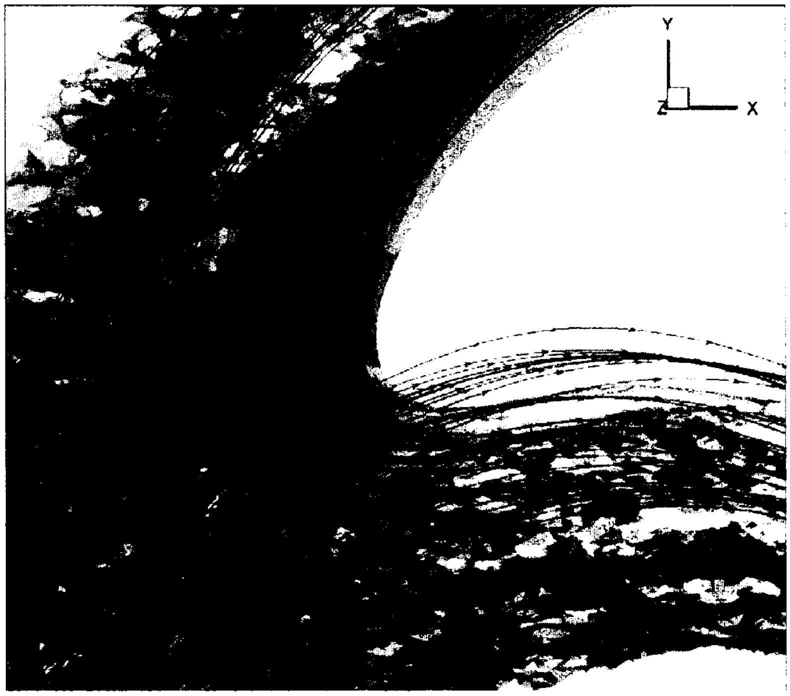

***Fig. 6.3:** Instantaneous Streamlines and Vorticity Isosurfaces*
Leading Edge - Design Condition

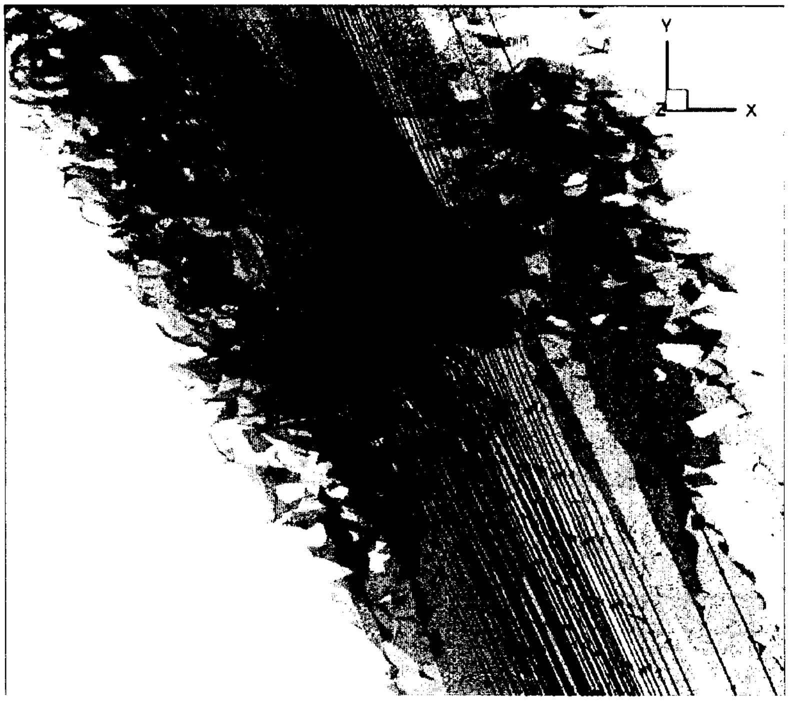

***Fig. 6.4:** Instantaneous Streamlines and Vorticity Isosurfaces Trailing Edge - Design Condition*

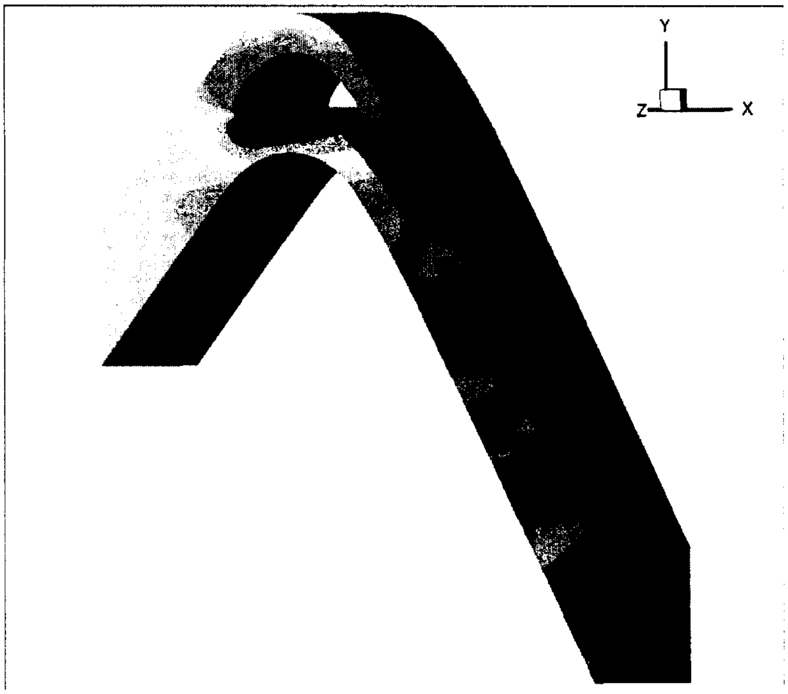

***Fig. 6.5:** Instantaneous Pressure Field Off-Design Condition*

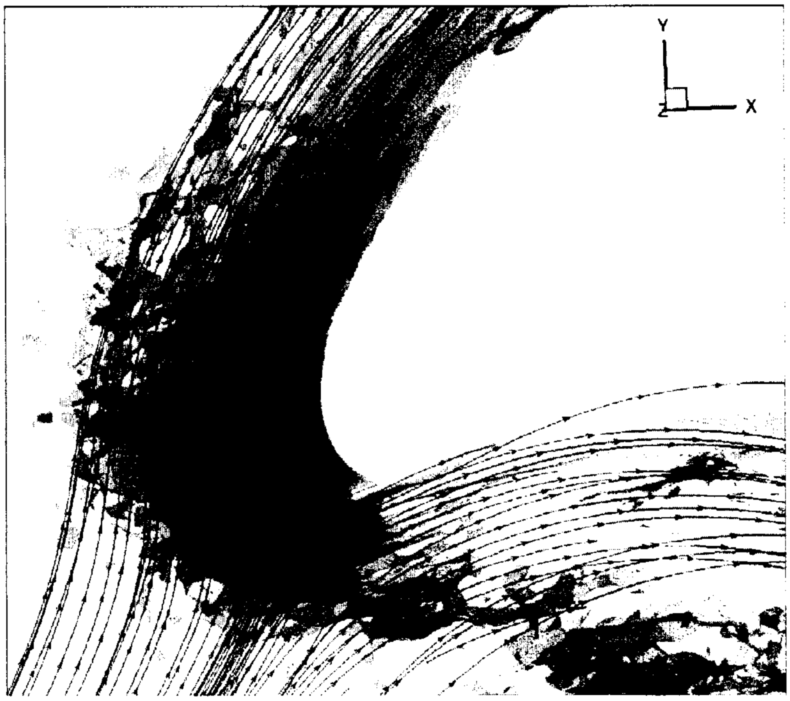

Fig. 6.6: *Instantaneous Streamlines and Vorticity Isosurfaces Leading Edge – Off-Design Condition*

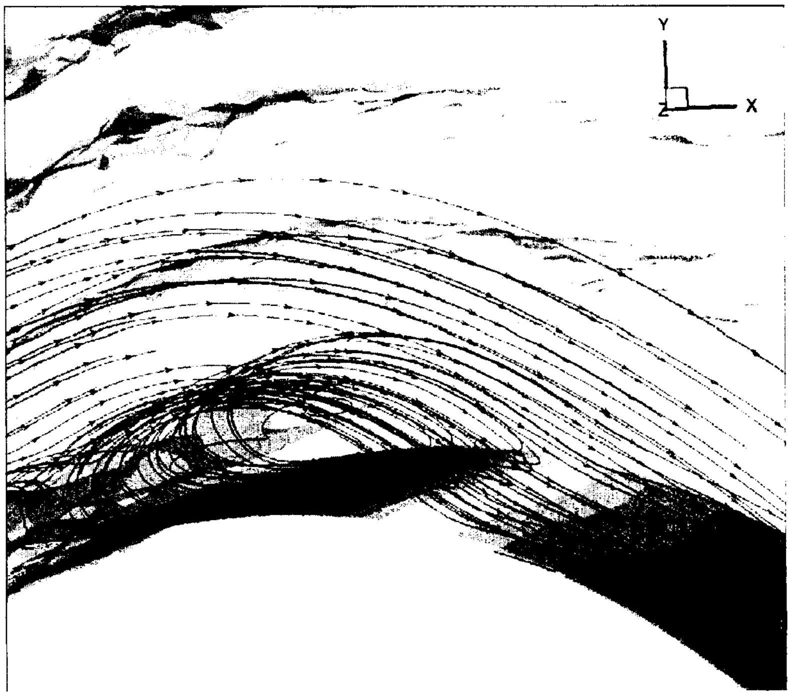

Fig. 6.7: *Instantaneous Streamlines and Vorticity Isosurfaces Suction Side – Off-Design Condition*

Fig. 6.8: *Instantaneous Streamlines and Vorticity Isosurfaces Suction Side – Off-Design Condition*

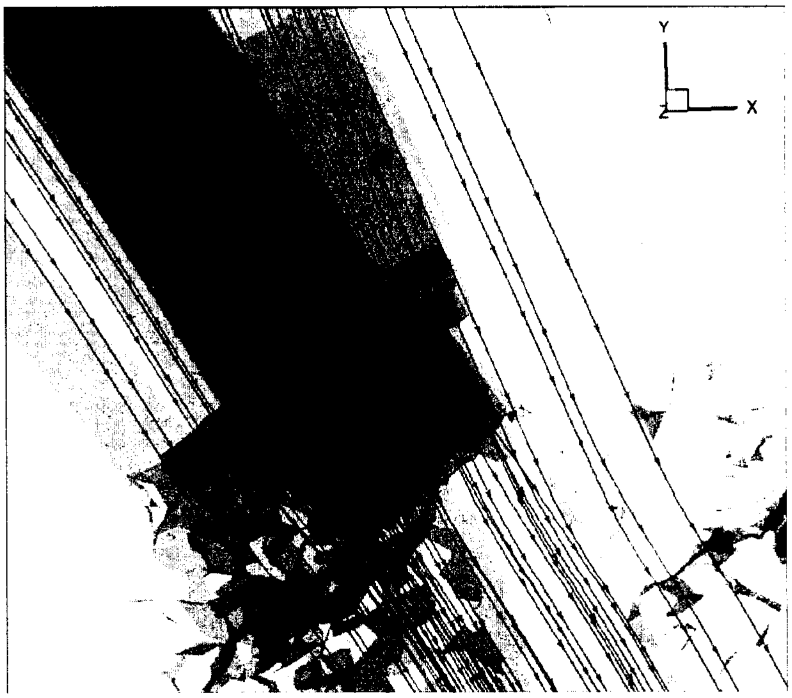

Fig. 6.9: *Instantaneous Streamlines and Vorticity Isosurfaces Trailing Edge – Off-Design Condition*

The figures 6.2-6.9 show the qualitative behavior of the instantaneous flow field. As seen from these figures, at design condition the flow is completely attached to the blade and pressure field is completely different from the off-design conditions in which several flow separation bubbles exist.

6.2 Sensitivity Analysis

To further investigate the flow behavior and the effect of different flow conditions, the pressure distribution over the blade is investigated which is the most important flow variable in engineering. Effects of the two main flow parameters are explored in this section, namely inlet flow angle and back pressure. The results are presented as isentropic Mach number M_{is}, which represents pressure, versus the stream-wise length of the blade s . The pressure side is the region ($s<0$) and suction side is the region ($s>0$). The blade length is non-dimensionalized using its maximum value on both side $s_{\max}$. $s_{\max}$ is total length of the suction side for $s>0$ and total length of the pressure side for $s<0$. This value for suctions side is nearly twice this value for pressure side.

Effect of the flow angle in isentropic Mach number is shown in figures 6.10 and 6.11 for two different back pressures. It can be seen that the first jumps in the M_{is} on both pressure side ($s<0$) and suction side ($s>0$) depends mainly on the flow angle. The experimental data in these figures correspond to the flow angle $I=53.36^{\circ}$. The solid lines in the following figure correspond to the results for the experiment condition.

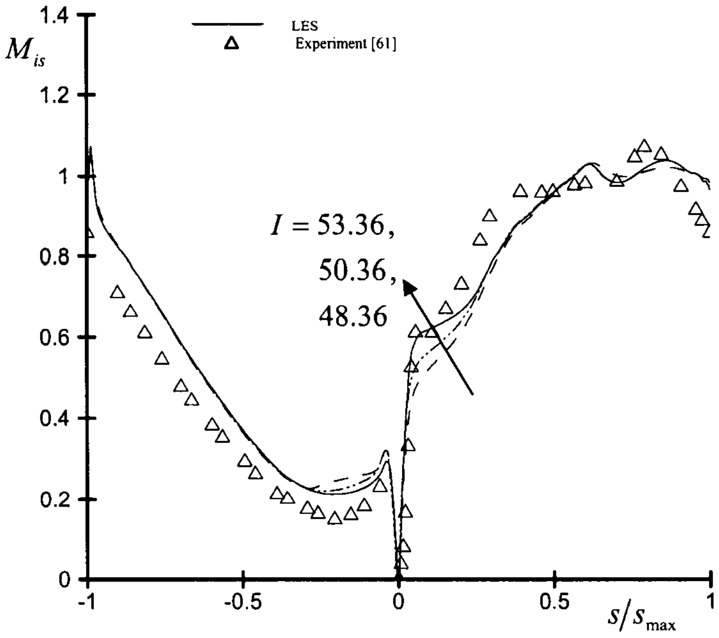

Fig. 6.10: *Different Flow Angles at* $M_{is_{back}} = 0.95$

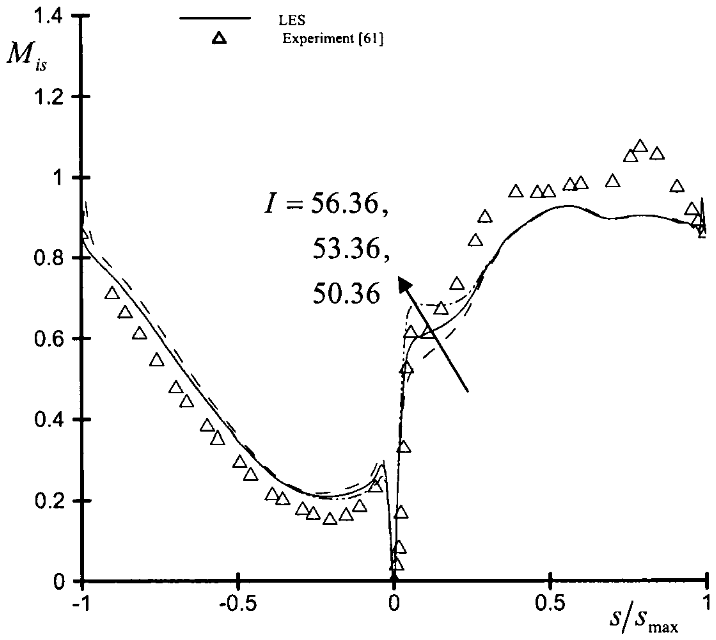

Fig. 6.11: *Different Flow Angles at* $M_{is_{back}} = 0.844$

Effect of back pressure is shown in figures 6.12 and 6.13 for the flow angle $I = 53.36^\circ$

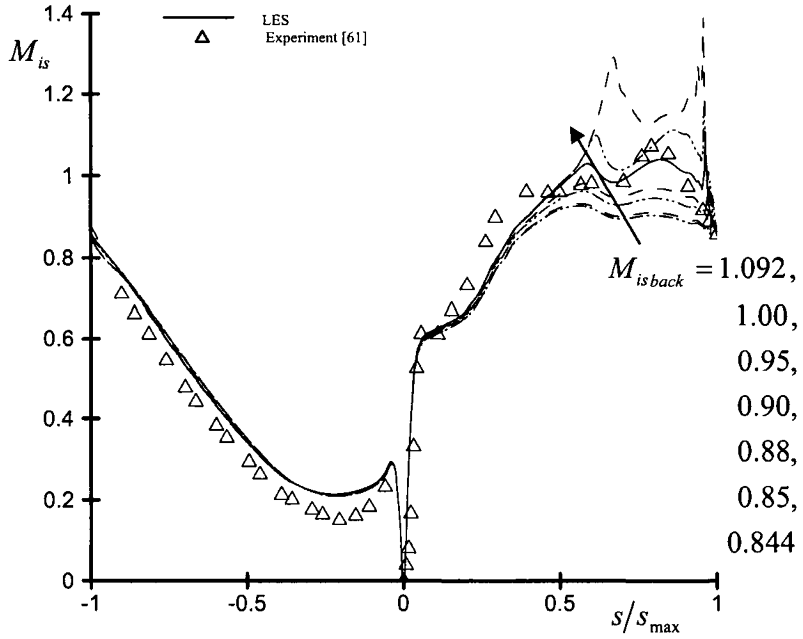

Fig. 6.12: *Different Back Pressure at* $I = 53.36$

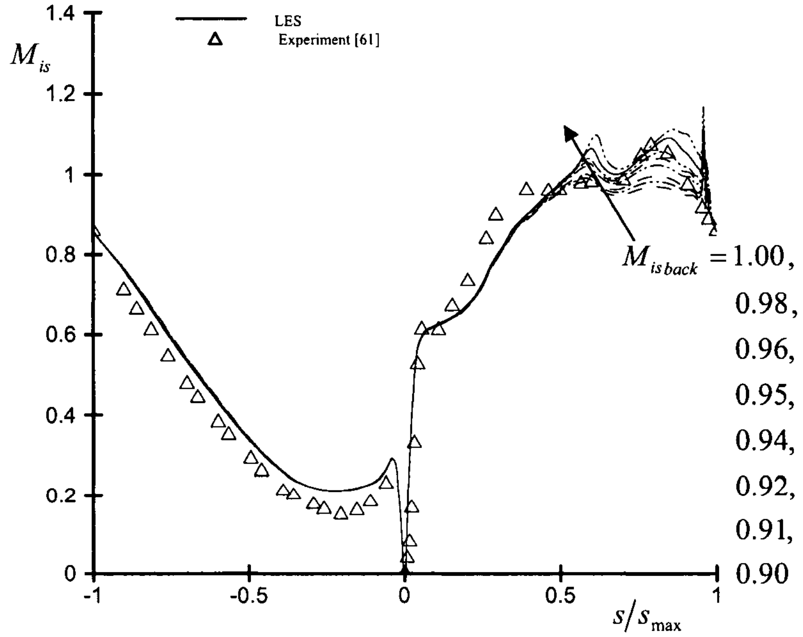

Fig. 6.13: *Different Back Pressure at* $I = 53.36$

It is clearly seen from figure 6.12 and 6.13 that on the pressure side ($s<0$), after the first jump in M_{is} results, rest of the M_{is} distribution remains constant regardless of the back pressure. However, on the suction side ($s>0$), M_{is} distribution varies significantly with back pressure. As stated before, the back pressure is adjusted in the numerical solution to have the best match with experimental data. In two levels of back pressure adjustment, figures 6.12 and 6.13 respectively, the back isentropic Mach number of 0.98 was found to best represent the experimental data which is shown by a solid line. The distribution which has the closet match with experimental data is shown by solid line in these figures.

6.3 LES Verification at Design Angle of Attack

In this section LES results will be presented and validated in this section. These results corresponds to $\mathrm{Re}=0.54e06$, $T_{o,in}=415K$, and adiabatic walls.

6.3.1 Smagorinsky Model

Figures 6.14 and 6.15 show the isentropic Mach number distribution on the blade using the Smagorinsky model for coarse and fine meshes respectively. The effects of the addition of Yoshizawa model for τ_{kk} (modeling the term C_2) as well as Van-Driest damping function have been explored.

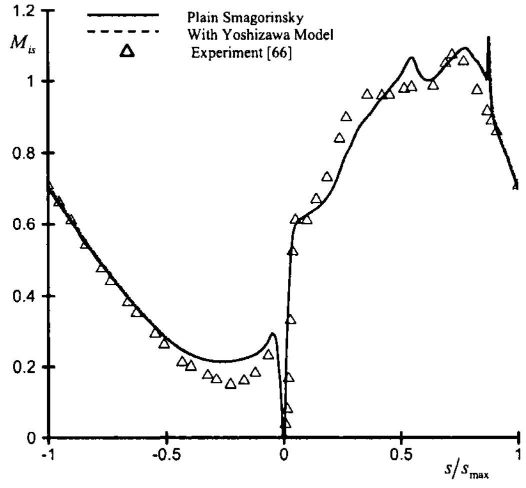

***Fig. 6.14:** Coarse Mesh Smagorinsky Model*

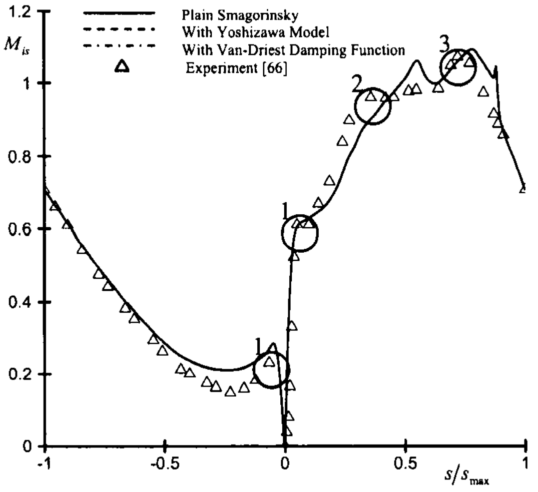

***Fig. 6.15:** Fine Mesh Smagorinsky Model*

Yoshizawa model by modifying pressure is expected to change the isentropic Mach number distribution which is a function of non-dimensional pressure only. However, figures 6.14 and 6.15 which show that Yoshizawa model makes a very small change on the coarse mesh while it has almost no significance on the fine mesh in this flow condition and the results of the Smagorinsky model with or without the τ_{kk} modeling fall on the same line. Furthermore, Van-Driest model for correcting the viscosity near the wall is expected to improve the flow variables distributions on the blade. However, for the coarse mesh, Van-Driest damping function makes the solution unstable and it is not shown here and in case of the fine mesh it makes almost no difference in pressure distribution on the blade. These results suggest that for a sufficiently fine mesh, all variations of the Smagorinsky model lead to the same pressure distribution.

The trend of the isentropic Mach number distribution is found well using different variations of the Smagorinsky model. Three jumps in M_{is} on the suction side (positive s) and one jump in M_{is} on the pressure side (negative s) are distinguishable in the experimental data and they are shown by circles in figure 6.15. The first jumps at point 1 on both suction and pressure sides are mainly a function of angle of attack and it is accurately captured. The pressure side jump is overestimated. The last two jumps on the suction side are mainly dependent on the back pressure. After point 2, pressure, hence M_{is}, reaches a plateau that LES calculation fail to capture. At point 3, again LES results seem to capture the shock behavior fairly well.

6.3.2 ILES Model

Figure 6.17 shows the isentropic Mach number distribution on the blade using the ILES model for coarse and fine mesh resolutions.

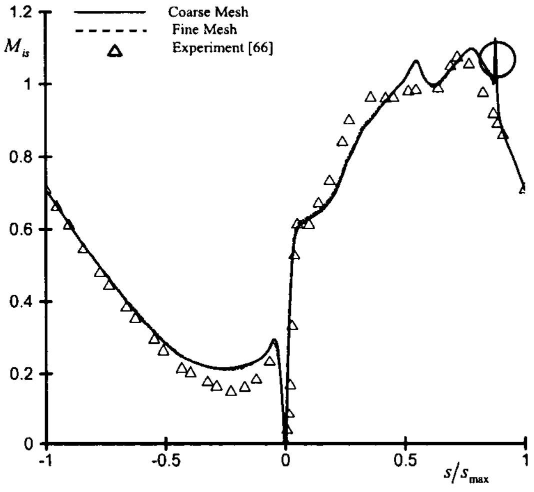

***Fig. 6.16:** ILES Model*

The effect of the artificial diffusion of the numerical method has been investigated in these figures. Although the diffusion of the coarse mesh is higher than that of the fine mesh, according to the ILES results, there is not a significant difference between the results of the two mesh resolutions. The results on the two mesh resolution level is almost the same but fine mesh has a smoother pressure variation on the blade. The sharp jump in M_{is} numerical results on the pressure side near the trailing edge, which is shown by a circle in figure 6.16, is much lower on the fine mesh. Other SGS models also retain the same behavior. This jump exists even in the RANS results [66] and it is much larger than the LES results.

6.3.3 Dynamic Smagorinsky Model

Figures 6.17 and 6.18 show the isentropic Mach number distribution on the blade using the Dynamic Smagorinsky model for coarse and fine meshes respectively. These figures also contain the Smagorinsky and ILES results to provide a comparison among different SGS models.

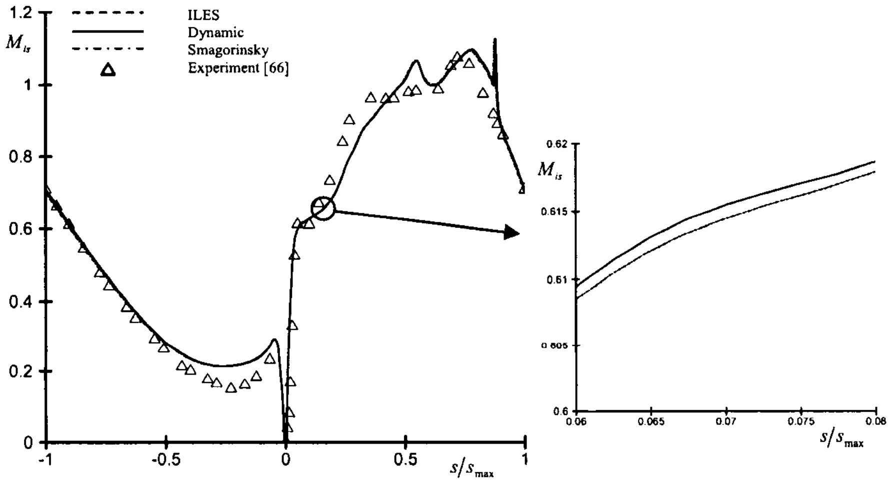

Fig. 6.17: *Coarse Mesh Different SGS Models*

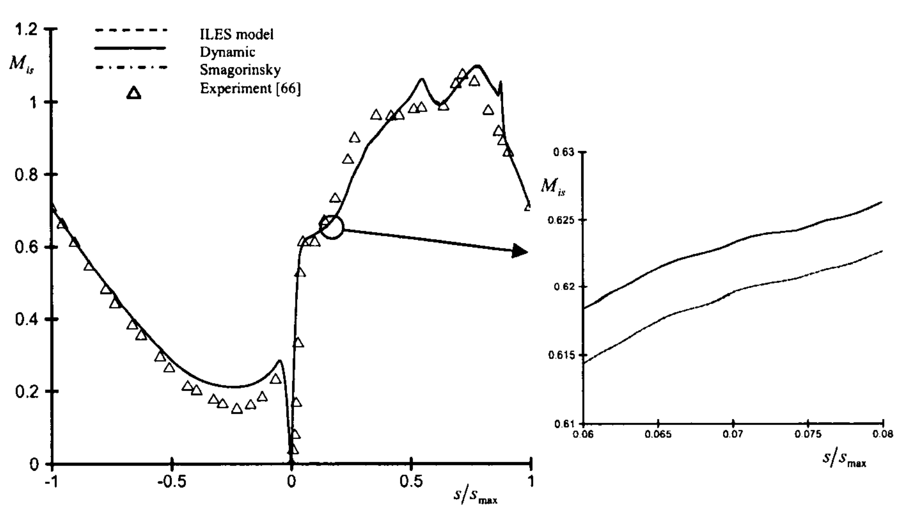

Fig. 6.18: *Fine Mesh*
Different SGS Models

ILES is the case with least amount of viscosity, while the Smagorinsky model has the highest viscosity. Dynamic Smagorinsky results always fall between the other two, on the grounds that this model by adjusting the amount of turbulent viscosity, based on the dynamics of the flow, provides a moderate turbulent viscosity. This is shown by zooming into figures.

As shown in figures 6.17 and 6.18, the dynamic Smagorinsky results are almost identical to the ILES results. This behavior stems from the fact that by dynamically finding the Smagorinsky constant C_S, its value becomes very small. The maximum value for the Smagorinsky constant using its dynamic version is found to be $C_S^2 = 0.00034$ while this value is $C_S^2 = 0.01$ in the plain Smagorinsky model. This value depends on the choice of filter and definition of filter width. Using a sharp cut-off filter, Germano et al. [53] found this value to be around 0.023 in an incompressible turbulent channel flow while Moin et al. [54] for an incompressible isotropic turbulent decay found this value to be roughly between 0.008 and 0.014. Also as can be seen from figures 6.17 and 6.18, the results on the fine mesh are more sensitive to SGS models than that on the coarse mesh on the account that coarse mesh has a higher numerical diffusion.

6.3.4 Interaction of Artificial Diffusion with SGS Modeling

To study the interaction of numerical diffusion and LES turbulent diffusion, different methods of convective flux calculations, i.e. F2, F31, and F32 according to table 3.1, have been examined and shown in figures 6.19-6.22 for coarse and fine meshes using Smagorinsky and Dynamic Smagorinsky SGS models.

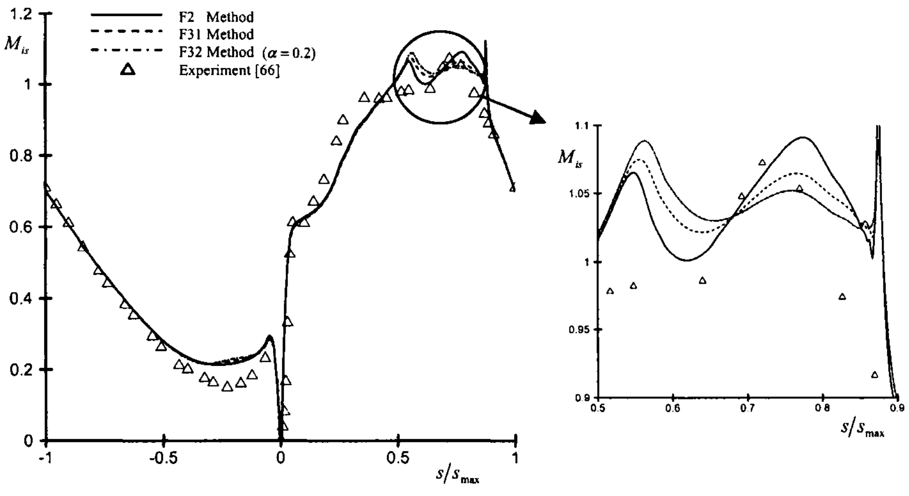

***Fig. 6.19:** Coarse Mesh*
Smagorinsky Model - Different Flux Accuracies

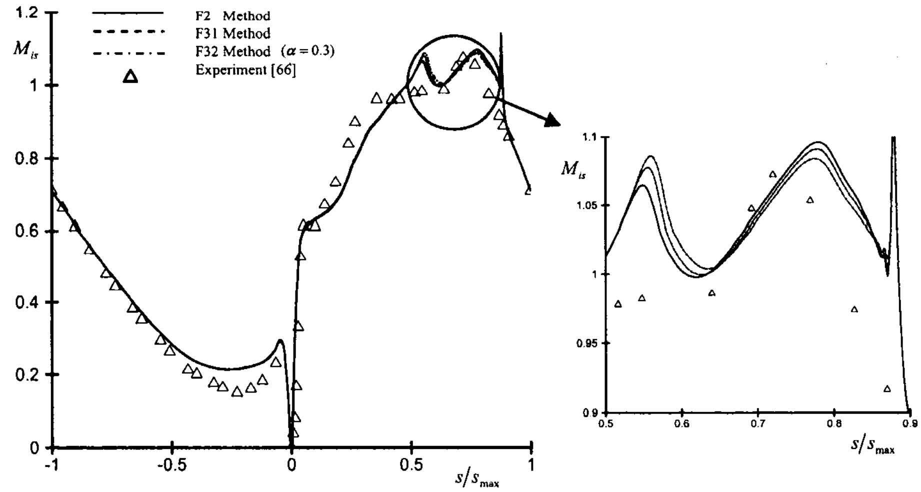

***Fig. 6.20:** Coarse Mesh*
Dynamic Model - Different Flux Accuracies

As previously discussed, owing to the fact that ILES results on both coarse and fine meshes are very close to each other, both meshes have responded the same to the artificial diffusion adjustment and on both meshes, the coefficient of artificial diffusion α can at most be reduced to 0.3 for ILES and dynamic SGS models and the solution still remains stable.

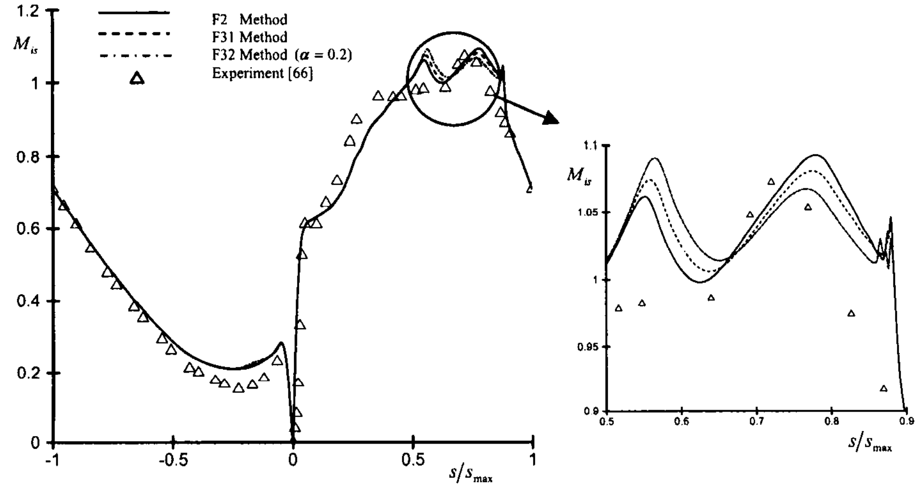

***Fig. 6.21:** Fine Mesh*
Smagorinsky Model - Different Flux Accuracies

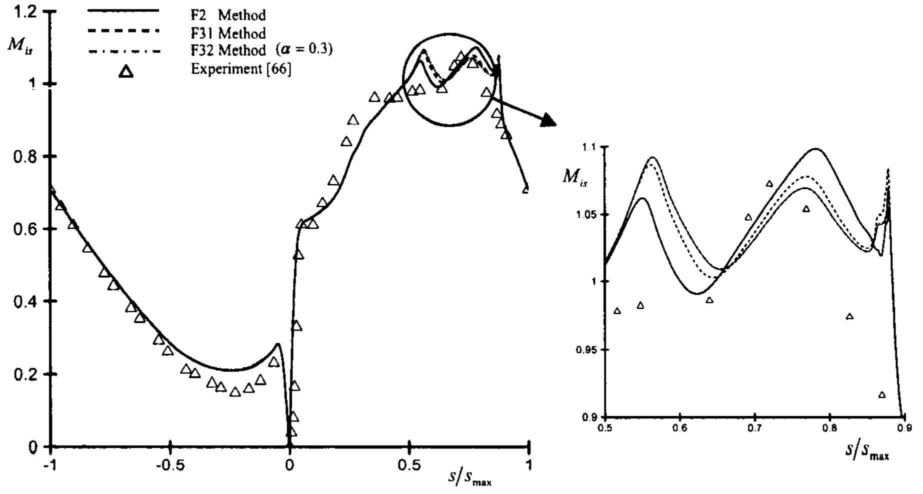

Fig. 6.22: *Fine Mesh*
Dynamic Model - Different Flux Accuracies

For Smagorinsky model α can even be reduced to 0.2. For α values lower than the above-mentioned values the solution becomes unstable.

As seen in figures 6.19 – 6.22, the only part of the flow to be affected by the artificial diffusion adjustment is the second half of the suction side which contains the shock zone. On the coarse mesh, the Smagorinsky model is more sensitive to the flux calculation method. However, on the fine mesh, the dynamic model is more sensitive to the flux calculation method.

6.4 LES and RANS Results at Design and Off-Design Conditions

Figures 6.23 and 6.24 show the isentropic Mach number distribution in the LES and RANS simulations respectively at design conditions $I = 53.36$. LES results corresponds to $M_{is_{back}} = 0.98$; however, there is ambiguity in the RANS back Mach number (it is said [66] to be 0.844 with some adjustments). This case is the hardest case to outperform the RANS simulations, on the account that RANS models perform well for pressure distribution on the wall at design conditions where the flow is attached. RANS models are derived based on flow characteristics on the wall and they do not behave as good throughout the flow. Also they have severe difficulties for non-attached flows, i.e. off-design conditions. As can be seen in figures 6.23 and 6.24, there are two local maximum in the LES Mach number on the rear suction side. This is the characteristic of transonic blades. One reason that it is not captured in RANS results is due to the unknown back Mach number which might not be as large as LES results. Figure 6.12 shows that for lower back Mach number, LES will not predict more than one local maximum at this region.

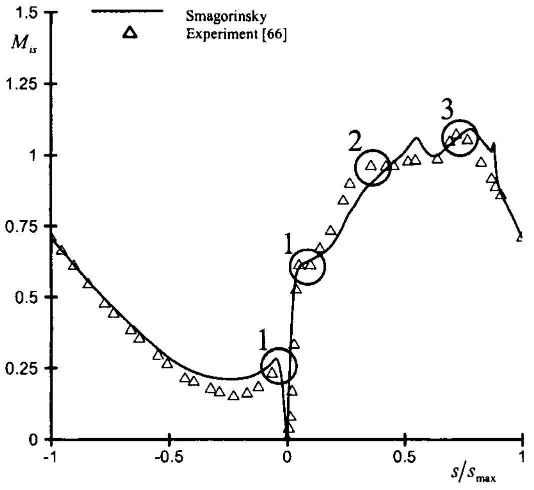

Fig. 6.23: Design Condition LES Result

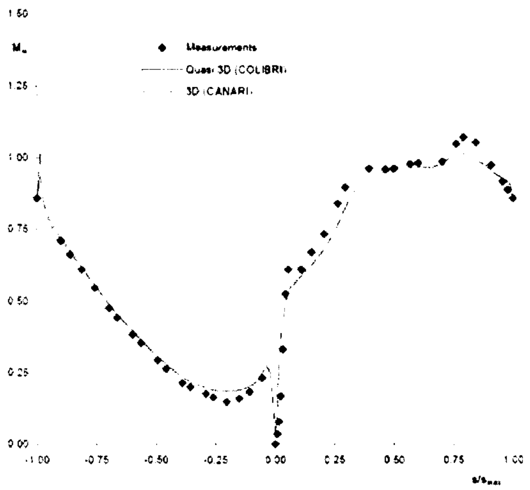

Fig. 6.24: Design Condition RANS Result [66]

Three jumps in M_{is} on the suction side ($s > 0$) and one jump in M_{is} on the pressure side ($s < 0$) are distinguishable in the experimental data and they are shown by circles in figure 6.23. The first jumps in isentropic Mach number on both suction and pressure sides (point 1 in figure 6.15) are mainly a function of angle of attack. Comparing to the RANS results presented in [66] using a 3D SNECAM-ONERA solver the first jump at point 1 on the suction side is much more accurately captured. The pressure side jump is overestimated in both LES and RANS results. The last two jumps on the suction side are mainly dependent on the back pressure. After point 2, pressure, hence M_{is}, reaches a plateau which is found well in RANS calculation but obviously LES calculation fail to capture it. At point 3, again LES results seem to capture better the shock behavior.

Figures 6.25 and 6.26 show the isentropic Mach number distribution in the LES and RANS simulations respectively at off-design conditions $I = 64.36$. The LES results correspond to $M_{is_{back}} = 1.22$; however, there is ambiguity in the RANS back Mach number (it is said [66] to be 1.088 with some adjustments). This case is a better case to show the superiority of the LES whose main characteristic is being able to resolve to separation bubble on the suction side and near the leading edge which can not be captured using RANS.

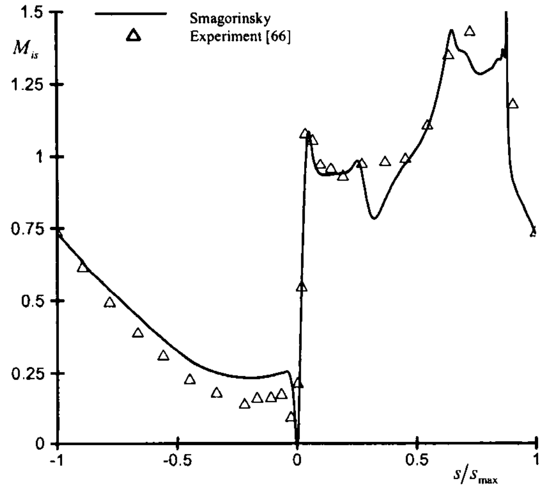

***Fig. 6.25:** Off-Design Condition LES Result*

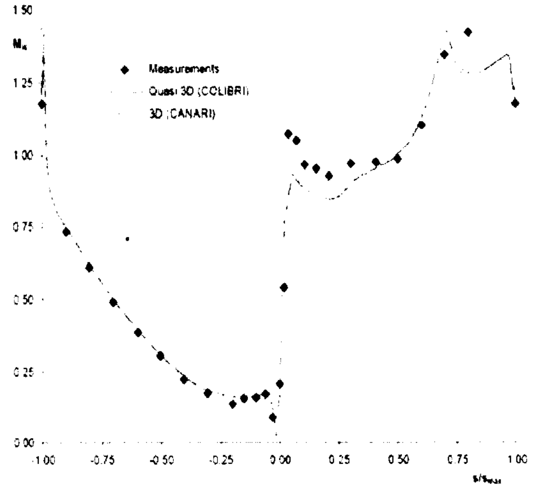

***Fig. 6.26:** Off-Design Condition RANS Result [66]*

As seen in figure 6.25 and 6.26, on the pressure side ($s < 0$) results are overestimated in LES while is found very well in RANS simulation. The most deficiency of the RANS simulation is on the suction side ($s > 0$) where the physics of the flow is very different than the pressure side. LES predicts the first jump in M_{is} very accurately in contrary to RANS. However, at the second jump in M_{is} on the suction side, LES results deviate significantly from the experimental data. This behavior is also seen in design condition.

As stated before, the RANS data are found by some back pressure adjustment. This change is vaguely stated to be "a few percent". In this work, based on the above-mentioned sensitivity analysis, the value 0.98 is found for the back isentropic Mach number at the design condition and 1.2 for off-design condition. The experimental values are 0.844 and 1.092 respectively. However, this ambiguity does not make the process of comparison difficult as far as the trend of the isentropic Mach number distribution is concerned. Even at lower back isentropic Mach number which is shown in figure 6.12, there are two bumps in LES results for M_{is} distribution, at point 2 and 3, that the first one is obviously not present in the experimental data and it is not shown in RANS distributions. As can be seen from the pressure field, figure 6.2, the region of very low pressure at point 2 is connected to the point 3 by periodicity, i.e. considering a linear cascade, point 3 on a given blade has the same x coordinate of the point 2 on the lower blade and point 3 is located just above point 2. That is, the flow structure is not found well on both suction and pressure sides. It might be due to the shortage of spanwise direction. It can also be a result of aspect ratio and skewness of the elements. However, removing each of these constraints leads to a much higher computation load. These issues are discussed in the last section.

6.5 Effect of Iso-Thermal Wall Conditioning

Up to now, presented results have been carried out using adiabatic wall conditioning which is the common practice in the analysis of turbo-machinery flows without cooling. But it is interesting to see the results of iso-thermal wall conditioning. The initial temperature of the wall is set to be 298 K and the inflow total stagnation temperature is 420 K. Figures 6.27 and 6.28 show the isentropic Mach number distribution versus non-dimensional axial chord for design and off-design conditions respectively. It can be seen from the following figures that iso-thermal and adiabatic conditions do not have a significant difference in predicting the pressure distribution on the wall. However, throughout the flow and especially for temperature distribution, the results are completely different.

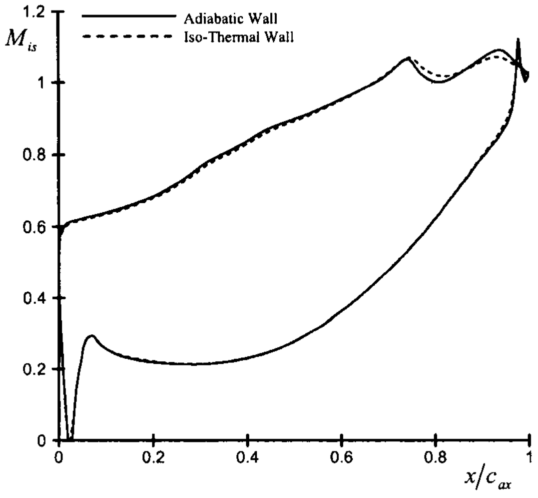

***Fig. 6.27:** Iso-Thermal Results*
Design Condition

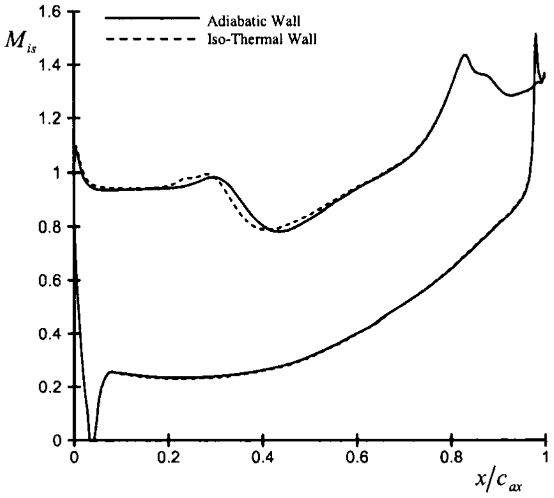

***Fig. 6.28:** Iso-Thermal Results*
Off-Design Condition

6.6 Effect of Spanwise Length

The computational cost of the LES simulation is determined by the resolution requirements. Grid spacing in the direction normal to wall has to be small enough to resolve dissipative scales. Also, the spanwise domain length has to be large enough to allow 3D turbulence structure evolving. Time step is also limited by considerations of numerical accuracy. An important limitation in the calculations up to now was the spanwise domain size. Due to the high computational costs, span length of the blade is only 10% of the chord length. In the LES simulation, shortage of the span length may not allow capturing the 3D flow structures well. This effect is minimized by making the lateral surfaces periodic but it can still be responsible for the large deviation of the numerical results.

At the design condition, boundary layer separates in a very small region around the trailing edge. Hence the spanwise length limitation has its lowest effect on the simulation on the account that three-dimensional motions that can be affected from the lateral dimension do not prevail in the flow and in the absence of a large boundary layer separation zone or shocks, pressure distribution becomes an inviscid phenomenon which is not very sensitive to the turbulence model. At off-design conditions, however, the spanwise limitation becomes a very important issue which can make the large eddies two-dimensional and have a huge impact on the solution.

Extension of the previously used meshes from 10% spanwise length to 100% spanwise length makes the mesh size 10 times bigger, i.e. 4.5 million nodes for stretched coarse mesh and 25 million nodes for stretched fine mesh. Due to the resource limitations, only stretched coarse mesh is feasible. Figures 6.29 and 6.30 show the isentropic Mach number distribution versus non-dimensional axial chord for design and off-design conditions respectively in case of stretched coarse mesh and iso-thermal wall conditioning. It is clearly shown in the following figures that spanwise length has no importance in design condition and it is important at the separation zone of at the off-design conditions.

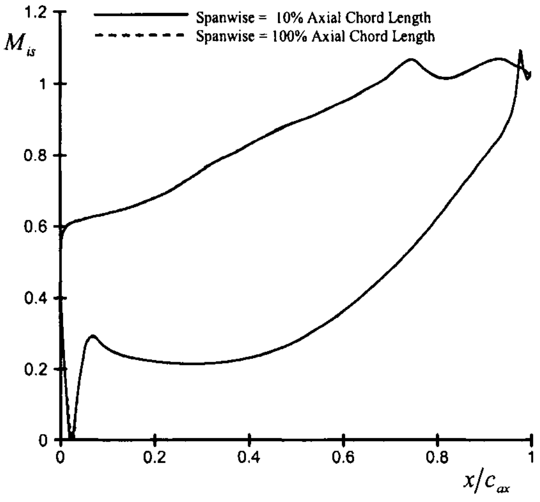

***Fig. 6.29:** Different Spanwise Lengths Design Condition*

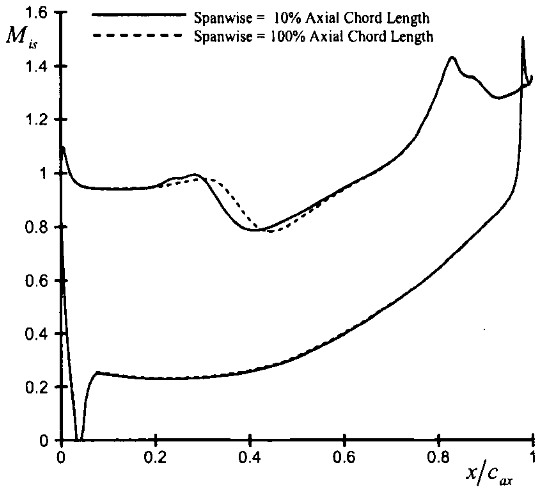

***Fig. 6.30:** Different Spanwise Lengths Off-Design Condition*

6.7 Conclusions and Future Works

Compressible turbulent flow over a gas turbine blade at high Reynolds and Mach number is investigated using the present state of the art physical models and the mathematical solution methods. Different LES methodologies are explored using a 3D unstructured tetrahedral Navier-Stokes parallel solver which is based on mixed finite-volume-finite-element method. Two different mesh levels are investigated which are one of the largest meshes that have been generated for such a CFD simulation. This work constitutes a first attempt at large eddy simulation of a compressible industrial turbulent flow over a complex geometry at high Reynolds and Mach numbers.

The results have been compared with experimental data on isentropic Mach number distribution. The results have a fairly good agreement with experimental data; however, there are still some challenges for industrial LES applications which have to be addressed to lead to a better agreement with experimental data. These challenges are mainly the shock/boundary layer interaction on the suction side near the trailing edge and separation bubble on the pressure side near the leading edge.

LES pressure distribution results have significant differences with the 3D RANS results. Much more discrepancy is expected in velocity profiles, shear stresses, and heat transfer characteristics. Considering pressure distribution results and compared to the currently used RANS models, LES results are fairly superior especially in the off-design conditions. LES results of this work are more superior to RANS results in the regions close to leading edge which contains very high strain in fluid elements and it is not satisfactorily resolvable using RANS. RANS results of [66] are superior to LES results of this work for the mid suction side at which the turbulence structures are not resolved well in LES where a separation leads to constant pressure distribution which is captured as an attached flow in LES. This might be due to not introducing fluctuations at LES inlet and also to not having enough mesh resolution. Both LES and RANS results have difficulty resolving the shock/boundary layer interaction on the rear suction side of the blade. This might also be cured in LES by improving the mesh at that region or using adaptation methods or enhancing the mesh capturing characteristics of the flux calculation method.

Different SGS methods used here do not significantly change the results in the present flow conditions. This can be a justification for using ILES method in the context of Roe method flux calculation for complex geometries. Up to now, ILES is theoretically proved to be meaningful just for very simple flows [57].

Different flux calculation methods are explored and the artificial viscosity is reduced up to the level of flow instability without a substantial difference in the results. This proves that SGS viscosity or its interaction with the numerical diffusion is not the cause of the difference between numerical and experimental results. Better resolution of the turbulent flow structures may lead to improved results compared to the time-averaging turbulence models. As far as the LES methods are concerned, for the current flow conditions, pressure does not appear to be a very sensitive quantity to the SGS viscosities.

One important assumption that is made here, is neglecting the term D_2. It is a customary practice in LES of compressible flow to offset this modeling lack by further increasing the SGS viscosity.

One important issue in this work is the limitation on spanwise length. It is already been shown that in separation zones and at off-design conditions, in which flow is highly 3D, the spanwise length limitation plays an important role. 2D RANS results of this flow [66] show that there is not a significant difference in the time-averaged pressure distribution results due to the three-dimensionality. But it completely affects the other quantities such as heat transfer characteristics. The LES results shows that at off-design condition the effect of spanwise limitation can be clearly seen in pressure distribution results. A more pronounced difference is also expected in heat transfer coefficient.

Another important issue in this simulation is the lack of introduction of fluctuations into the flow and the turbulence in the flow mainly depends on the transition occurring on the blade. Introducing these fluctuations accurately can be an expensive process. The choice of neglecting them for the time being is made solely for the sake of simplicity and as this work is a first step in LES application at Concordia University CFD Lab. Also, RANS pressure distribution results are not very sensitive to this parameter. However, this might not be true in a LES calculation as it is shown very recently [25]. Obviously there is a need for accurate and inexpensive LES inlet conditioning. Simply adding random fluctuations to the flow, which lack temporal and spatial correlations of a real turbulent flow, will dissipate shortly after the inlet [7].

A major dilemma in LES of industrial flows is that the available experimental data of engineering value are mostly tailored for RANS validations. For a better LES of engineering flows appropriate experimental data are required. The next step of this study is to improve the current LES solver by introducing a more accurate inlet condition. Also, the flux calculation method has to be improved to reduce the artificial diffusion involved. Self adaptive methods which can reduce the explicit artificial diffusion or higher order MUSCL schemes, 4th and 6th order, which can reduce the implicit artificial diffusion, have to be explored. For better capturing the shock/boundary layer structure, shock capturing characteristics of the flux calculation method has to be improved. Also, better mesh resolution in the rear suction side or using an adaptation method for improving the mesh at that region is required. The fluctuation intensities of other flow quantities will also be investigated which needs a more complete experimental data. Heat transfer characteristics and friction coefficient are of high important value and are great identifiers whether the boundary layer regime and transition to turbulence are captured well. Energy spectrum is also a very informative parameter on how well the flow structures are resolved. This work aims at accomplishing the first step and providing a solid basis for future works on an intellectually challenging topic which is of high importance in academia and industry: *Turbulence Modeling.*

BIBLIOGRAPHY

1. Ucer, A. S., AGARD lecture series 195, *Turbo-machinery design using CFD*, Chapter 2: Computational Methods for Preliminary Design and Geometry Definition and Geometry Definition in Turbo-Machinery, 1994.
2. Ucer, A. S., AGARD lecture series 195, *Turbo-machinery design using CFD*, Chapter 1: Introduction and Overview, 1994.
3. Hirsch, C., AGARD lecture series 195, *Turbo-machinery design using CFD*, Chapter 4: CFD Methodology and Validation for Turbo-Machinery Flows, 1994.
4. Schluter, J., Wu, X., Kim, S., Weide, E., Alonso, J. J., Pitsch, H., *Integrated RANS-LES of a Realistic Gas Turbine Compressor / Combustor Assembly*, Stanford University Center for Turbulence Research, Annual Research Briefs, **10**: 117-129, 2004.
5. Schluter, J., Apte, S., Kalitzin, G., Weide, E., Alonso, J. J., Pitsch, H., *Large-scale Integrated LES-RANS Simulations of a Gas Turbine Engine*, Stanford University Center for Turbulence Research, Annual Research Briefs, **11**: 111-120, 2005.
6. Schluter, J., Pitsch, H., Consistent Boundary Conditions for Integrated LES-RANS Simulations: LES Outflow Conditions, Stanford University Center for Turbulence Research, Annual Research Briefs, **7**: 19-30, 2001.
7. Schluter, J., Consistent Boundary Conditions for Integrated LES-RANS Simulations: LES Inflow Conditions, Stanford University Center for Turbulence Research, Annual Research Briefs, **8**: 143-154, 2002.

8. Schluter, J., Wu, X., On LES Outflow Conditions for Integrated LES-RANS Computations, Stanford University Center for Turbulence Research, Annual Research Briefs, **10**: 107-116, 2004.
9. Weide, E., Kalitzin, G., Schluter, J., Medic, G., Alonso, J. J., On Large Scale Turbo-Machinery Computations, Stanford University Center for Turbulence Research, Annual Research Briefs, **11**: 139-150, 2005.
10. Hahn, S., Alonso, J. J., Baeder, J., Duraisamy, K., Iaccarino, G., Lele, S., Moin, P., Schmitz, F., Shoeybi, M., Wu, X., Progress on Hybrid Unsteady Simulation of Helicopter Rotor Flow, Stanford University Center for Turbulence Research, Annual Research Briefs, **11**: 121-138, 2005.
11. Wang, M., Moreau, S., Iaccarino, G., Roger, M., LES Prediction of Pressure Fluctuation on a Low Speed Airfoil, Stanford University Center for Turbulence Research, Annual Research Briefs, **10**: 183-193, 2004.
12. Piomelli, U., *Large Eddy Simulation of Turbulent Flows*, In *Advances in Turbulence Modeling*, Lecture Series 1998-05, Olivari, D., (Lecture Series Director), von Karman Institute, Belgium, 1998.
13. Compte, P., Lesieur, M. *Large Eddy Simulation of Compressible Turbulent Flows*, In *Advances in Turbulence Modeling*, Lecture Series 1998-05, Olivari, D., (Lecture Series Director), von Karman Institute, Belgium, 1998.
14. Mary, I., *Large Eddy Simulation of Vortex Breakdown Behind a Delta Wing*, International Journal of Heat and Fluid Flow, **24**: 596–605, 2003.
15. Fujii, K., *Progress and Future Prospects of CFD in Aerospace: Wind Tunnel and Beyond*, Progress in Aerospace Sciences, **41**: 455–470, 2005.

16. Liu, C., *High Performance Computation for DNS/LES*, Applied Mathematical Modeling, **30**: 1143–1165, 2006.
17. Kim, H. J., Lee, S., Fujisawa, N., *Computation of Unsteady Flow and Aerodynamic Noise of NACA0018 Airfoil using Large-Eddy Simulation*, International Journal of Heat and Fluid Flow, **27**: 229–242, 2006.
18. Carolus, T., Schneider, M., Reese, H., *Axial Flow Fan Broad-Band Noise and Prediction*, Journal of Sound and Vibration, to be published.
19. Conway, S., Caraeni, D., Fuchs, L., *Large Eddy Simulation of the Flow through the Blades of a Swirl Generator*, International Journal of Heat and Fluid Flow, **21**: 664-673, 2000.
20. Rodi, W., *DNS and LES of Some Engineering Flows*, Fluid Dynamics Research, **38**: 145–173, 2006.
21. Schobeiri, M. T., Öztürk, B., *Experimental Study of the Effect of Periodic Unsteady Wake Flow on Boundary Layer Development, Separation, and Reattachment Along the Surface of a Low Pressure Turbine Blade*, Journal of Turbomachinery, **126**: 663–676, 2004.
22. Schobeiri, M. T., Öztürk, B., Ashpis, D. E., *Effect of Reynolds Number and Periodic Unsteady Wake Flow Condition on Boundary Layer Development, Separation, and Intermittency Behavior Along the Suction Surface of a Low Pressure Turbine Blade*, Journal of Turbomachinery, **129**: 92–107, 2007.
23. Wissink, J. G., Rodi, W., *Direct Numerical Simulations of Transitional Flow in Turbomachinery*, Journal of Turbomachinery, **128**: 668–678, 2006.

24. Mary, I., Sagaut, P., *Large Eddy Simulation of Flow around an Airfoil near Stall*, AIAA Journal, **40**(6): 1139–1145, 2002.

25. Matsuura, K., Kato, C., *Large Eddy Simulation of Compressible Transitional Flows in a Low-Pressure Turbine Cascade*, AIAA Journal, **45**(2): 442–457, 2007.

26. Cadiou, A., *NadiaLES : Manuel Theorique*, Note Technique CODICIEL-LMFA N : 2003-01.

27. Hirsch, C., *Numerical Computation of Internal and External Flows*, Vol. 2, New York: John Wiley & Sons, 1998.

28. Laney, C. B., *Computational Gas Dynamics*, Cambridge University Press, 1998.

29. Hallo, L., Le Ribault, C., Buffat, M., *An Implicit Mixed Finite-Volume-Finite-Element Method for Solving 3D Turbulent Compressible Flows*, International Journal for Numerical Methods in Fluids, **25**: 1241-1261, 1997.

30. Fezoui, L., Lanteri, S., Loriot, M., *Compressible Navier-Stokes Solver on MPPs*, In Habashi, W. G., editor, *Solution Techniques for Large-Scale CFD Problems*, New York: John Wiley & Sons, 1995.

31. Roe, P.L., *Approximate Riemann Solvers, Parameter Vectors, and Difference Schemes*, Journal of Computational Physics, **43**: 357-372, 1981.

32. Toro, E. F., *Reimann Solvers and Numerical Methods for Fluid Dynamics*, 2nd Edition, Springer-Verlag, 1999.

33. Kermani, M. J., Plett, E. G., *Modified Entropy Correction Formula for the Roe Scheme*, AIAA Paper # 2001-0083, 2001.

34. Roe, P.L., Pike, J., *Effective Construction Utilization of Approximate Riemann Solution*, In Glowinski, R. and Lions, J. L., editors, *Computing Methods in Applied Science and Engineering*, Amsterdam: North Holland, 1984
35. Harten, A., Hyman, J. M., *Self adjusting grid methods for one-dimensional hyperbolic conservation laws*, Journal of Computational Physics, **50**: 235-269, 1983.
36. Van Leer, B., *Towards the Ultimate Conservative Difference Scheme*, Lecture Notes in Physics, **18**: 163-275, 1972.
37. Harten, A., Lax, P. D., Van Leer, B., *On Upstream Differencing and Godunov Type Schemes for Hyperbolic Conservation Laws*, SIAM Reviews, **25**: 35-67, 1983.
38. Saad, Y., Schultz, M.H., *A Generalized Minimal Residual Algorithm for Solving Non-Symmetric Linear Systems*, SIAM Journal of Scientific Computation, **7**: 856-869, 1986.
39. Karypis Laboratory, http://glaros.dtc.umn.edu/gkhome/views/metis/index.html, 2006.
40. Snir, M., Otto, S., Huss-Lederman, S., Walker, D., Dongarra, J., *MPI: The Complete Reference*, 2nd Edition, Massachusetts: The MIT Press, 1996.
41. Steger, J., Warming, R. F., *Flux Vector Splitting for the Inviscid Dynamics with Application to Finite Difference Method*, Journal of Computational Physics, **40:** 265-293, 1981.
42. Pope, S. B., *Turbulent Flows*, Cambridge University Press, 2001.
43. Chung, T. J., *Computational Fluid Dynamics*, Cambridge University Press, 2002.
44. Favre, A., *Turbulence: Space-Time Statistical Properties and Behavior in Supersonic Flows*, Physics of Fluids, **26**: 2851-2863, 1983.

45. Vreman, B., Geurts, B., and Kuerten, H., *A Priori Test of Large Eddy Simulation of the Compressible Plane Mixing Layer*, Journal of Engineering Mathematics, **29**: 299-327, 1995.

46. Boersma, B. J., Lele, S.K., *Large Eddy Simulation of Compressible Turbulent Jets*, Stanford University Center for Turbulence Research, Annual Research Briefs, 1999.

47. Vreman, B., Geurts, B., and Kuerten, H., *Comparison of Numerical Schemes in Large Eddy Simulation of the Temporal Mixing Layer*, International Journal for Numerical Methods in Fluids, **22**: 297-311, 1997.

48. Bardina, J., Ferziger, J. H., Reynolds, W. C., *Improved Sub-Grid Scale Model for Large Eddy Simulation*, AIAA paper, 1357-1380, 1980.

49. Smagorinsky, J., *General Circulation Experiments with the Primitive Equations*, Monthly Weather Review, **91**: 99-164, 1963.

50. Yoshizawa, A., *Statistical Theory for Compressible Turbulent Shear Flows, with the Application to Sub-Grid Modeling*, Physics of Fluids, **29**: 2152-2164, 1986.

51. Deardoff, W. J., A numerical study of three-dimensional turbulent channel flow at large Reynolds numbers, Journal of Fluid Mechanics, **41**: 453-480, 1970.

52. McMillan, O. J., Ferziger, J. H., *Direct Testing of Sub-Grid Scale Models*, AIAA Journal, **17**: 1340-1346, 1979.

53. Schumann, U., *Direct and Large Eddy Simulation of the Turbulence – Summary of the State-of-the-Art*, In Lecture Series 1991-02: *Introduction to the Modeling of Turbulence*, VKI, Brussels, 1991.

54. Moin, P., Kim, P., *Numerical Investigation of Turbulent Channel Flow*, Journal of Fluid Mechanics, **118**: 341-377, 1982.

55. Erlebacher, G., Hussaini, M. Y., Speziale, C. G., Zang, T. A., *Toward the Large-Eddy Simulation of the Compressible Turbulent Flows*, Journal of Fluid Mechanics, **238**: 155-185, 1992.
56. Van Driest, E. R., *Turbulent Boundary Layer in Compressible Fluids*, Journal of Aeronautical Science, **18**: 145-160, 1951.
57. Piomelli, U., Moin, P., Ferziger, J. H., *Model Consistency in Large Eddy Simulation of Turbulent Channel Flow*, Physics of Fluids, **31**: 1884-1891, 1988.
58. Germano, M., Piomelli, U., Moin, P., Cabot, W. H., *A dynamic Sub-Grid Scale Eddy Viscosity Model*, Physics of Fluids, **3**(7): 1760-1765, 1991.
59. Moin, P., Squires, K., Cabot, W., Lee, S., *A Dynamic Sub-Grid Scale Model for Compressible Turbulence and Scalar Transport*, Physics of Fluids A 3, **11**: 2746-2757, 1991.
60. Lilly, D. K., *A Proposed Modification of the Germano Sub-Grid Scale Closure Method*, Physics of Fluids, **4**(3): 633-635, 1992.
61. Boris, J. P., Grinstein, F. F., Oran, E. S., Kolbe, R. L., *New Insights into Large Eddy Simulation*, Fluid Dynamic Research, **10**: 199–228, 1992.
62. Margolin, L. G., Rider, W. J., *A Rationale for Implicit Turbulence Modeling*, International Journal for Numerical Methods in Fluids, **39**: 821-841, 2002.
63. Marsden, A. L., Vasilyev, O. V., Moin, P., *Construction of Commutative Filters for LES on Unstructured Meshes*, Journal of Computational Physics, **175**: 584-603, 2002.
64. Vasilyev, O. V., Lund, T. S., Moin, P., *A General Class of Commutative Filters for LES in Complex Geometry*, Journal of Computational Physics, **146**: 82-104, 1998.

65. Ciardi, M., Sagaut, P., Klein, M., Dawes, W. N., *A Dynamic Finite Volume Scheme for Large Eddy Simulation on Unstructured Grids*, Journal of Computational Physics, **210**: 632-655, 2005.

66. Arts, T., Duboule, J. M., Rollin, G., *Aero-Thermal Performance Measurements and Analysis of a Two-Dimensional High Turning Rotor Blade*, Journal of Turbomachinery, **120**(3): 494-499, 1998.

Appendix A

y^+ CALCULATION

The non-dimensional normal distance from the wall is defined as follows,

$$y^+ = \frac{y u_\tau}{\nu} \tag{A.1}$$

y is the normal distance to the wall, ν is the kinematic viscosity. u_τ is the wall-friction velocity and is defined as,

$$u_\tau = \sqrt{\frac{\tau_w}{\rho_w}} \tag{A.2}$$

ρ_w designates the value of the density at the wall. τ_w is the wall shear stress and in boundary layer approximation is defined as,

$$\tau_w = \mu_w \left(\frac{\partial U}{\partial y} \right)_{y=0} \tag{A.3}$$

μ_w is the dynamic viscosity at the wall which is calculated using the Sutherland law. In practice and in case of complex geometries, it is simpler to determine the wall shear stress as the norm of the wall stress tensor projected on a plane tangent to the wall. The stress vector acting at the wall is defined as,

$$\vec{\tau} = \overline{\overline{\sigma}} \cdot \vec{n}_w \tag{A.4}$$

where $\overline{\overline{\sigma}}$ is the tensor of viscous stresses at the wall, and $\vec{n}_w = (\vec{t}, \vec{n}, \vec{s})$ is the local normal vector of the wall. The stress vector can be decomposed into its components as follows,

$$\vec{\tau} = \tau_{wt}\vec{t} + \tau_{n}\vec{n} + \tau_{ws}\vec{s} \tag{A.5}$$

Wall shear stress magnitude is then defined as the normal to the tangent vector as given by,

$$\tau_w = \sqrt{{\tau_{wt}}^2 + {\tau_{ws}}^2} \tag{A.6}$$

To determine these components, it suffices to remove the normal components of the wall shear stress.

$$\vec{\tau} - \left(\vec{\tau} \cdot \vec{n}\right)\vec{n} = \tau_{wt}\vec{t} + \tau_{ws}\vec{s} \tag{A.7}$$

Then, in Cartesian coordinates $\left(\bar{e}_x, \bar{e}_y, \bar{e}_z\right)$ this can be written as,

$$\vec{\tau} - \left(\vec{\tau} \cdot \vec{n}\right)\vec{n} = \tau_{wx}\vec{e}_x + \tau_{wy}\vec{e}_y + \tau_{wz}\vec{e}_z \tag{A.8}$$

and therefore,

$$\tau_w = \sqrt{{\tau_{wx}}^2 + {\tau_{wy}}^2 + {\tau_{wz}}^2} \equiv \sqrt{\left|\vec{\tau} - \left(\vec{\tau} \cdot \vec{n}\right)\vec{n}\right|} \tag{A.9}$$

Appendix B

ISENTROPIC RELATIONS

For an isentropic flow, the ratio of all the static properties, e.g. p, ρ, T, to their stagnation values can be expressed as a function of Mach number M and γ. In this case, the Mach number is called isentropic Mach number M_{is}. Starting from the energy equation,

$$c_p T_0 = c_p T + \frac{1}{2} u_i^2 \tag{B.1}$$

and plugging the speed of sound, $c^2 = \gamma R_g T$, gives,

$$\frac{c_0^2}{\gamma - 1} = \frac{c^2}{\gamma - 1} + \frac{1}{2} u_i^2 \tag{B.2}$$

where c_0 is the stagnation speed of sound. This above relation can be used to obtain the ratio of static temperature to its stagnation value, using the Mach number definition $M = u/c$ which is now isentropic Mach number in this flow.

$$\frac{c^2}{c_0^2} = \frac{T}{T_0} = \left(1 + \frac{\gamma - 1}{2} M_{is}^2\right)^{-1} \tag{B.3}$$

First law of thermodynamics states that the energy of a system and surroundings is conserved. Hence, for a system, the change in the internal energy de_I is equal to the amount of specific heat into the system dq minus the amount of work done by the system dw, i.e. $de_I = dq - dw$. Using the definition of enthalpy $h = e_I + p/\rho$, the first law of thermodynamics can be written as $dh = dq + udp$. For a perfect gas and a reversible process, $dq = c_p dT - RT\,dp/p$ and $dq = Tds$. Integration between two points 1 and 2 can be integrated as $s_2 - s_1 = c_p \ln(T_2/T_1) - R\ln(p_2/p_1)$.

In an isentropic flow (adiabatic, irreversible) of an ideal gas, one can write,

$$\frac{T_2}{T_1} = \left(\frac{p_2}{p_1}\right)^{\frac{\gamma-1}{\gamma}} = \left(\frac{\rho_2}{\rho_1}\right)^{\gamma-1} \tag{B.4}$$

Hence, using the relation B.3, the static to stagnation ratio of pressure and density can be written as,

$$\frac{p}{p_0} = \left(1 + \frac{\gamma-1}{2} M_{is}^2\right)^{-\frac{\gamma}{\gamma-1}} \tag{B.5}$$

$$\frac{\rho}{\rho_0} = \left(1 + \frac{\gamma-1}{2} M_{is}^2\right)^{\frac{-1}{\gamma-1}} \tag{B.6}$$